Search for the double beta decay of Zr-96 with NEMO-3 and calorimeter development for the SuperNEMO experiment

Matthew B. Kauer

Thesis submitted for the degree of

Doctor of Philosophy

of

UCL

Department of Physics and Astronomy

University College London

January 2010

I, Matthew B. Kauer, confirm that the work presented in this thesis is my own. Where information has been derived from other sources, I confirm that this has been indicated in the thesis.

Acknowledgements

First and foremost I would like to thank my supervisor, Ruben Saakyan, who originally took me under his wing as a temporary intern and later encouraged me towards graduate school. I would like to thank Vladimir Vasiliev for his help with software, Derek Atree and Brian Anderson for their engineering and optical expertise, and Jon Butterworth and Mark Lancaster for being fantastic HEP group leaders.

Thanks to all my UCL HEP friends who made my London experience more enjoyable through rock-n-roll, football, and climbing. Thanks to the NEMO-3 and SuperNEMO collaborators for your advice and guidance and specifically 'Team Barbotage' for our good times.

Thanks to Chris and Nikki Williams and all of LCC for your love, support, and community. Thanks to Ma, Pa, Dan, and Gar for endless hours of Sheepshead. Special thanks to my wife, Brianna, for putting up with my shenanigans these past years.

for Juniper

Abstract

Using 9.4 g of ^{96}Zr and 1221 days of data from the NEMO-3 detector corresponding to 0.031 kg·y, the obtained $2\nu\beta\beta$ decay half-life measurement is $T^{2\nu}_{1/2}$ = $[2.35 \pm 0.14(stat) \pm 0.16(syst)] \times 10^{19}$ yr. Different characteristics of the final state electrons have been studied, such as the energy sum, individual electron energy, and angular distribution. The 2ν nuclear matrix element is extracted using the measured $2\nu\beta\beta$ half-life and is $M^{2\nu}$ = 0.049 ± 0.002. The $0\nu\beta\beta$ decay half-life is excluded at the 90% CL $T^{0\nu}_{1/2} > 9.2 \times 10^{21}$ yr corresponding to a limit on the effective Majorana neutrino mass of $\langle m_{\beta\beta}\rangle < 7.2 - 19.4$ eV. Limits on other mechanisms of $0\nu\beta\beta$ have also been set.

Due for commissioning in 2012, SuperNEMO is the next generation detector which improves upon the proven technology and success of NEMO-3 to achieve a half-life sensitivity of $\sim 10^{26}$ yr (90% CL) for ^{82}Se which corresponds to a neutrino mass of 50-100 meV. An energy resolution of 7% FWHM at 1 MeV has been obtained for the calorimeter baseline design of SuperNEMO which is currently in the R&D phase. This result not only meets the requirement stipulated by the R&D proposal, but is unprecedented for this type of calorimeter design.

Contents

List of Figures

List of Tables

Chapter 1

Introduction

The recent years of experimental physics have been largely successful in validating many predictions from the standard model of particle physics. An increasing interest in the neutrino sector is due to yet unanswered fundamental questions about neutrinos. Only recently has strong evidence been found to support neutrino oscillations and mixing among flavors. By definition, neutrino oscillations are only possible if neutrinos have a non-zero mass and this leads to the questions of neutrino absolute mass and mass hierarchy. More fundamental is the question of Dirac or Majorana nature of the neutrino. A Dirac neutrino has a distinct anti-neutrino partner, but a Majorana neutrino is its own antiparticle and implies lepton number violation. An axiom of the standard model is that all fundamental particles are Dirac, therefore an observation of Majorana nature is direct evidence of physics beyond the standard model (SM) and has far-reaching implications.

Neutrinoless double-beta decay ($0\nu\beta\beta$) is one of the most sensitive processes to determine the nature, absolute mass scale, and mass hierarchy of the neutrino and will therefore have huge implications for particle physics, nuclear physics, astrophysics, and cosmology. The study of two neutrino double-beta decay ($2\nu\beta\beta$) gives us a better understanding of the nuclear models used to calculate the nuclear matrix elements, which are important to extract the new physics parameters from the $0\nu\beta\beta$ decay search. NEMO-3 is one such $0\nu\beta\beta$ experiment which is currently running and whose main aim is the search for $0\nu\beta\beta$ decay. SuperNEMO (currently in the research and design phase) is the next generation detector which improves upon the knowledge and proof of design of NEMO-3.

1.1 NEMO-3

The NEMO-3 detector is observing seven candidate $0\nu\beta\beta$ isotopes ($^{100}\mathrm{Mo}$, $^{82}\mathrm{Se}$, $^{150}\mathrm{Nd}$, $^{116}\mathrm{Cd}$, $^{130}\mathrm{Te}$, $^{48}\mathrm{Ca}$, and $^{96}\mathrm{Zr}$) for a total of 10 kg of source. These isotopes were chosen because of their large $Q_{\beta\beta}$, natural abundance and available technology for enrichment and purification. The projected half-life sensitivity is $\sim 2 \times 10^{24}$ yr (90% CL) for $^{100}\mathrm{Mo}$, corresponding to a neutrino mass of 0.3-0.6 eV. A summary of the current limits obtained for other isotopes is shown in Tab. 4.1.

Observation of $2\nu\beta\beta$ decay is an important physics interest because $2\nu\beta\beta$ and $0\nu\beta\beta$ nuclear models are guided and validated by precision experimental input from $2\nu\beta\beta$ decay. $2\nu\beta\beta$ decay is an irreducible background to $0\nu\beta\beta$ decay due to their identical event topologies, therefore precise measurement of the $2\nu\beta\beta$ decay half-life must precede $0\nu\beta\beta$ searches.

This thesis presents the measurement of the $2\nu\beta\beta$ decay half-life of $^{96}\mathrm{Zr}$ and search for neutrinoless processes using the NEMO-3 detector. Using 1221 days of data, the measurement of $^{96}\mathrm{Zr}$ two neutrino double-beta decay half-life is $[2.35 \pm 0.14(stat) \pm 0.16(syst)] \times 10^{19}$ yr. A 90% CL limit is set on the neutrinoless double-beta decay half-life of $> 9.2 \times 10^{21}$ yr corresponding to a limit on the effective Majorana neutrino mass of $< 7.2 - 19.4\,\mathrm{eV}$. These are the world's best results for this isotope.

1.2 SuperNEMO

The SuperNEMO detector will be a next-generation $0\nu\beta\beta$ experiment based on the successful design approach of NEMO-3 and will house 100 kg of source. Currently in the research and design phase, SuperNEMO has a projected half-life sensitivity of $\sim 10^{26}$ yr (90% CL) for $^{82}\mathrm{Se}$ which corresponds to a neutrino mass of 50-100 meV. One of the main challenges of the SuperNEMO R&D is the development of the calorimeter with an unprecedented energy resolution of 4% full-width at half-maximum (FWHM) at 3 MeV ($Q_{\beta\beta}$ value of $^{82}\mathrm{Se}$).

This thesis presents the results of R&D for the so-called block design, including characterization of photomultipliers and scintillators and corresponding energy resolutions of various configurations of the block design. An energy resolution of 7% FWHM at 1 MeV has been obtained which corresponds to the target resolution of 4% at 3 MeV.

This is the best energy resolution obtained to date for this type of detector.

1.3 Author's Contributions

1.3.1 NEMO-3 Contributions

- reconstruction of raw data and MC samples for ^{96}Zr analysis
- core software development for the main analysis (parsing config and input files, command line options, CLs method)
- software development for graphical representation of the results
- background measurements of the ^{96}Zr source
- full analysis of ^{96}Zr including $2\nu\beta\beta$ half-life measurement, search for $0\nu\beta\beta$ processes, extraction of $2\nu\beta\beta$ nuclear matrix element, and extraction of various lepton number violating parameters
- leading author of submitted paper on ^{96}Zr results
- data acquisition and calibration shifts for NEMO-3
- reporting results at collaboration meetings and HEPP IOP '09 conference

1.3.2 SuperNEMO Contributions

- calorimeter R&D test bench and data acquisition setup
- core development of the analysis software package
- validation of the analysis package with simulations
- characterization of photomultipliers and scintillators
- precision energy resolution measurements of various configurations
- reporting results at collaboration meetings and CALOR '08 conference

Chapter 2

Overview of neutrino physics phenomenology

2.1 Neutrino mixing

A light neutral particle called the neutrino was proposed by Wolfgang Pauli in 1930 [1]. The idea of neutrino oscillations suggested by Pontecorvo in 1957 [2] and furthered by Maki, Nakagawa, and Sakata in 1962 [3] has been experimentally verified. Mixing between the three neutrino flavors is expressed as a superposition of three mass eigenstates (ν_1,ν_2,ν_3) linked by the unitary Pontecorvo-Maki-Nakagawa-Sakata (PMNS) matrix U

$$|\nu_\alpha\rangle = \sum_i U_{\alpha i}|\nu_i\rangle \,. \tag{2.1.1}$$

The PMNS matrix can be represented as

$$U = \begin{pmatrix} c_{12}c_{13} & s_{12}c_{13} & s_{13}e^{-i\delta} \\ -s_{12}c_{23} - c_{12}s_{23}s_{13}e^{i\delta} & c_{12}c_{23} - s_{12}s_{23}s_{13}e^{i\delta} & s_{23}c_{13} \\ s_{12}s_{23} - c_{12}c_{23}s_{13}e^{i\delta} & -c_{12}s_{23} - s_{12}c_{23}s_{13}e^{i\delta} & c_{23}c_{13} \end{pmatrix} \cdot D_M \,, \tag{2.1.2}$$

where s_{ij} and c_{ij} are the sine and cosine of the three mixing angles θ_{ij} and δ is the Dirac (CP violating) phase. D_M is the diagonal Majorana phase matrix

$$D_M = \begin{pmatrix} 1 & 0 & 0 \\ 0 & e^{i\phi_2} & 0 \\ 0 & 0 & e^{i\phi_3} \end{pmatrix} \,, \tag{2.1.3}$$

where ϕ_2 and ϕ_3 are the Majorana CP-violating phases and only apply to Majorana neutrinos.

The probability in vacuum for a neutrino with flavor α to change into flavor β is

$$P(\nu_\alpha \to \nu_\beta) = \left| \sum_i U^*_{\alpha\, i}\, U_{\beta\, i}\, e^{-i\frac{m_i^2 L}{2E}} \right|^2 , \tag{2.1.4}$$

where m_i is the neutrino mass, L is the propagation length, and E is the neutrino energy. In the simplified two neutrino flavor case the experimental appearance (Eq. 2.1.5) and disappearance (Eq. 2.1.6) probabilities become

$$P(\nu_\alpha \to \nu_\beta) = \sin^2 2\theta \sin^2 \left(\Delta m^2(\mathrm{eV}^2) \frac{1.27 L(\mathrm{km})}{E(\mathrm{GeV})} \right) , \tag{2.1.5}$$

$$P(\nu_\alpha \to \nu_\alpha) = 1 - \sin^2 2\theta \sin^2 \left(\Delta m^2(\mathrm{eV}^2) \frac{1.27 L(\mathrm{km})}{E(\mathrm{GeV})} \right) , \tag{2.1.6}$$

and the parameters θ and Δm^2 may be extracted from experimental data. Oscillation parameters are measured via neutrino disappearance (none from appearance yet) from solar (SNO[4, 5], Super-Kamiokande[6, 7]), atmospheric (Super-Kamiokande[6, 7]), reactor (CHOOZ[8], KamLAND[9, 10]), and accelerator (K2K[11, 12], MINOS[13]) neutrino sources. A summary of current oscillation results is shown in Tab. 2.1.

Table 2.1: Current best global fits to neutrino oscillations are found in Ref. [14]. The arXiv version has been updated to 2007 oscillation results.

Parameter	Value	Neutrino Source
θ_{12}	34.4 ± 1.3 deg	Solar + Reactor [4, 10]
θ_{23}	45 ± 7 deg	Atm. + Accel. [6, 11]
θ_{13}	< 11 deg (90% CL)	Atm. + Reactor [8]
Δm^2_{21}	$(7.59 \pm 0.21) \times 10^{-5}$ eV^2	Solar + Reactor [4, 10]
Δm^2_{32}	$(2.43 \pm 0.13) \times 10^{-3}$ eV^2	Atm. + Accel. [6, 13]

Next generation oscillation experiments will more precisely measure the oscillation parameters and begin to address the issue of CP violation and mass hierarchy. Experiments such as Daya-Bay[15], Double CHOOZ[16], T2K[17] and NOvA[18] hope to obtain precision measurements of θ_{13}. T2K and NOvA will also measure more precisely θ_{23} and Δm^2_{32}. Searches for CP violation with current accelerator experiments are limited by hadron production uncertainty, but neutrino factories, so-called because

of the neutrino flavor purity of the beam, will be sensitive to neutrino CP violation and mass hierarchy (via matter effects).

2.2 Neutrino mass

A neutrino mass can be constructed using a Dirac or Majorana description, and by combining the Dirac and Majorana Lagrangians into one, the small neutrino mass is justified by the so called see-saw mechanism (see Sec. 2.2.3). This theory predicts a heavy ($\sim 10^{15}$ GeV) right-handed neutrino which if it exists, helps explain the observed matter to anti-matter asymmetry.

2.2.1 Dirac mass term

A Dirac neutrino mass can be generated with the Standard Model (SM) Higgs-lepton Yukawa coupling and the introduction of a chirally right-handed singlet field under the SM symmetries [19]. The essential characteristic of this field is that it is a singlet, and hence "sterile". The inclusion of only one new neutrino field singlet is known as the minimally extended Standard Model, but traditionally three chirally right-handed fields are introduced to represent each lepton generation (e, μ, τ). This is represented by the Lagrangian

$$\mathcal{L}^{D}_{mass} = -\overline{\nu_R} M_D \nu_L + H.c.\,, \tag{2.2.1}$$

where M_D is the non-diagonal Dirac mass matrix, $H.c.$ is the Hermitian conjugate, and ν_R and ν_L are the chirally right-handed and left-handed neutrino flavor fields

$$\nu_R = \begin{pmatrix} \nu_{e_R} \\ \nu_{\mu_R} \\ \nu_{\tau_R} \end{pmatrix}\,,\ \nu_L = \begin{pmatrix} \nu_{e_L} \\ \nu_{\mu_L} \\ \nu_{\tau_L} \end{pmatrix}\,. \tag{2.2.2}$$

The Dirac mass construction requires four independent components $(\nu_L, \nu_R, \overline{\nu_L}, \overline{\nu_R})$. The difficulty with this theory is the axiom of a sterile neutrino which cannot be detected and the lack of explanation for the small Higgs-neutrino Yukawa coupling relative to the other leptons and quarks.

2.2.2 Majorana mass term

An alternative approach is the massive Majorana neutrino [20] whose construction requires only two independent components. The Lagrangian for a massive Majorana

neutrino can be constructed solely out of the left-handed (or right-handed) neutrino field

$$\mathcal{L}_{mass}^{M_L} = -\frac{1}{2}\overline{\nu_L^c} M_{M_L} \nu_L + H.c.\,, \tag{2.2.3}$$

where M_{M_L} is the left-handed symmetric Majorana mass matrix and the factor of $1/2$ is introduced to avoid double counting due to the fact that $\overline{\nu_L^c}$ and ν_L are not independent. $\overline{\nu_L^c}$ is the charge conjugate of $\overline{\nu_L}$ which satisfies the condition (as shown in Ref. [19])

$$\nu_L^c = C\overline{\nu_L}^{\mathrm{T}}\,, \tag{2.2.4}$$

where C is the charge conjugation matrix and T denotes transposition. This field also has the property that

$$\nu_L^c = P_R\,\nu^c\,, \tag{2.2.5}$$

where P_R is the right-handed projection operator and this means ν_L^c is right-handed.

The Majorana neutrino has theoretical simplicity since it requires only two independent components $\left(\nu_L, \overline{\nu_L^c}\right)$ opposed to the Dirac requirement of four $(\nu_L, \nu_R, \overline{\nu_L}, \overline{\nu_R})$. The charge conjugate of the field is unchanged, meaning neutrinos are their own anti-particles, but among all other elementary fermions this is only true for neutrinos since they are neutral.

2.2.3 The see-saw mechanism

The so called see-saw mechanism is constructed to justify the small neutrino mass by combining the Dirac and Majorana terms in the Lagrangian.

$$\begin{aligned}
\mathcal{L}_{see-saw} &= \mathcal{L}_D + \mathcal{L}_{M_R}\,, \\
&= -\overline{\nu_R} M_D \nu_L - \frac{1}{2}\overline{\nu_R}^c M_{M_R} \nu_R + H.c.\,, \\
&= -\frac{1}{2}\left(\overline{\nu_L^c},\ \ \overline{\nu_R}\right)\mathcal{M}_\nu \begin{pmatrix}\nu_L \\ \nu_R^c\end{pmatrix} + H.c.\,,
\end{aligned} \tag{2.2.6}$$

where

$$\mathcal{M}_\nu = \begin{pmatrix} 0 & m_D \\ m_D & m_{M_R} \end{pmatrix}\,, \tag{2.2.7}$$

is referred to as the neutrino mass matrix. $\mathcal{M}_\nu$ is diagonalized to obtain the eigenvalues

$$M_{1,2} = \frac{1}{2} m_{M_R} \pm \sqrt{m_{M_R}^2 + 4m_D^2}\,. \tag{2.2.8}$$

In the scenario where the Dirac mass m_D is on the same order of magnitude as the Dirac mass of the other fermions and the right-handed Majorana mass term m_{M_R} is much heavier than the Dirac mass term ($m_{M_R} \gg m_D$), the first approximation of these eigenvalues is

$$M_1 \approx \frac{m_D^2}{m_{M_R}}\,, \tag{2.2.9}$$

$$M_2 \approx m_{M_R}\,. \tag{2.2.10}$$

The scenario predicts a light left-handed neutrino and a heavy right-handed Majorana neutrino. If the heavy neutrino mass is assumed to be at the Grand Unified Theory (GUT) scale ($\sim 10^{15}$ GeV), then the light neutrino is on the order of meV. This model therefore explains why the neutrino mass is small compared to that of other fermions. Important features of this scenario include the prediction of neutrinos being Majorana particles (because the Majorana mass term appears in both eigenvalues) and total lepton number violation.

2.3 Constraints on neutrino mass

Limits have been placed on the absolute neutrino mass via a number of independent methods. Δm^2_{32} from oscillation experiments provides a lower bound on the heaviest mass eigenstate to be > 0.05 eV. Cosmological data is used to place a limit on the sum of the neutrino masses ($\Sigma\, m_i$). The values obtained are model dependent, so here we assume a flat, homogeneous, isotropic universe made up of ordinary matter, radiation, dark matter and dark energy. Using a combination of data sources a limit of $\Sigma\, m_i < 2$ eV (95% CL) [21, 22] is obtained. Measurement of the β decay energy spectrum endpoint of tritium (^{3}H) has provided a limit of $\langle m_\beta \rangle < 2.0$ eV (95% CL) [23, 24]. It is important to note that the limit from tritium decay is model independent. The current best limit on neutrino mass from double-beta decay experiment is $\langle m_{\beta\beta} \rangle < 0.30$ eV (90% CL) [25] obtained by combining data from Heidelberg-Moscow and IGEX experiments (Sec. 4.1.1). The controversial claim of observing $0\nu\beta\beta$ signal published by a fraction of the Heidelberg-Moscow collaboration is discussed in Sec. 4.1.1. A summary of limits on neutrino mass is shown in Tab. 2.2.

Oscillation experiment, β-decay, and $0\nu\beta\beta$ decay measurements are necessary to obtain a complete understanding of the neutrino. Mixing parameters are measured

Table 2.2: Current constraints on neutrino mass using oscillation data, cosmological data, tritium β^- decay, and $0\nu\beta\beta$ decay.

Parameter	Obtained Limit	Ref.
oscill.	$> 0.05\,\text{eV}$ (68% CL)	heaviest mass eigenstate
$\Sigma\, m_i$	$< 2\,\text{eV}$ (95% CL)	Cosmo. [21, 22]
$\langle m_\beta \rangle$	$< 2.0\,\text{eV}$ (95% CL)	Tritium decay [23, 24]
$\langle m_{\beta\beta} \rangle$	$< 0.30\,\text{eV}$ (90% CL)	$0\nu\beta\beta$ decay [25]

and eventually Dirac CP violation may be accessible through oscillation experiments. Tritium decay measurements give access to the effective electron neutrino mass without prior knowledge of the Dirac/Majorana CP violation parameters via the squared mass

$$\langle m_\beta \rangle^2 = \sum_i |U_{\alpha\, i}|^2\, m_i^2 = c_{12}^2 c_{13}^2 m_1^2 + s_{12}^2 c_{13}^2 m_2^2 + s_{13}^2 m_3^2\,, \tag{2.3.1}$$

but requires knowledge of the neutrino flavor mixing angles. The masses m_i are squared in Eq. 2.3.1 because $\langle m_\beta \rangle^2$ is the observable [24]. Neutrinoless double-beta decay is a unique process which allows access to a number of desired neutrino parameters including the mass hierarchy, CP violating phase, and the absolute neutrino mass scale because the effective mass of the electron neutrino obtained from $0\nu\beta\beta$ experiment is given by effective mass

$$\langle m_{\beta\beta} \rangle = \left| \sum_i U_{\alpha\, i}^2\, m_i \right| = \left| c_{12}^2 c_{13}^2 m_1 + s_{12}^2 c_{13}^2 m_2\, e^{2i\phi_2} + s_{13}^2 m_3\, e^{2i(\phi_3+\delta)} \right|\,. \tag{2.3.2}$$

There is a factor of $U_{\alpha\, i}$ for each $W^-\nu\, e^-$ vertex of the Feynman diagram shown in Fig. 3.5. The complimentary nature of the different experimental methods is visualized in Tab. 2.3.

Table 2.3: Neutrino characteristics accessible through the main experimental approaches.

	β-decay	$0\nu\beta\beta$	Oscill.
Neutrino nature		$\surd$	
Absolute mass	$\surd$	$\surd$	
Mass hierarchy		$\surd$	$\surd$
Mixing Param.			$\surd$
Dirac CP			$\surd$
Majorana CP		$\surd$	

Chapter 3

Double beta decay theory

3.1 Single β decay

Beta decay can occur via electron emission (β^-), positron emission (β^+), and electron capture (EC). β^- decay is a process in which a neutron decays to a proton while emitting an electron and anti-electron neutrino

$$n \rightarrow p + e^- + \overline{\nu_e}\,, \tag{3.1.1}$$

β^+ decay is a process in which a proton decays to a neutron while emitting a positron and electron neutrino

$$p \rightarrow n + e^+ + \nu_e\,, \tag{3.1.2}$$

and the process of EC occurs when the nucleus does not have enough energy to emit a positron

$$p + e^- \rightarrow n + \nu_e\,. \tag{3.1.3}$$

The captured electron (usually K-shell) leaves a hole in which electrons from higher levels cascade down. This process is therefore accompanied by X-rays and/or Auger electrons. These three processes cannot occur unless the mass of the parent atom is greater than the summed mass of the daughter atom and emitted particles

$$\begin{aligned} Z_i m_p + (A_i - Z_i) m_n + N_i m_e - E_i^B \\ > Z_f m_p + (A_f - Z_f) m_n + N_f m_e - E_f^B\,, \end{aligned} \tag{3.1.4}$$

where m_p, m_n, and m_e are the mass of the proton, neutron, and electron, respectively. E^B is the nuclear binding energy and subscripts i and f represent the initial and final states.

The Semi-Empirical Mass Formula (SEMF) [26] is used to calculate the atomic mass M as a function of its mass number A and atomic number Z and provides predictions for allowed and forbidden decay modes and transition energies. The SEMF has six terms, the first term being the summed mass of all protons and neutrons. This is just an approximation and all the proceeding terms act as corrections. They are the volume, surface, Coulomb, asymmetry, and pairing terms. The pairing term maximizes the binding energy of even-even nuclei and minimizes the binding of odd-odd nuclei. Two separate parabolas therefore describe the mass of even-even and odd-odd nuclei as a function of Z as seen in Fig. 3.1.

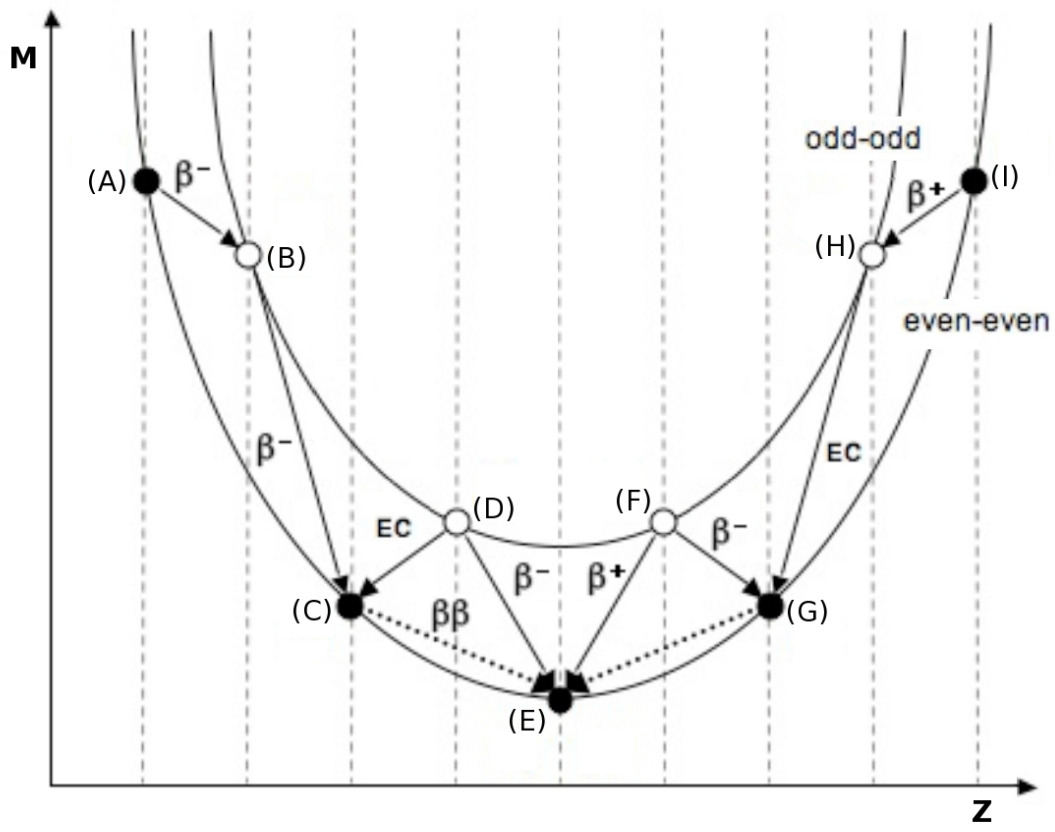

Figure 3.1: The two parabolas show energetically allowed beta and double-beta decays for an arbitrary decay chain. The transition C $\rightarrow$ D is energetically forbidden, therefore double-beta decay is the only transition that allows C $\rightarrow$ E.

3.2 Two neutrino double-beta decay

Proposed by Maria Goeppert-Mayer in 1935 [27], two neutrino double-beta decay ($2\nu\beta\beta$) is a second order process in which two neutrons spontaneously decay to two protons while emitting two electrons and two anti-electron neutrinos

$$(A, Z) \rightarrow (A, Z + 2) + 2e^- + 2\overline{\nu_e}\,, \tag{3.2.1}$$

where A is the mass number and Z is the atomic number. This process conserves electric charge, lepton number, and is allowed under the standard electroweak model as seen in Fig. 3.2. $2\nu\beta\beta$ decay can occur in even-even nuclei (even number of protons

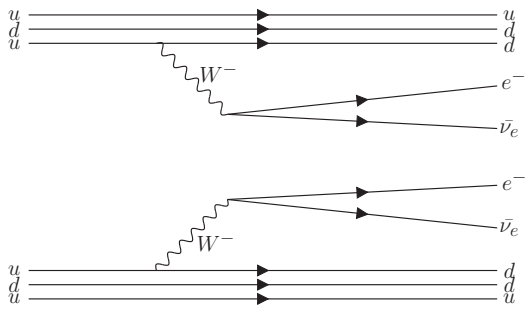

Figure 3.2: Feynman diagram for $2\nu\beta\beta$ decay allowed in the standard model which conserves electric charge and lepton number.

and neutrons) as seen in Fig. 3.1. The nuclear transition energy $Q_{\beta\beta}$ is defined

$$Q_{\beta\beta} = m(A, Z) - m(A, Z\ +\ 2) - 2m_e\,, \tag{3.2.2}$$

where $m(A, Z)$ and $m(A, Z\ +\ 2)$ are respectively the mass of the initial and final nucleus and m_e is the mass of the electron. The half-life of this process is written

$$(T^{2\nu}_{1/2})^{-1} = G^{2\nu}\,|M^{2\nu}|^{\,2}\,, \tag{3.2.3}$$

where $G^{2\nu}$ is the analytically calculable phase space. The nuclear matrix element $M^{2\nu}$ is the transition probability which is theoretically calculated but model dependent, therefore comparison to experimentally extracted values is crucial. Nuclear matrix element (NME) models will be further discussed in Sec. 3.4.

3.3 Neutrinoless double-beta decay

With present data we do not know the absolute mass eigenstate hierarchy, i.e. whether m_3 is heavier or lighter than m_1 and m_2 as seen in Fig. 3.3. $0\nu\beta\beta$ decay is a

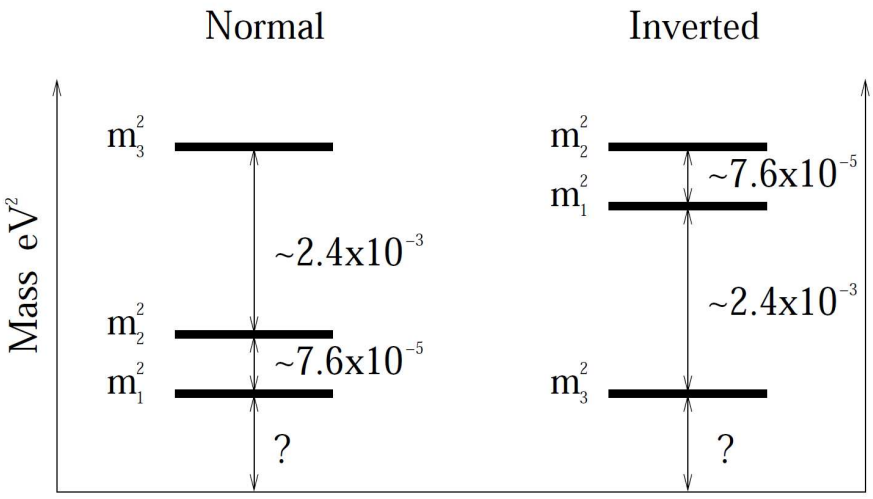

Figure 3.3: Depiction of the normal and inverted hierarchies of absolute mass eigenstates.

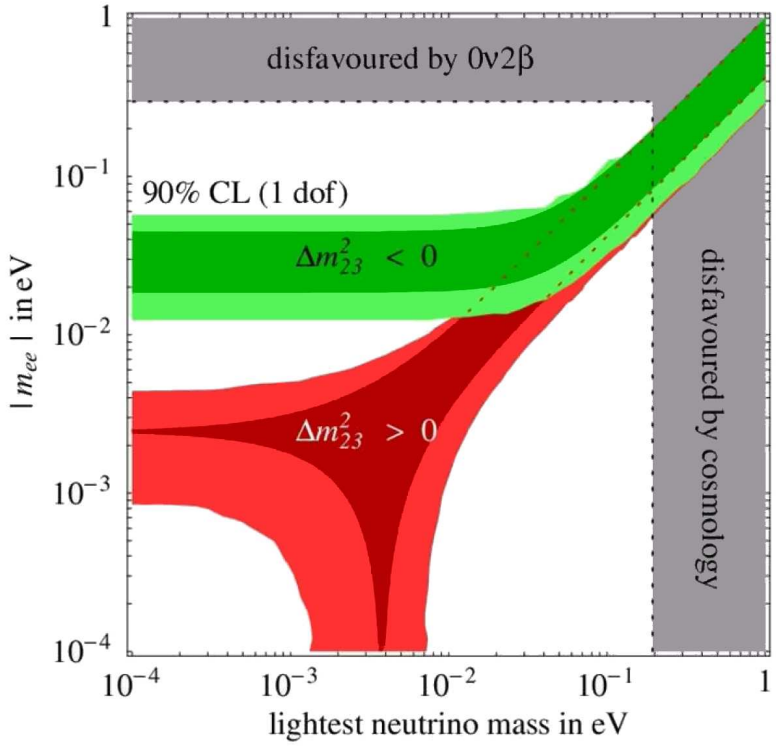

Figure 3.4: The effective electron neutrino mass as a function of the lightest mass eigenstate provides discrimination between mass eigenstate hierarchy models.

sensitive probe of the neutrino hierarchy and Fig. 3.4 shows the discrimination between hierarchies as a function of the effective neutrino mass from $0\nu\beta\beta$ experiment. It is unlikely but possible for the Majorana phases to cancel and give an effective neutrino

mass of zero resulting in no $0\nu\beta\beta$ decay signal.

Neutrinoless double-beta decay ($0\nu\beta\beta$) was suggested in 1937 by Guilio Racah [28] to test Majorana's theory and in 1939 Wendell Furry calculated the transition probabilities for the decay [29]. $0\nu\beta\beta$ violates total lepton number conservation and is forbidden under the standard electroweak model. No real neutrinos are in the final state of this process, rather a virtual right-handed Majorana neutrino (similar to a Dirac anti-neutrino) is emitted from one vertex and absorbed at the other vertex as a virtual left-handed Majorana neutrino (Fig. 3.5). The probability of the second vertex

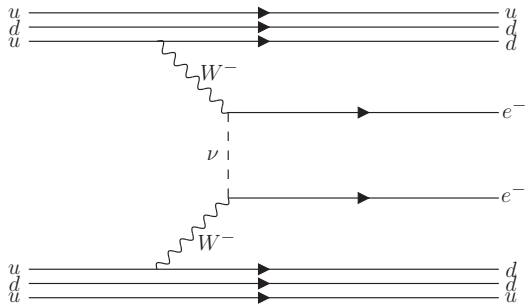

Figure 3.5: Feynman diagram of $0\nu\beta\beta$ decay which is forbidden by the standard model because it violates total lepton number conservation.

being in a frame of reference required for the helicity flip is proportional to the mass squared of the neutrino. Neutrinoless double-beta decay, therefore cannot occur unless the neutrino has mass and is Majorana by nature ($\nu_e = \overline{\nu_e}$).

The half-life of an arbitrary $0\nu\beta\beta$ mechanism is generalized as

$$(T^{0\nu}_{1/2})^{-1} = G^{0\nu} \left|M^{0\nu}\right|^2 \eta^2 \,, \tag{3.3.1}$$

where $G^{0\nu}$ is the precisely calculable phase-space, $M^{0\nu}$ is the NME of the decay, and η is the lepton number violating parameter. η takes on a different form to represent various $0\nu\beta\beta$ mechanisms, for example the mass mechanism $\langle m_{\beta\beta}\rangle$ (Sec. 3.3.1), right-handed currents $\langle\lambda\rangle$ (Sec. 3.3.2), and Majoron emission $\langle g_{\chi^0}\rangle$ (Sec. 3.3.2).

3.3.1 The mass mechanism

The mass mechanism is the most discussed scenario because it minimizes the modification of the SM. The half-life of the $0\nu\beta\beta$ mass mechanism is expressed

$$(T^{0\nu}_{1/2})^{-1} = G^{0\nu} \left|M^{0\nu}\right|^2 \langle m_{\beta\beta}\rangle^2 \,, \tag{3.3.2}$$

where $G^{0\nu}$ is the precisely calculable phase-space proportional to $Q^5_{\beta\beta}$ (the transition energy of the decay to the fifth power), $M^{0\nu}$ is the NME of the decay, and $\langle m_{\beta\beta}\rangle$ is the effective Majorana mass of the electron neutrino, as defined by Eq. 2.3.2. The phase-space value for $0\nu\beta\beta$ ($\propto Q^5_{\beta\beta}$) is limited by the kinematics of the virtual neutrino and is much less than the phase-space value for $2\nu\beta\beta$ which is proportional to $Q^{11}_{\beta\beta}$. Knowledge of the $0\nu\beta\beta$ NME is required to experimentally extract the $\langle m_{\beta\beta}\rangle$ parameter and is further discussed in Sec. 3.4.

3.3.2 Other mechanisms of $0\nu\beta\beta$ decay

The mass mechanism is so called because the neutrino must have mass to achieve the relative helicity flip. Another proposed mechanism is right-handed currents and introduces two new physics parameters $\langle\eta\rangle$ and $\langle\lambda\rangle$. The coupling between the right-handed leptonic current and left-handed quark current is defined by $\langle\eta\rangle$, while $\langle\lambda\rangle$ describes the coupling when both currents are right-handed. $\langle\lambda\rangle$ is more often discussed and the half-life is expressed

$$(T^{0\nu\lambda}_{1/2})^{-1} = G^{0\nu\lambda}\left|M^{0\nu}\right|^2\langle\lambda\rangle^2 . \tag{3.3.3}$$

Several models beyond the SM exist in which global Baryon-Lepton (B-L) symmetry is spontaneously broken due to a massless Goldstone boson. The term "Majoron" is used to refer to a predicted Goldstone boson which couples to the neutrino. Singlet, doublet, and triplet Majoron models were postulated but the doublet and triplet models were ruled out by the Z boson width measurement at LEP [30]. The singlet model remains but requires severe fine tuning. New Majoron models have been suggested and the term "Majoron" has been redefined as a light or massless boson which weakly couples to the neutrino with no constraint on being a Goldstone boson.

The various Majoron models are referred to by their spectral index n which determines the dependence of the phase-space on the energy released in the decay as $G^{0\nu} \propto (Q_{\beta\beta} - E_{sum})^n$, where E_{sum} is the sum of the kinetic energies of the electrons emitted in the decay. Spectral index $n = 1$ denotes models with one Majoron emission [31, 32], the "bulk" Majoron in the context of the "brane-bulk" scenario has $n = 2$ [33], $n = 3$ denotes the emission of one or two massless lepton number carrying Majorons [34, 35, 31], and the scenario where two light Majorons are emitted has $n = 7$ [34, 35, 31]. The expected energy spectra of these models is illustrated

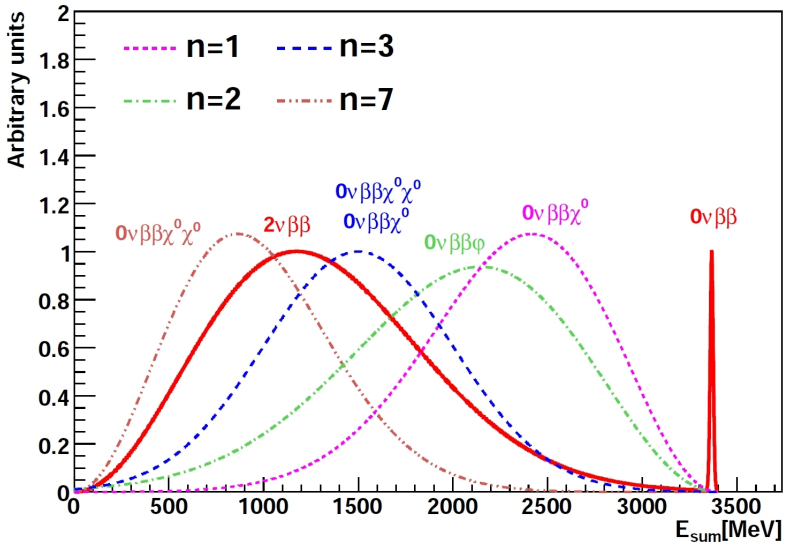

Figure 3.6: Energy spectra for $2\nu\beta\beta$ and $0\nu\beta\beta$ and Majoron emission modes where the spectral index n = 1, 2, 3, and 7. The illustration is courtesy of Dr. Fatemi-Ghomi [36].

in Fig. 3.6. The half-life for $0\nu\beta\beta$ decay accompanied by Majoron emission is expressed

$$(T^{0\nu\chi^0}_{1/2})^{-1} = G^{0\nu\chi^0} \left|M^{0\nu}\right|^2 \langle g_{\chi^0}\rangle^2 , \tag{3.3.4}$$

where $\langle g_{\chi^0}\rangle$ is the Majoron to neutrino coupling.

Other possibilities, albeit more exotic include R-parity violating SUSY [37], doubly charged Higgs [38], and leptoquarks.

3.4 Nuclear matrix elements

The accuracy at which $\langle m_{\beta\beta}\rangle$ can be extracted from Eq. 3.3.2 depends upon the measured half-life and the precision of the NME (the kinematic phase-space is precisely calculable). The successful models thus far include the nuclear shell model (NSM), the quasiparticle random phase approximation (QRPA), and the projected Hartree-Fock-Bogoliubov (PHFB) model.

3.4.1 The nuclear shell model

The NSM and QRPA (Sec. 3.4.2) methods are complementary. In simplistic terms, NSM includes few single-particle orbitals around a relatively large inert core but includes arbitrarily complicated correlations, while QRPA includes many single-particle orbitals outside a relatively small inert core but limits itself to certain types of corre-

lations, thereby reducing complexity. The NSM can handle most isotopes but still has difficulty with deformed nuclei such as ^{150}Nd. NSM calculations are very complex for heavy isotopes, therefore QRPA has been more successful for these calculations. Around 2007 the inclusion of short-range correlations [39, 40] in NSM improved the consistency between the NSM and QRPA models. The improved NSM calculations are compared with QRPA values in Fig. 3.7.

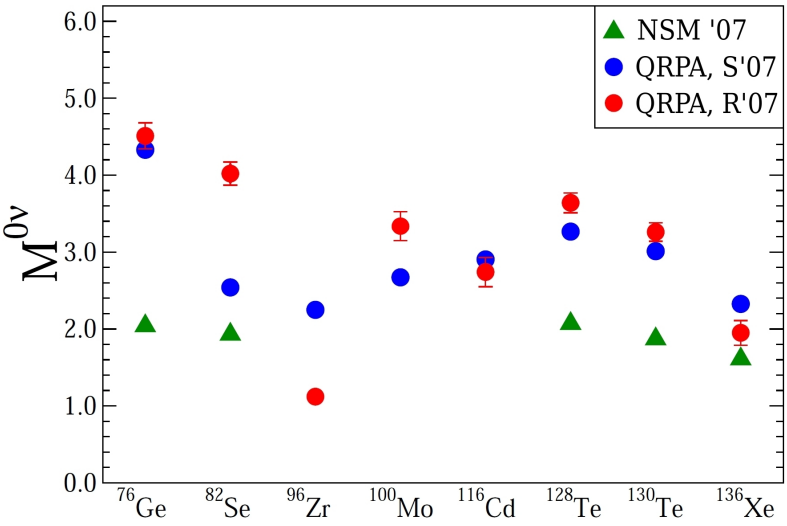

Figure 3.7: Recent NSM calculations [40] compared with QRPA calculations by Suhonen *et. al.* [41] and Rodin *et. al.* [42].

3.4.2 The quasiparticle random phase approximation

In the QRPA the NME calculation is the sum of the Gamow-Teller M_{GT}, Fermi M_F, and tensor M_T contributions

$$M^{0\nu} = M_{GT} - \frac{M_F}{g_A^2} + M_T \,, \tag{3.4.1}$$

where g_A is the effective axial coupling generally set to $g_A = 1.25$. It is necessary to introduce parameters for the particle-particle g_{pp} and particle-hole g_{ph} pairing interactions. The g_{ph} is chosen to reproduce the experimentally known excitation energy of the Gamow-Teller giant resonance and generally $g_{ph} \approx 1$. The g_{pp} has a large effect on M_{GT} and is either left as a free parameter or fixed to reproduce the correct $2\nu\beta\beta$ decay rate or the intermediate β-decay rate. The QRPA is unstable against the increase of proton-neutron correlations and several extensions of QRPA have been proposed to

stabilize solutions but introduce ambiguities of their own. The advantages and shortcomings of these models are discussed in Refs.[43, 44, 45].

3.4.3 The projected Hartree-Fock-Bogoliubov model

The PHFB model has theoretical advantages because $M^{2\nu}$ and $M^{0\nu}$ are calculated with fewer model dependent parameters. Furthermore, the inclusion of nuclear deformation degrees of freedom is observed to play an important role in the quenching of $M^{2\nu}$ [46, 47]. Recent PHFB calculations are compared with NSM and QRPA values in Fig. 3.8.

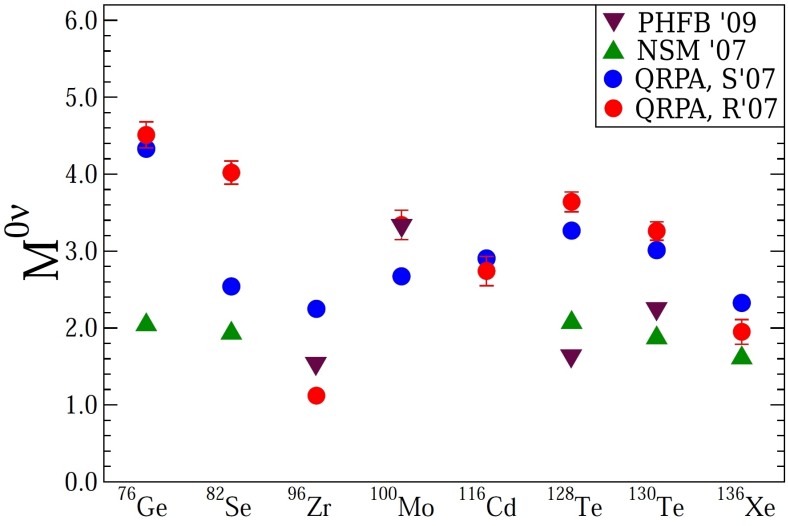

Figure 3.8: PHFB NME values [47] compared with those computed by NSM [40] and QRPA from authors Suhonen *et. al.* [41] and Rodin *et. al.* [42].

Chapter 4

Experimental techniques and status

Searching for $0\nu\beta\beta$ (and $2\nu\beta\beta$) decay is a sensitive process. Experimental techniques generally focus on background suppression as typical $0\nu\beta\beta$ half-lives are $> 10^{25}$ yr and the half-lives of natural radioactivity are $\sim 10^{10}$ yr. Background suppression and several other factors contribute to the sensitivity of the experiment and are outlined below:

- Approximately 100 kg of enriched isotope is needed to reach the 50 meV region of interest.
- Isotope and detector components must have a high radiopurity (mBq/kg).
- Cosmic ray backgrounds are suppressed by locating experiments underground (typically > 2500 MWE).
- The detector needs shielding to suppress the external background flux from the surrounding environment.
- Isotopes with large $Q_{\beta\beta}$ (> 3 MeV) are favored to increase the energy separation between the $0\nu\beta\beta$ peak and lower energy backgrounds.
- A good energy resolution provides separation between the $2\nu\beta\beta$ tail and the $0\nu\beta\beta$ peak as $2\nu\beta\beta$ events are an irreducible background to $0\nu\beta\beta$ searches.
- Event reconstruction, particle identification, and event topologies are powerful tools for background suppression.
- Reliability of NME calculations is essential for extraction of the effective Majorana neutrino mass.

Future experiments hoping to achieve a sensitivity of a few meV require >1 ton of isotope and purity at the level of μBq/kg.

Double-beta decay experiments can be divided into categories of homogeneous where the isotope is the detector and heterogeneous in which the source is separate from the detector. Homogeneous techniques generally have excellent energy resolution whereas heterogeneous experiments have tracking detectors and consequently better particle identification. The experiments mentioned in Sec. 4.1 and 4.2 are summarized in Tab. 4.1 with their past or current limits on effective neutrino mass and in Tab. 4.2 with future projected sensitivities to neutrino mass.

Table 4.1: A brief summary of current (top) and past (bottom) $0\nu\beta\beta$ experiments and their obtained limits on the neutrino mass at 90% CL.

Experiment	Isotope	Mass	kg·y	$T^{0\nu}_{1/2}$ (yr)	$\langle m_{\beta\beta}\rangle$ (eV)	Refs.
NEMO-3	^{48}Ca	7.0 g	0.018	$>1.3\times10^{22}$	<23	[48, 49]
NEMO-3	^{82}Se	932 g	1.76	$>2.1\times10^{23}$	<1.4 - 2.2	[50, 49]
NEMO-3	^{96}Zr	9.4 g	0.031	$>9.2\times10^{21}$	<7.2 - 19.5	[51, 49]
NEMO-3	^{100}Mo	6.9 kg	13.1	$>5.8\times10^{23}$	<0.61 - 1.26	[52, 49]
NEMO-3	^{150}Nd	37 g	0.094	$>1.8\times10^{22}$	<1.7 - 2.4	[53, 49]
ELEGANT VI	^{48}Ca	7.6 g	0.025	$>5.8\times10^{22}$	<3.5 - 22	[54, 55]
H-M	^{76}Ge	11 kg	71.7	1.19×10^{25}	0.44	[56, 57]
IGEX	^{76}Ge	8.4 kg	10.1	$>1.6\times10^{25}$	<0.33 - 1.35	[58, 59]
ELEGANT V	^{100}Mo	171 g	0.14	$>4.3\times10^{22}$	<2.3	[60, 61]
CUORICINO	^{130}Te	11 kg	15.53	$>3.1\times10^{24}$	<0.19 - 0.68	[62, 63]

4.1 Experiments following a homogeneous design

Homogeneous systems are preferred for their good energy resolution, radiopurity, and relatively compact design. Popular techniques include semiconductor detectors, bolometers, and scintillator detectors. The downsides to this approach is poor particle identification and event reconstruction.

Table 4.2: A brief summary of future $0\nu\beta\beta$ experiments and their projected sensitivities to the neutrino mass.

Experiment	Isotope	Mass (kg)	$\langle m_{\beta\beta}\rangle$ (meV)	Refs.
CANDLES III	^{48}Ca	0.2	500	[64]
CANDLES	^{48}Ca	3	100	[64, 65]
GERDA-I	^{76}Ge	18	600	[66, 67]
GERDA-II	^{76}Ge	40	100	[66, 67]
MAJORANA	^{76}Ge	26	150	[68, 69]
SuperNEMO	^{82}Se	100	70	[70, 71]
MOON-I	^{100}Mo	30	160	[72, 73]
MOON-II	^{100}Mo	120	100	[72, 73]
MOON-III	^{100}Mo	480	45	[72, 73]
COBRA	^{116}Cd	140	45	[74, 75]
CUORE	^{130}Te	203	60	[76, 77]
EXO-200	^{136}Xe	160	160	[78, 79]
EXO	^{136}Xe	800	30	[79]
NEXT-100	^{136}Xe	80	120	[80, 81]
XMASS	^{136}Xe	90	100	[82]
MTD-1	^{150}Nd	32	100	[83]
MTD-50	^{150}Nd	600	30	[83]
SNO+	^{150}Nd	56	100	[84, 85]

4.1.1 Semiconductor experiments

Semiconducting germanium detectors are favored for their great energy resolution and radiopurity. Previous experiments Heidelberg-Moscow (H-M) and IGEX (International Germanium EXperiment) have produced the most strict limits on $\langle m_{\beta\beta}\rangle$ thus far as summarized in Tab. 4.1.

The Heidelberg-Moscow experiment had a mass of 11 kg ^{76}Ge. Using 71.7 kg·y of data, a fraction of the collaboration reported [56] a signal (Fig. 4.1) with half-life $T^{0\nu}_{1/2} = 1.19^{+2.99}_{-0.50} \times 10^{25}$ yr (3σ) corresponding to $\langle m_{\beta\beta}\rangle = 0.44^{+0.14}_{-0.20}$ eV (3σ) using the NME

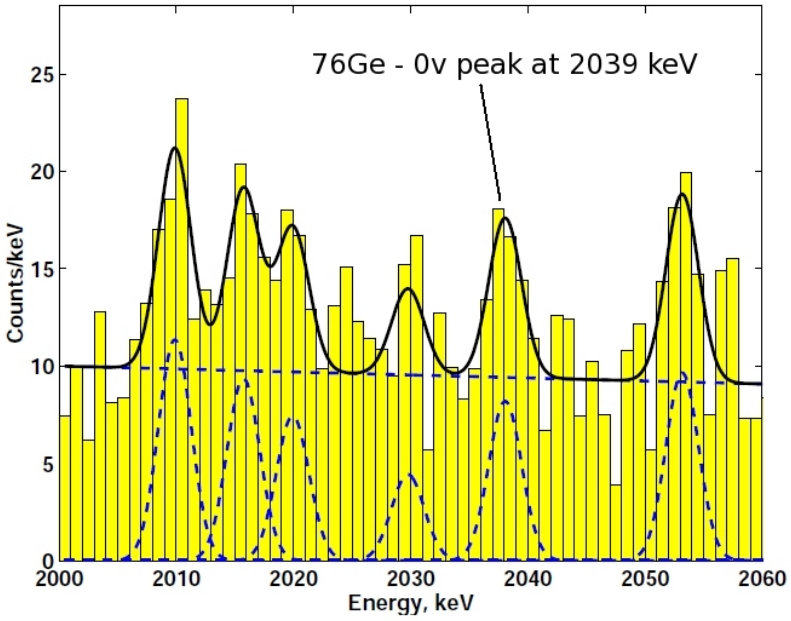

Figure 4.1: The claimed $^{76}\mathrm{Ge}$ $0\nu\beta\beta$ signal at 2039 keV from a subset of the Heidelberg-Moscow experiment.

from Ref. [86]. This claim received much criticism due to incorrect relative strengths of the presumed $^{214}\mathrm{Bi}$ peaks at 2011, 2017, 2022, and 2053 keV and an unidentified peak near 2030 keV. It is also argued that the backgrounds and systematic uncertainty are underestimated. Other experiments [58, 63] have not seen evidence of $0\nu\beta\beta$ signal but were unable to fully excluded the claim due to insufficient sensitivity. Addressing this claim is one of the main tasks of the upcoming future experiments in their first 1-2 years of running.

The proposed GERDA (GERmanium Detector Array) experiment will operate in two phases (GERDA-I and GERDA-II). The germanium from the previous Heidelberg-Moscow and IGEX experiments ($\sim$ 18 kg $^{76}\mathrm{Ge}$ total) will be used for GERDA-I. Another $\sim$ 25 kg $^{76}\mathrm{Ge}$ will be added for GERDA-II to reach a sensitivity of $\langle m_{\beta\beta}\rangle \sim$ 100 meV. The MAJORANA experiment proposes $\sim$ 30 kg germanium enriched to 86% $^{76}\mathrm{Ge}$ to achieve a sensitivity of $\langle m_{\beta\beta}\rangle \sim$ 150 meV.

The COBRA (Cadmium telluride 0-neutrino Beta decay Research Apparatus) experiment is currently in the R&D stage and will use semiconducting CdZnTe (CZT) crystals to study a range of isotopes and decay mechanisms. Decay processes $\beta^+\beta^+$, β^+ EC, and EC EC will be searched for in ^{67}Zn, ^{106}Cd, ^{108}Cd, and ^{120}Te isotopes but the

greatest sensitivity to $0\nu\beta\beta$ decay comes from the $^{116}\mathrm{Cd}$ component with a projected sensitivity of $\langle m_{\beta\beta}\rangle \sim 45$ meV.

4.1.2 Bolometer experiments

Bolometers are used to measure the temperature increase as a function of the energy deposited in the crystal. As the temperature of the crystal is decreased, the specific heat decreases according to the Debye law which is proportional to $(T/T_D)^3$, where T_D is the Debye temperature of the crystal. The temperature increase of the crystal per unit energy deposited is inversely proportional to the specific heat of the crystal, therefore very low temperatures are needed (~ 10 mK) to obtain a measurable temperature rise for the energy region of interest.

MI-BETA [87, 88] was the first bolometer type experiment and precursor of the CUORICINO (Italian for "small CUORE") experiment. CUORICINO has crystals operating at 10 mK (~ 0.2 mK/MeV) with a total mass of 41 kg TeO_2 with natural $^{130}\mathrm{Te}$ abundance (33.8%). CUORICINO has finished taking data and the current limit obtained for $0\nu\beta\beta$ decay is $T^{0\nu}_{1/2} > 3.1 \times 10^{24}$ yr corresponding to $\langle m_{\beta\beta}\rangle < 0.2$-$0.7$ eV. CUORE (Cryogenic Underground Observatory of Rare Events) is the next generation experiment currently in the R&D phase designed to hold 750 kg of TeO_2 of which 203 kg will be $^{130}\mathrm{Te}$. Their expected half-life sensitivity is $\sim 2.1 \times 10^{26}$ yr corresponding to $\langle m_{\beta\beta}\rangle \sim 40$-$90$ meV.

4.1.3 Scintillator experiments

In general, scintillator experiments are less technically complicated than semiconductor or bolometer types. Solid CaF_2 crystal scintillators are used for example in the ELEGANT VI and CANDLES (CAlcium fluoride for studies of Neutrinos and Dark matter by Low Energy Spectroscopy) experiments. ELEGANT VI obtained a limit on the $0\nu\beta\beta$ half-life of $^{48}\mathrm{Ca}$ to be $T^{0\nu}_{1/2} > 1.4 \times 10^{22}$ yr corresponding to $\langle m_{\beta\beta}\rangle < 23$ eV. CANDLES is the next generation detector being developed on the success of ELEGANT VI. CANDLES currently houses 200 kg CaF_2 corresponding to ~ 0.2 kg $^{48}\mathrm{Ca}$ (called CANDLES III) with a sensitivity $\langle m_{\beta\beta}\rangle \sim 500$ meV and plans to expand to 3 tons CaF_2 corresponding to ~ 3 kg $^{48}\mathrm{Ca}$ to achieve a sensitivity of $\langle m_{\beta\beta}\rangle \sim 100$ meV.

Liquid scintillator experiments currently being proposed are SNO+ (Sudbury Neutrino Observatory +) and XMASS (Xenon detector for weakly interaction MASSive

particles). SNO+ proposes to focus on $0\nu\beta\beta$ decay searches via $^{150}\mathrm{Nd}$ loading of its liquid scintillator but solar and geo neutrinos will remain an important part of the program. 1000 tones of liquid scintillator loaded with 1% natural neodymium corresponds to 56 kg $^{150}\mathrm{Nd}$ and a sensitivity of $\langle m_{\beta\beta}\rangle \sim 100$ meV. If $^{150}\mathrm{Nd}$ enrichment proves to be possible, SNO+ may achieve a sensitivity < 100 meV but issues of energy resolution and neodymium purification need to be addressed. XMASS is a dark matter and solar neutrino experiment using 100 kg of liquid xenon. A proposed expansion to 1-20 tons of natural xenon allows $0\nu\beta\beta$ decay searches with $^{136}\mathrm{Xe}$ but studies have shown that a re-configuration of the detector would be needed.

The EXO (Enriched Xenon Observatory) detector is a TPC using 1-10 tons of liquid xenon (similar to XMASS) enriched to 80% $^{136}\mathrm{Xe}$. A cathode wire at the center surrounded by anode wires along the circumference of the detector allows for particle trajectory reconstruction and charge collection leading to the measurement of deposited energy. As liquid xenon is also an efficient scintillator, the energy resolution of the detector is improved by the combination of light and charge collection. The first phase called EXO-200 uses 200 kg of xenon enriched to 80% $^{136}\mathrm{Xe}$ and is expected to reach a sensitivity of $\langle m_{\beta\beta}\rangle \sim$ 130-190 meV. Similar to EXO, NEXT (Neutrino Experiment with a Xenon TPC) is a proposed enriched liquid xenon TPC. The first phase of the experiment NEXT-100 holds 100 kg xenon enriched to 80% $^{136}\mathrm{Xe}$ and predicts a sensitivity of $\langle m_{\beta\beta}\rangle \sim$ 100-140 meV. There are plans for a future ton-scale design.

4.2 Experiments following a heterogeneous design

Heterogeneous detectors are advantageous because of particle identification and event topology selection which leads to background suppression. The two most common techniques are the time projection chamber (TPC) where the ionizing gas or liquid is loaded with the source isotope (or a solid source foil is housed within the TPC) and the tracking detector plus calorimeter design where a solid foil contains the source isotope and is located within the tracking detector.

4.2.1 Time projection chambers

Time projection chambers use an electric field to drift the ionization track(s) from an event to a charge collection device, typically drift-cells. A novel approach images the

electroluminescence via a multi-pixel PMT or CCD. Generally the chamber geometry and gas density are chosen so that the events of interest deposit their full energy in the ionizing medium. Because the amount of total ionization is proportional to the energy deposited in the gas, this approach allows the energy of the event to be measured.

The ELEGANT V detector used a helium gas mixture TPC surrounded by arrays of scintillators coupled to PMTs, and solid foils contained $^{100}\mathrm{Mo}$ and $^{116}\mathrm{Cd}$ isotopes. The proposed MOON (Molybdenum Observatory Of Neutrinos) experiment is based on the techniques of ELEGANT V and will search for the $0\nu\beta\beta$ decay of $^{100}\mathrm{Mo}$ and will also act as a solar neutrino detector. MOON will be carried out in three phases. MOON-I will hold 30 kg $^{100}\mathrm{Mo}$ and have a sensitivity of $\langle m_{\beta\beta}\rangle \sim 160$ meV. MOON-II will hold 120 kg $^{100}\mathrm{Mo}$ and have a sensitivity of $\langle m_{\beta\beta}\rangle \sim 100$ meV. Finally MOON-III will house ~ 500 kg enriched to 85% $^{100}\mathrm{Mo}$ and hopes to reach a sensitivity of $\langle m_{\beta\beta}\rangle \sim 45$ meV.

The DCBA (Drift Chamber Beta Analyzer) experiment is a TPC containing source plates and permeated with a strong magnetic field (2 kG). The particle momentum will be extracted from the curvature of the track and backgrounds will be suppressed through event vertex reconstruction. The main design DCBA-T3 (now called MTD – Magnetic Tracking Detector[83]) will house Nd_2O_3 enriched to 60% $^{150}\mathrm{Nd}$. There is a single detector (named here as MTD-1) and modular detector (named here as MTD-50) design. The single detector design will house 32 kg of $^{150}\mathrm{Nd}$ and have a sensitivity of $\langle m_{\beta\beta}\rangle \sim 100$ meV after one year. The modular design will have 50 modules and house 600 kg $^{150}\mathrm{Nd}$ with a predicted sensitivity of $\langle m_{\beta\beta}\rangle \sim 30$ meV.

4.2.2 Tracking detector plus calorimeter experiments

Tracking detector plus calorimeter experiments are favored for their particle identification, event topology selection, and range of isotope choice. The NEMO-3 (Neutrino Ettore Majorana Observatory) detector is the only running experiment of this type and currently is the only running double-beta decay experiment as well. The NEMO-3 detector houses 7 kg of $^{100}\mathrm{Mo}$ (and others) with a projected sensitivity of $\langle m_{\beta\beta}\rangle \sim 0.3$-0.9 eV. The NEMO-3 detector is further discussed in Chap. 5.

The SuperNEMO experiment is the next generation detector based on the successful experimental approach of NEMO-3. SuperNEMO is not only bigger than NEMO-3

but implements new technologies to improve the tracking efficiency, calorimeter energy resolution, and most importantly the $0\nu\beta\beta$ detection efficiency. SuperNEMO is of modular design and will house a total of 100 kg of $^{82}\mathrm{Se}$ for a projected sensitivity of $\langle m_{\beta\beta}\rangle \sim$ 50-90 meV. The SuperNEMO detector is further discussed in Chap. 9.

Part I

Double beta decay of 96-Zr with NEMO-3

Chapter 5

The NEMO-3 experimental apparatus

The NEMO-3 detector is located at the Laboratoire Souterrain de Modane (LSM) in the Fréjus road tunnel connecting France and Italy. The detector was commissioned in February 2003 and has acquired 6 years of data. It is of cylindrical geometry measuring 5 m in diameter and 3 m in height Fig. 5.1. NEMO-3 is of heterogeneous design (as

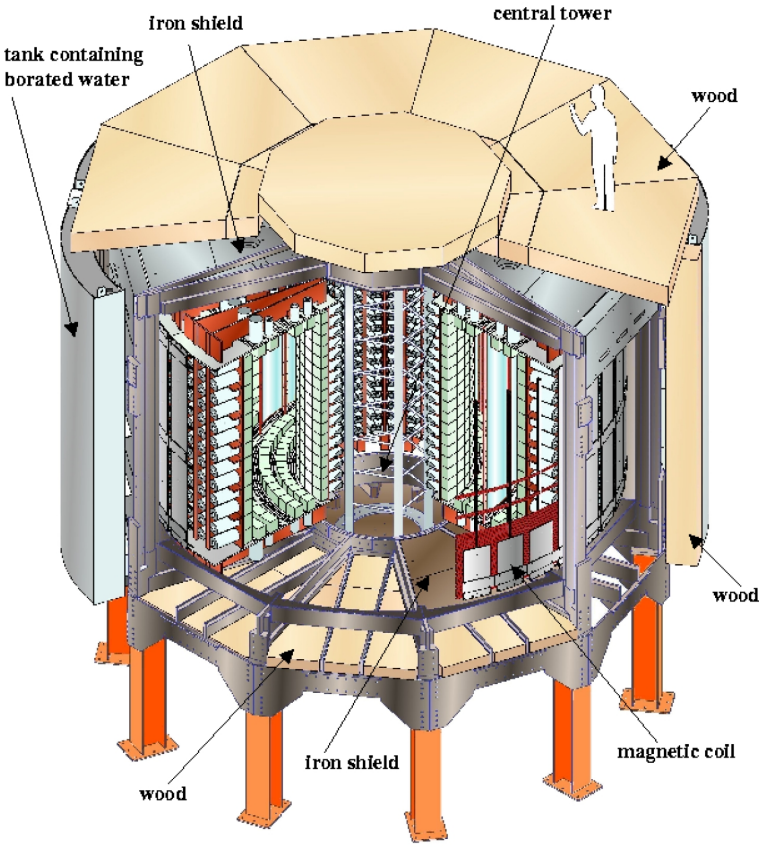

Figure 5.1: A cutaway view of the NEMO-3 detector.

discussed in Sec. 4.2) in which the radioactive sources do not make up part of the ac-

tive detector. The detector geometry is best described as a thick ring whose inner and outer radii are defined by the calorimeter walls. The calorimeter encloses the tracking chamber with the source foil defining the center radius of the ring as indicated in Fig. 5.2. This design facilitates the use of different sources and the detector con-

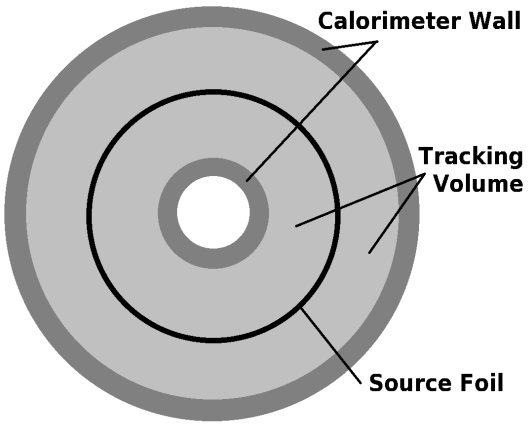

Figure 5.2: A simplified top-view of the NEMO-3 detector described as a thick ring.

tains 10 kg of seven candidate double-beta decay isotopes. The sources are distributed along suspended thin foils and surrounded by the vertical wires of the drift-cell tracking chamber. The drift-call wires are not specifically shown in Fig. 5.1 and Fig. 5.3 but are implied to be present. The drift-cell wires are thin to minimize electron scattering and operate in Geiger mode to maximize efficiency (Sec. 5.3). The tracking volume is enclosed by the calorimeter comprised of polystyrene scintillators coupled to photomultiplier tubes (PMTs). The detector is enclosed in a solenoid which generates a 25 Gauss magnetic field parallel to the Geiger cells. The detector is 4800 meters water equivalent (MWE) under ground to reduce the cosmic muon flux and passive shielding is used to suppress neutrons and γ-rays from entering the active detector volume.

5.1 Detector geometry

The detector can be described in both the Cartesian and cylindrical coordinate systems. The three dimensional Cartesian origin $(0, 0, 0)$ is defined as the center of the detector in x, y and z axies. When referring to individual sectors it is useful to describe

them in cylindrical coordinates which requires the transformations

$$R = \sqrt{x^2 + y^2}\,, \tag{5.1.1}$$

$$\phi = \begin{cases} \arcsin\left(\dfrac{y}{R}\right) & \text{if } x \geq 0 \\ \arcsin\left(\dfrac{y}{R}\right) + \pi & \text{if } x < 0 \end{cases}\,, \tag{5.1.2}$$

$$Z = z\,, \tag{5.1.3}$$

where ϕ is the polar angle. The detector is constructed from 20 constituent sec-

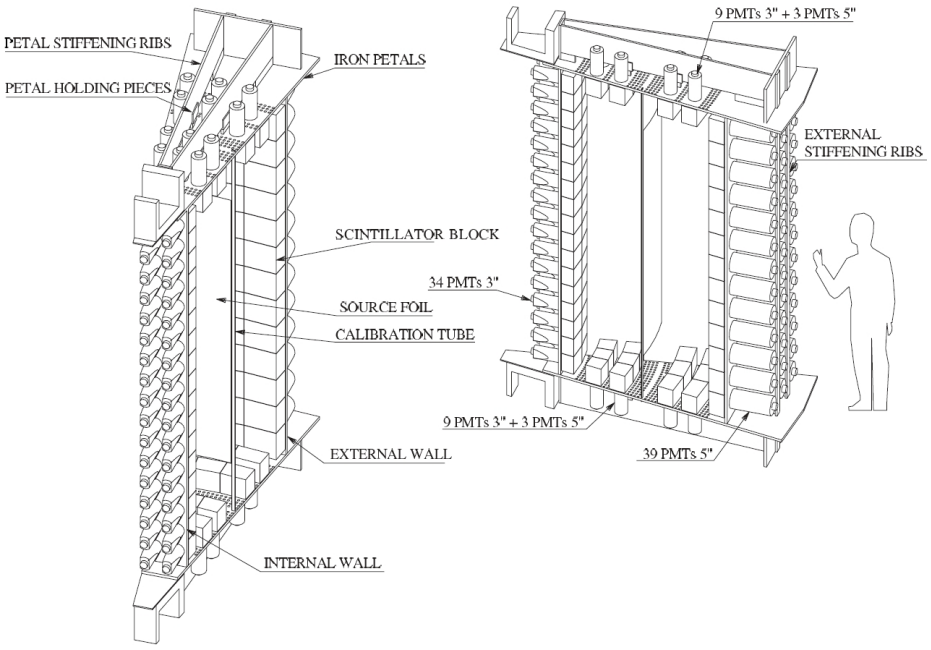

Figure 5.3: One sector of NEMO-3 depicting the source foils, scintillator blocks and PMTs. The Geiger cells are located between the internal and external walls.

tors (Fig. 5.3) numbered 00 to 19 with each sector occupying 18 degrees (0.314 radians) of ϕ. The sector number is therefore defined as

$$\text{sector number} = \phi \times \frac{20}{2\pi}\,, \tag{5.1.4}$$

where sector 00 begins at $\phi = 0$. In the z-axis, the detector spans from $Z = 120\,\text{cm}$ to $Z = -120\,\text{cm}$. Each sector is equipped with source foils located at $R = 155.5\,\text{cm}$ in cylindrical coordinates, Geiger cells, and calorimeter blocks which define the internal and external walls of the sector (Fig. 5.4).

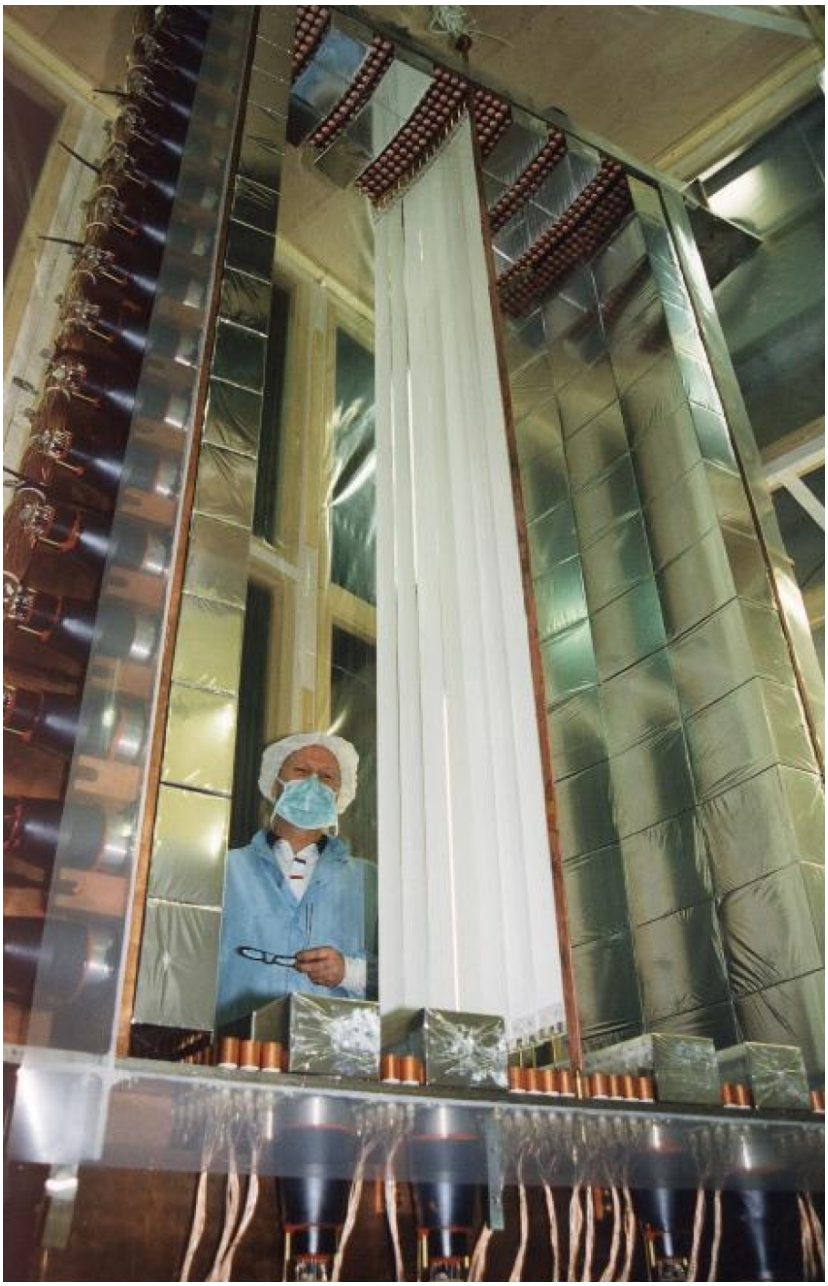

Figure 5.4: An image of sector 03 displaying the vertically suspended source foil (thin white rectangular sheet), the scintillators wrapped in aluminized Mylar (silver blocks), and the Geiger cell cathode rings (small copper cylinders).

5.2 The NEMO-3 double-beta decay isotopes

Seven double-beta decay isotopes, ^{100}Mo, ^{82}Se, ^{116}Cd, ^{130}Te, ^{150}Nd, ^{48}Ca, and ^{96}Zr are distributed throughout the detector as shown in Fig. 5.5. There is also a sector of ultra-pure copper (OFHC – oxygen-free high conductivity) which provides a radiopure sector to aid in understanding the external backgrounds. Each sector contains

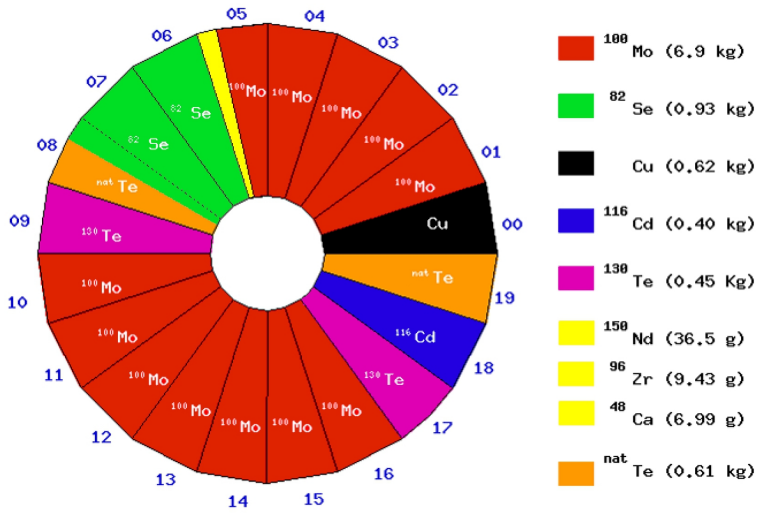

Figure 5.5: Distribution of sources throughout the 20 sectors of the NEMO-3 detector.

seven vertical foils measuring 2.5 m in height, 65 mm in width, and 30–60 mg/cm^2 in area density. The key signature for neutrinoless double-beta decay ($0\nu\beta\beta$) events is the emission of two electrons detected in the calorimeter with a total energy equaling that of the $Q_{\beta\beta}$ value of the isotope under study. It is therefore important to chose isotopes with relatively high $Q_{\beta\beta}$ values to suppress background contributions in the $0\nu\beta\beta$ energy region. ^{208}Tl and ^{214}Bi are consequently the most troublesome backgrounds due to large Q_β values of 4.99 MeV and 3.27 MeV. Gamma transitions from the decays can have energies up to 2.615 MeV (in the case of ^{208}Tl), therefore isotopes with $Q_{\beta\beta} > 2.6$ MeV are chosen to suppress the external background. The natural isotopic abundance is also considered for selection criteria because in general the higher the natural abundance, the less expensive the enrichment process. Typically isotopes with natural abundance greater than 2% were chosen. Tab. 5.1 summarizes the seven isotopes, their $Q_{\beta\beta}$ values and natural abundances. ^{130}Te is included for study because its $2\nu\beta\beta$ half-life has not yet been directly measured and ^{48}Ca is included because of its impressive $Q_{\beta\beta}$ value and its "doubly magic" nucleus leads to easier shell model calculations. It is interesting to tabulate the phase-spaces ($G^{2\nu}, G^{0\nu}$) for the selected NEMO-3 sources for the $2\nu\beta\beta$ and $0\nu\beta\beta$ decays because a larger phase-space generally translates to a shorter half-life (see Eq. 3.2.3).

Table 5.1: Double-beta decay isotopes used in NEMO-3. Except for ^{130}Te, all isotopes have $Q_{\beta\beta}$ values greater than the 2.6 MeV γ-ray transition from ^{208}Tl. All isotopes have a natural abundance greater than 2% except for ^{48}Ca. Phase-space values are published in Ref. [43].

Transition	$Q_{\beta\beta}$ (keV)	Abundance (%)	$G^{2\nu}$ (yr^{-1})	$G^{0\nu}$ (yr^{-1})
^{130}Te $\rightarrow$ ^{136}Xe	2528.8 $\pm$ 2.1	33.8	4.8×10^{-18}	1.7×10^{-25}
^{116}Cd $\rightarrow$ ^{116}Sn	2804.7 $\pm$ 4.2	7.5	8.0×10^{-18}	1.9×10^{-25}
^{82}Se $\rightarrow$ ^{82}Kr	2995.2 $\pm$ 3.3	9.2	4.3×10^{-18}	1.1×10^{-25}
^{100}Mo $\rightarrow$ ^{100}Ru	3034.8 $\pm$ 6.3	9.6	9.4×10^{-18}	1.8×10^{-25}
^{96}Zr $\rightarrow$ ^{96}Mo	3350.0 $\pm$ 3.5	2.8	1.9×10^{-17}	2.2×10^{-25}
^{150}Nd $\rightarrow$ ^{150}Sm	3367.1 $\pm$ 4.9	5.6	1.2×10^{-16}	8.0×10^{-25}
^{48}Ca $\rightarrow$ ^{48}Ti	4272.0 $\pm$ 4.1	0.187	4.0×10^{-17}	2.4×10^{-25}

5.2.1 The ^{96}Zr source foil

The foil was made of two samples of ^{96}Zr manufactured in two separate locations: ITEP (Institute of Theoretical and Experimental Physics, Moscow) and INR (Institute of Nuclear Research, Moscow). Zirconium-dioxide (ZrO_2) was enriched through an electromagnetic separation technique to 57.3 $\pm$ 1.4% ^{96}Zr and purified through a chemical process. The ITEP sample has 9.6 g ZrO_2 enriched to 4.1 $\pm$ 0.1 g of ^{96}Zr, and the INR sample has 12.4 g ZrO_2 enriched to 5.3 $\pm$ 0.1 g of ^{96}Zr for a combined ^{96}Zr mass of 9.4 $\pm$ 0.2 g.

The ^{96}Zr samples are located on the seventh foil of sector 05 and occupy a sector-space of 5.87-5.99 (Sec. 5.1) and extend $115 > Z > 0$ cm in the Z-axis. The bottom half of the foil is occupied with the ^{48}Ca source, ^{150}Nd is located in the sector to the left, and a calibration tube to the right (Fig. 5.6). The ZrO_2 powder is sandwiched between two sheets of 19 μm thick Mylar (referred to as the backing film) and held together with a glue made from a mixture of water and polyvinyl-alcohol (PVA). All materials have been selected for their radiopurity measurements from a high-purity Germanium detector (HPGe). The activity limits of the ZrO_2 powder plus Mylar backing film are tabulated in Tab. 5.2 at the 95% confidence level (CL) in units of milliBecquerel per

Figure 5.6: View of the source foil production for sector 05. The two silver foils are metallic ^{100}Mo, the three black foils are composite ^{100}Mo, the white foil adjacent to the black foils is the composite ^{150}Nd, and the white foil being held is the composite ^{96}Zr and ^{48}Ca foil.

kilogram (mBq/kg).

Table 5.2: Radioactivity limits for the ^{96}Zr source foil at the 95% confidence level in units of mBq/kg obtained with a high purity germanium detector. The measured mass represents the full mass of the ZrO_2 powder plus the Mylar backing film.

		Activity (mBq/kg)					
source	mass (g)	^{40}K	^{235}U	^{234}Th	^{214}Bi	^{228}Ac	^{208}Tl
ITEP ZrO_2	13.7	<217	<7	<222	<16	<23	<10
INR ZrO_2	16.6	583 ± 167	<10	<221	<14	<27	<5.5

5.3 The tracker

The tracking volume is divided in half by the source foil. It is made up of 6180 vertically aligned, octagonal drift cells operating in Geiger mode (Geiger cells). Geiger mode is so-called because any amount of ionization above threshold causes a large binary signal whereas in proportional mode the signal amplitude is proportional to the amount of ionization. Geiger mode is advantageous over proportional mode because it offers higher efficiency and minimizes electron energy loss as a consequence of the reduced gas density within the tracking volume.

A Geiger cell signal is the result of ionization near the anode wire. The free electrons from ionized helium are accelerated towards the anode wire and ionize further atoms creating an avalanche. The avalanche creates a detectable signal (tens of mV) without amplification. On average one or more UV photons are emitted from the atoms as they relax to ground state and the UV photons further ionize the gas. The small volume around the anode wire becomes heavily ionized (burnt out) allowing the UV photons to travel further along the wire before ionizing more gas. This process leads to propagation of the plasma in both directions along the wire until termination at the ends of the cell.

The NEMO-3 Geiger cells are layered in a 4-2-3 configuration on both sides of the source foil (Fig. 5.7) meaning there are four layers of cells closest to the source foil proceeded by two layers of cells and three layers of cells at the internal and external walls. The layering is a result of optimizing the two-electron (ee) detection efficiency which depends on the vertex resolution at the source foil and the detection of the electrons in the calorimeter. Each Geiger cell is 3.0 cm in diameter and 2.7 m long with a single anode wire surrounded by eight cathode wires. The stainless steel wires, chosen for robustness, are 50 μm in diameter were chosen to suppress aging effects and promote good plasma propagation along the wire. The gas mixture in the chamber is 95% helium, 4% ethyl alcohol, 1% argon and 0.15% water with a total pressure of ~ 10 mbar above atmospheric pressure. The use of helium allows good transparency (minimized multiple scattering due to low Z) of the chamber. The cell would produce a continuous discharge without alcohol acting as a quencher to limit the photoionization process of the fired cell. The quenching agent also reduces the probability of triggering neighboring cells. Argon and water are added to the mixture to increase the plasma propagation

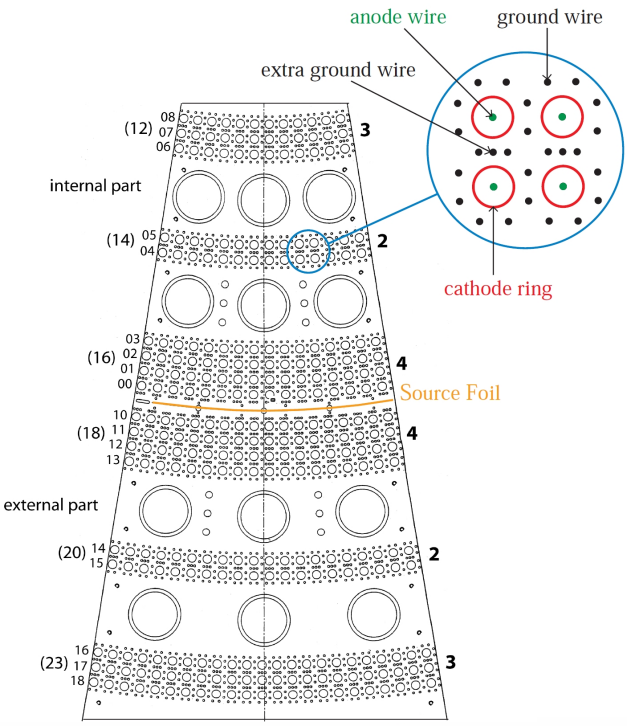

Figure 5.7: The top view of one NEMO-3 sector showing the layout of the drift cells and PM cavities.

efficiency and stabilize the process. The longitudinal plasma propagation velocity is $\sim 5\,\text{cm}/\mu\text{s}$ corresponding to a full propagation time of $\sim 52\,\mu\text{s}$ with an efficiency of $\sim 95\%$. The average transverse and longitudinal resolution of the individual Geiger cells is 0.6 mm (σ) and 0.3 cm (σ) respectively. These values differ from the vertex resolutions quoted in Sec. 6.2.2 and 6.2.3 due to the error introduced by the reconstruction algorithm.

5.4 The calorimeter

The NEMO-3 calorimeter is comprised of 1940 units. Each unit has a scintillator, two lightguides and a photomultiplier tube. The dimensions of the scintillator are $20\times20\times10\,\text{cm}$. This scintillator thickness was chosen to maximize the γ-ray detection efficiency. The probability for a γ-ray of energy 0.5 MeV to interact with a 10 cm thick scintillator is $\sim 50\%$. The scintillator material is polystyrene (PST) and chosen primarily for its low Z value compared with mineral scintillators. A low Z is advantageous because it reduces the back-scattering of low energy electrons. PST is also preferred for its conventional mass production, uniformity, and radio-purity. The

PST is doped with scintillation agent p-Terphenyl (PTP), and wavelength shifter 1,4-bis(5-phenyloxazol-2-yl) benzene (POPOP). The four lateral sides of the scintillator are wrapped with 350 μm of polytetrafluoroethylene (PTFE) for diffusive reflection and with the exception of the lightguide coupling area, the six faces are covered with 12 μm thick aluminized Mylar over the PTFE. The lightguides are constructed from poly (methyl methacrylate) (PMMA), whose purpose is to couple the scintillator to the PMT while isolating the PMT from the helium gas in the tracking volume and all PMTs are fitted with Mu-metal shielding to protect them from the magnetic field Fig. 5.8. The PMTs are 3" (R6091) and 5" (R6594) Hamamatsu types which are specially designed for NEMO-3, having low radioactivity glass and other components, fast signal rise-time and good linearity. The 3" PMTs have 12 dynodes and a flat photo-cathode and the 5" PMTs have 10 dynodes and a hemispherical photo-cathode. All calorimeter counters are individually characterized and information such as gain, dark noise, and linearity are placed into a database. The counters begin deviating from linearity above 4 MeV which complies with the design specification that PMTs be linear up to the energy of the $Q_{\beta\beta}$ of the candidate source isotopes. The calorimeter energy resolution and timing resolution is 14–17% (FWHM at 1 MeV) and 250 ps (σ at 1 MeV) respectively.

5.5 The radon trapping facility

Backgrounds to NEMO-3 will be discussed in detail in the following chapter, but an important component of the detector description is the radon trapping facility. ^{214}Bi is one of the ^{222}Rn daughters and is particularly troublesome because of its high $Q_\beta = 3.27$ MeV (Sec. 5.2). It was discovered that radon was entering the detector by diffusion through the glued joints of the sectors. To achieve the design sensitivity to the $0\nu\beta\beta$ half-life, the amount of radon inside the detector needed to be reduced by an order of magnitude. This was achieved with the realization of the radon trapping facility, based on the system developed for Super-Kamiokande [89]. Fresh air is compressed and cooled to -50^{o} C and flushed through activated charcoal which is also cooled to -50^{o} C. The principle (see Fig. 5.9) is that the cooled ^{222}Rn will be adsorbed by the extremely porous charcoal (large surface area) for long enough to decay ($T_{1/2} = 3.8$ days). Many types of charcoals were measured at various temperatures before the ultimate realization. The dominant factors determining the radon trapping

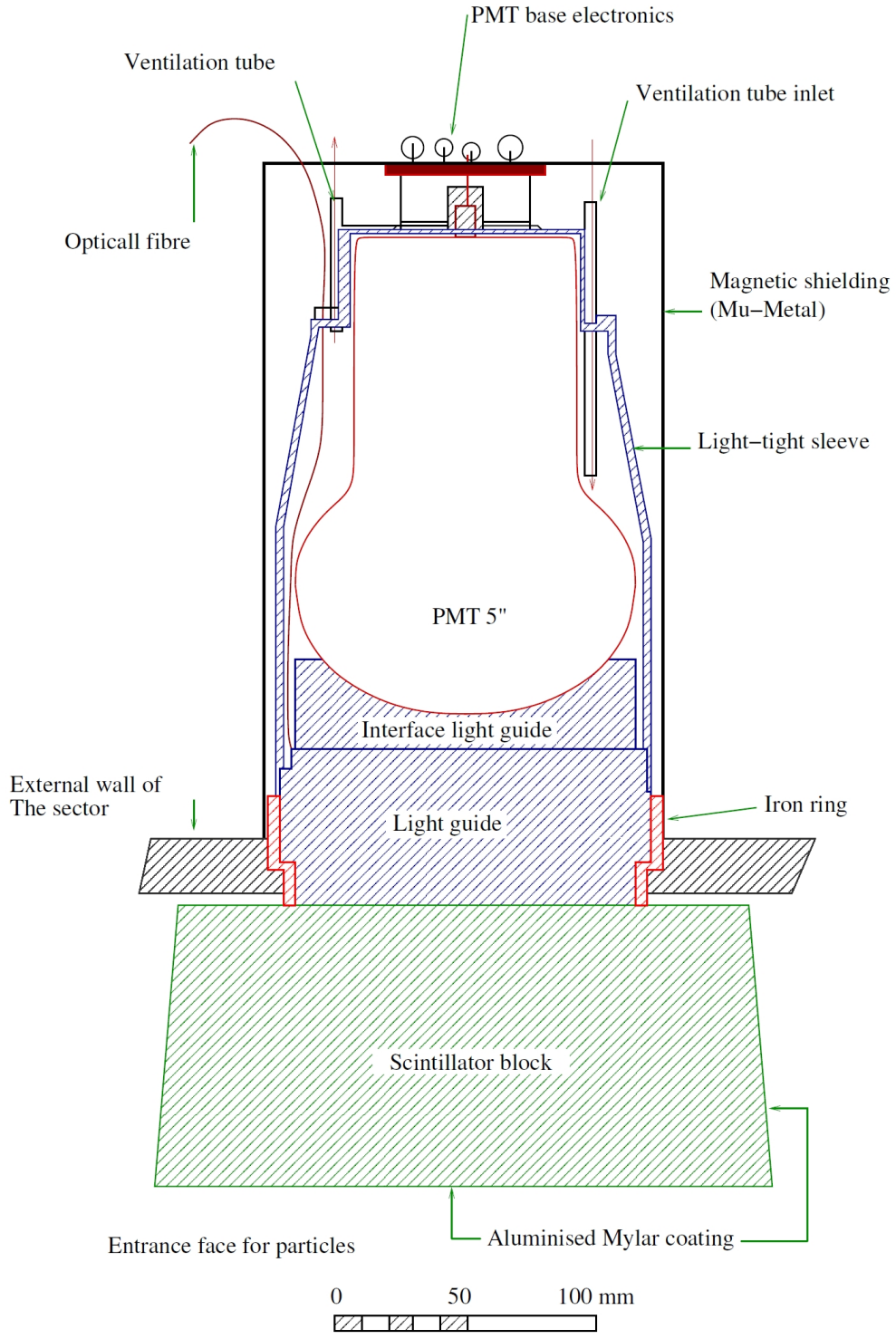

Figure 5.8: Schematic of one calorimeter unit showing the coupling of the scintillator to lightguides and PMT and method for isolating the PMT from the helium environment of the tracking chamber.

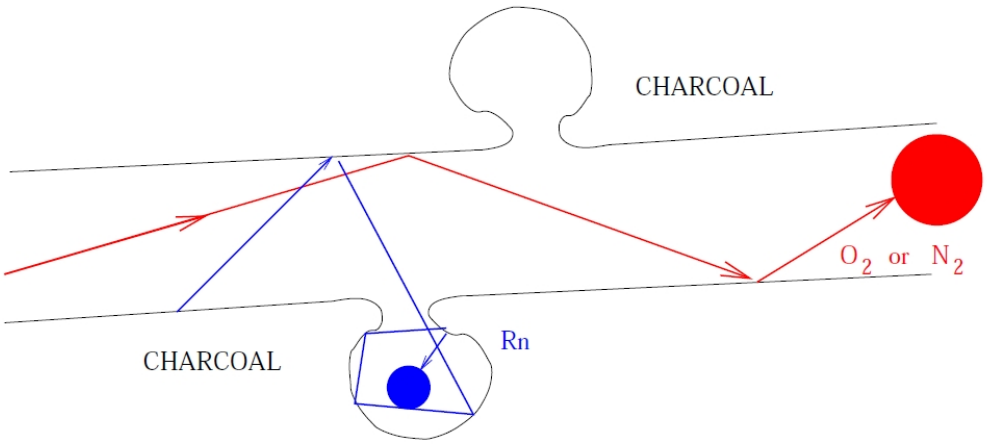

Figure 5.9: The principle of radon adsorption using activated charcoal.

efficiency are the physical size of the charcoal pores, the spatial density of charcoal pores, and the temperature of the air and charcoal. In general, as the temperature of the air and charcoal decreases, the radon trapping efficiency increases due to the decreased kinetic energy of the radon atom. The temperature limitation in the case of NEMO-3 is the expensive technology needed to cool below -55^{o} C. The fresh air enters the purification system with a radon activity of $\sim 15\,\mathrm{Bq/m^3}$ and exits with an activity of $\sim 0.015\,\mathrm{Bq/m^3}$ for a reduction factor of about 1000. The NEMO-3 detector is enclosed in an airtight polyethylene tent in which the purified air is flushed through to sustain the low radon environment immediately surrounding the detector. After the injection of pure air around the detector, the total radon activity inside the detector decreased from 1.2 Bq to 0.2 Bq. Due to detector component out-gassing, the radon reduction factor within the detector is not as large as that from the trapping facility.

5.6 The electronics and calibration

The NEMO-3 detector comprises an independent calorimeter and tracking detector and has interdependent triggering and data readout systems. This design allows flexibility for multiple triggering criteria which permits different tests to adjust and calibrate the detector.

5.6.1 Calorimeter electronics

The mean high voltage (HV) for the 5" PMTs is positive 1350 V and for the 3" PMTs is positive 1800 V. The HV is generated with 3 CAEN power supplies capable

of 2200 V at 1.2 mA maximum per channel. Each of the 3 power supplies is equipped with 10 modules, each containing 24 HV channels for a total of 240 HV channels per power supply. The HV is transferred to each sector via 9 distribution boards. Each distribution board has 4 HV inputs which are each split in parallel to 3 outputs. Each output is controlled with an integrated 2-resistor voltage divider to allow fine tuning of the individual PMT HV. This configuration provides 2160 channels of controllable HV.

The 97 PMTs per sector are divided by the source foil into 46 PMT channels for the internal half and 51 PMT channels for the external half and each PMT channel has a dedicated signal processing daughter card. There are either 46 or 51 daughter cards per motherboard and a total of 40 motherboards distributed among 3 VME (Versa Module Europa) crates. The sequence of events is initiated by a PMT signal exceeding the low level threshold of 7 mV which corresponds to 23 keV. This sends a TTL (TransistorTransistor Logic) *START* command to the TDC (Time to Digital Converter) and opens the charge integration gate for 80 ns. The high level threshold is set to 48 mV or 150 keV and triggers the system (first level trigger) if the desired multiplicity of active PMTs is achieved, which typically is one PMT. The system then reads out the relevant TDC and ADC data and saves to disk. The TDCs have a timing resolution of 53 ps/channel for 12 bits for a total time of ~ 200 ns. The ADCs have a charge resolution of 0.36 pC/channel (~ 3 keV/channel) for 12 bits providing an energy range up to ~ 12 MeV.

5.6.2 Tracking detector electronics

Typical HV on the anode wires is 1620-1650 V and is supplied by two CAEN power supplies, each with 16 HV channels. The tracker is made up of 18 concentric layers of Geiger cells and due to electrostatic effects, each layer generally requires a slightly different voltage to maintain a consistent efficiency. For this reason each concentric layer of Geiger cells is powered by one HV channel, with the exception of the 9 outer most layers which are each powered by two HV channels (because more current is required). Distribution boards are used for the fine control of the HV and for decoupling the anode wire signals to be sent to acquisition boards. Each of the 20 sectors needs 8 distribution boards. Each distribution board holds 15 daughter boards and each daughter board contains 8 channels. The 15 daughter boards are distributed

such that 5 daughter boards are for anode signals, 5 for the high cathode ring (HC) and 5 for the low cathode ring (LC).

The application specific integrated circuits (ASICs) are programmed to amplify and discriminate the signals above threshold before initiating the TDCs for the anode (tdc_A), low cathode ring (tdc_{LC}) and high cathode ring (tdc_{HC}). In the general case, the anode signal triggers the *START* of the TDCs (tdc_A, tdc_{LC}, and tdc_{HC}) but primarily the fast timing from the calorimeter triggers the *START* of tdc_A. In the case of a β-type event, the first level trigger (T1) from the calorimeter has already begun the tdc_A measurement, in which case the anode signal triggers *STOP* to tdc_A and *START* to tdc_{LC} and tdc_{HC}. The time difference between tdc_A *START* and *STOP* is the anode time t_A and corresponds to the transverse drift time from the point of ionization. The signals from cathode rings *STOP* their associated TDCs and those time differences correspond the longitudinal plasma propagation times t_{LC} and t_{HC}.

An important characteristic of the tracking detector is the ability to wait up to 710 μs after T1 for delayed Geiger hits. ^{214}Bi is, as mentioned earlier, a troublesome background to NEMO-3 because of its high Q_β, but where nature provides a problem, it also provides a solution. ^{214}Po is the daughter isotope and decays via α-decay with a half-life of 164.3 μs. The event signature of an α-decay is a short straight ionization track in the tracking detector and no energy deposit in the calorimeter, being quite dissimilar from other event signatures. NEMO-3 is able to veto a large fraction of ^{214}Bi events by tagging delayed α-decays within the 710 μs time window.

5.6.3 The NEMO-3 trigger system

The NEMO-3 detector has a 3 level (T1, T2, and T3) triggering system. T1 is based on the desired multiplicity of PMT signals with energy greater than 150 keV required for successful readout. For standard data acquisition only one PMT is required but for example during calibration runs using ^{60}Co two coincident PMT signals are required (Sec. 5.6.4). T2 is based on activated Geiger cells in at least three of the nine layers in the half-sector. Furthermore, there must be at least two triggered cells in one of the three groups (0-3, 4-5, 6-8) of layers as exampled in Fig. 5.10. Examples of activated Geiger cells which do not produce a T2 trigger are demonstrated in Fig. 5.11. T3 is only used for calibration runs because it modifies the T2 tracking algorithm to bias tracks

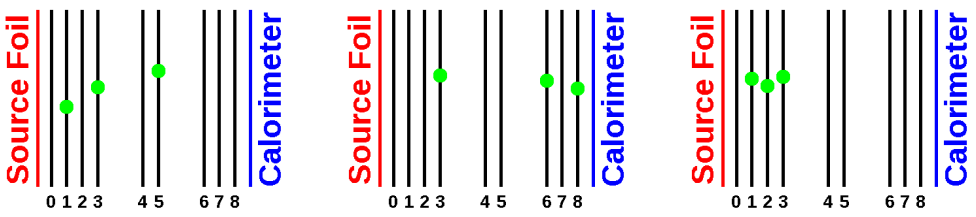

Figure 5.10: Examples of activated Geiger cells which produce a second level trigger, T2.

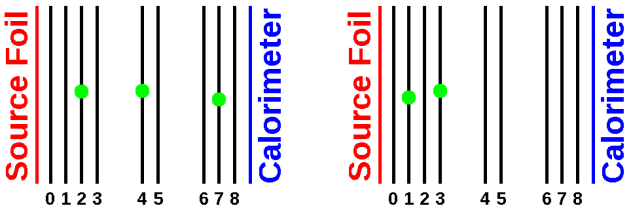

Figure 5.11: Examples of activated Geiger cells which do not produce a second level trigger, T2.

whose origin is near calibration tubes (where sources are positioned for the calibration of the detector).

5.6.4 Energy and timing calibrations

Each of the 20 sectors of the detector is equipped with a calibration tube. These are vertical copper pipes located at the foil's edge and at the same cylindrical radius as the foil. Radioactive sources are inserted and used to calibrate the different systems and also allows analysis of the detector related systematic errors. The absolute energy calibration of the PMTs is realized monthly with ^{207}Bi. Periodically ^{90}Sr sources are used in conjunction with the ^{207}Bi sources to provide a third point for the absolute gain calibration. ^{207}Bi provides K-shell conversion electrons at 482 keV and 976 keV [90] and the endpoint of the β-spectrum of ^{90}Y is at 2.283 MeV (^{90}Sr decays to ^{90}Y with a period of 2.671 days). Timing calibration of the calorimeter is achieved by measuring the relative time difference between two coincident γ-rays emitted by ^{60}Co sources with energies of 1173 and 1332 keV. Relatively intense sources are used because this measurement does not require the tracking chamber. Gain stability of the PMTs is monitored twice a day with a calibrated laser light injection system. Six reference PMTs fitted with ^{207}Bi sources and a reference photodiode monitor the laser light being transmitted via optical fibers to the PMT blocks. Using a variable optical attenuator, the

laser calibration system provides measurements for linearity calibration up to 12 MeV.

5.7 Magnetic coil and passive shielding

5.7.1 The magnetic coil

A 25 Gauss magnetic field parallel to the Geiger cells is achieved with passing ~ 30 A through 203 loops of copper bar to form a solenoid enclosing the NEMO-3 detector. The purpose of the magnetic field is to identify electrons from positrons by the curvature of their tracks. Due to the magnetic field, the charge reconstruction is 97% efficient for 1 MeV electrons and positrons.

5.7.2 Cosmic muon suppression

The detector was placed at a depth of 4800 m water equivalent to suppress the cosmic muon flux. The muon flux at the NEMO-3 location (LSM) has been measured to be $5 \times 10^{-5}\,\mathrm{m^{-2}s^{-1}}$ which is a reduction of about a factor of one million from the muon flux at sea level.

5.7.3 The iron shield

The iron shield is 20 cm thick and covers 4π solid angle of the detector. The shield suppresses the γ-ray flux caused by γ-ray emitting radioactive decays in the surrounding rock and γ-rays emitted from neutron capture. The iron also acts as a flux return for the solenoid. As with other materials, the iron was selected for its radiopurity.

5.7.4 The neutron shield

High energy γ-rays are troublesome for NEMO-3 and neutron capture contributes to this problem. One strategy is to stop and suppress fast, thermal and epithermal neutrons from outside the iron shield so that the accompanying γ-rays will be absorbed by the iron. This is accomplished with 20 cm of paraffin, 35 cm of borated water, and 28 cm of wood is used where borated water is inconvenient. This configuration is optimized to slow down fast neutrons with energies of a few MeV and suppress thermal neutrons.

Figure 5.12: Picture of the completed NEMO-3 detector including all passive shielding, the airtight radon-free tent, and the cooling and ventilation system.

Chapter 6

General analysis technique

This chapter discusses the major steps of the analysis procedure required for background estimation, $2\nu\beta\beta$ half-life measurement, and search for $0\nu\beta\beta$ decay. The software chain includes generating simulated events (Sec. 6.1), propagating simulated events through the detector description (Sec. 6.1), reconstructing the data and simulation (Sec. 6.2), preprocessing (Sec. 6.3), and finally statistical analysis (Sec. 6.4).

6.1 Monte Carlo simulations

The event generator DECAY0 [91] contains the kinematics and branching ratios of α, β, and γ decays for many isotopes and simulates a comprehensive selection of $2\nu\beta\beta$ and $0\nu\beta\beta$ decay modes and Majoron emission processes to ground state and excited states. DECAY0 is used to generate all associated external and internal backgrounds to NEMO-3 as well as the $2\nu\beta\beta$ and $0\nu\beta\beta$ signal from source isotopes. Generated events are propagated by GEANT-3.21 [92] through a full description of the detector simulating the kinematics of various interactions according to their full and differential cross-sections. Simulated events are in the same format as the raw data to allow for an identical reconstruction process.

6.2 Data and Monte Carlo reconstruction

The reconstruction of data and MC is identical with one exception. The reconstruction package (NEMOR) knows nothing about the status of the detector or scintillator characterizations, so this information is applied during the reconstruction of the raw MC via the NEMO database. The database is a record of the detector status for each period of data acquisition and contains information such as PMT and scintilla-

tor characteristics, drift cell characteristics, and calibration data. The generated MC events (Sec. 6.1) are distributed among the data acquisition periods (runs) as a function of runtime and for each acquisition period the associated run status from the database is applied. Reconstructed events of any particular MC sample represent the full decay scheme kinematics and includes energy smearing due to intrinsic calorimeter energy resolution and uncertainty in the energy calibrations.

6.2.1 Event topology and particle identification

The detector (and therefore reconstruction software) is capable of sophisticated particle identification and event topologies. Electrons produce an ionization trail through the tracking detector with a negative-type curvature due to the magnetic field and deposit their energy in the calorimeter block. Positrons create a track with a positive-type curvature through the tracking chamber before depositing their energy in the calorimeter. Gamma-rays do not ionize the gas in the tracker volume and the probability for interaction with a single calorimeter block is $\sim 60\%$ for 0.5 MeV γ-rays. In comparison the total gamma efficiency of the detector is $\sim 50\%$ for 0.5 MeV γ-rays. Alpha particles are identified by their short straight ionization trails in the gas volume of the tracking detector and do not deposit energy in the calorimeter.

Time-of-flight (TOF) information is valuable to identify external γ-rays originating from detector components (other than the source foil) which cross the sector and Compton scatter in the source foil (Fig. 6.1a) mimicking $e\gamma$-type events and more importantly Compton scatter in the scintillator block producing crossing electrons (Fig. 6.1b) which mimic $\beta\beta$-type events [93]. The event topologies studied in this analysis include the single electron channel ($1e$), the electron plus gamma channel ($e\gamma$), and the two electron channel (ee). A typical topology of an ee event is displayed in Fig. 6.2. Other topologies of analysis include β-decay followed by a delayed α-decay ($e\alpha$) as mentioned in Sec. 5.6.2, an electron plus two γ-rays ($e\gamma\gamma$) and an electron plus three γ-rays ($e\gamma\gamma$).

6.2.2 The single particle vertex resolution

The quality of the vertex reconstruction has been analyzed with $^{207}\mathrm{Bi}$ sources positioned at $Z = 90$ cm, $Z = 0$ cm, and $Z = -90$ cm in each calibration tube of each sector (Sec. 5.1). The transverse $R\phi$ and longitudinal Z coordinates of each source

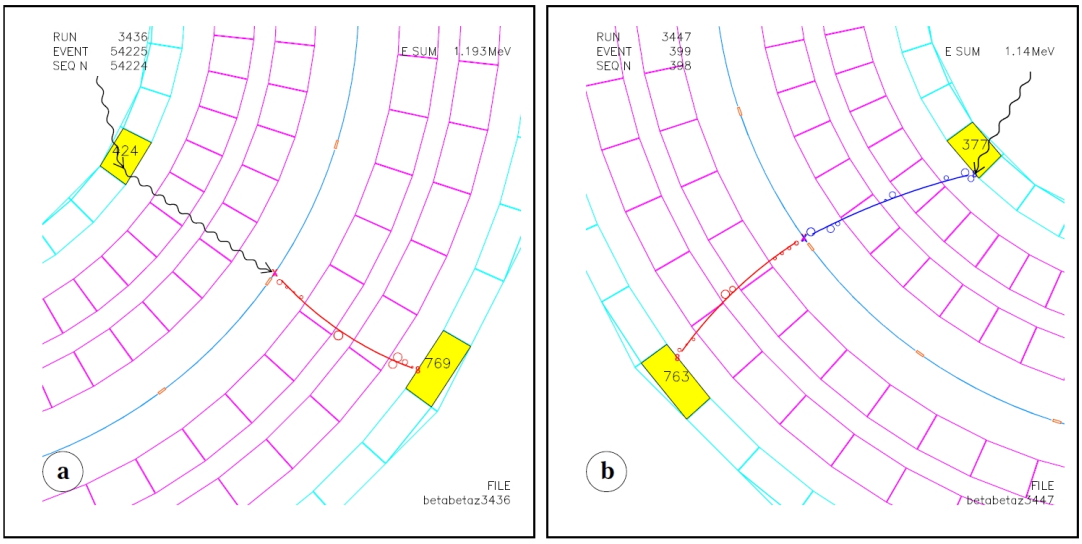

Figure 6.1: Examples of $e\gamma$-external (a) and crossing electron (b) events viewed from the top. Presumed γ-rays are superimposed on the event display.

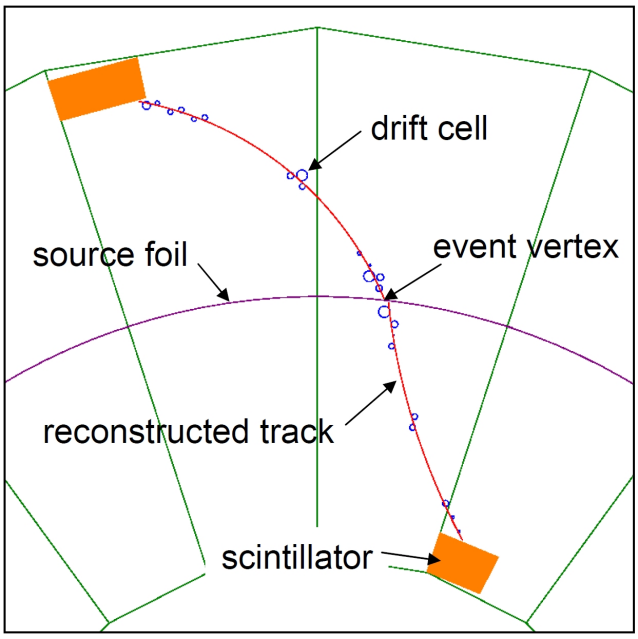

Figure 6.2: Example of a typical ee event viewed from the top depicting the source foil, scintillators, and event vertex.

is known to an accuracy of 1 mm. ^{207}Bi emits conversion electrons at energies of $\sim$0.5 MeV and $\sim$ 1 MeV allowing two average transverse resolutions to be determined,

also published in Ref. [94]

$$\sigma_{R\phi}(0.5\,MeV) = 0.3\,\mathrm{cm}\,, \tag{6.2.1}$$

$$\sigma_{R\phi}(1\,MeV) = 0.2\,\mathrm{cm}\,. \tag{6.2.2}$$

The longitudinal resolution σ_Z depends on both the energy and position, so the top ($Z = 90\,\mathrm{cm}$) and bottom ($Z = -90\,\mathrm{cm}$) resolutions are compared to the center ($Z = 0\,\mathrm{cm}$) resolution at the two $^{207}\mathrm{Bi}$ energies, also published in Ref. [94]

$$\sigma_{Z=0}(0.5\,MeV) = 0.6\,\mathrm{cm} \quad \text{and} \quad \sigma_{Z\pm90}(0.5\,MeV) = 0.8\,\mathrm{cm}\,, \tag{6.2.3}$$

$$\sigma_{Z=0}(1\,MeV) = 0.4\,\mathrm{cm} \quad \text{and} \quad \sigma_{Z\pm90}(1\,MeV) = 0.5\,\mathrm{cm}\,. \tag{6.2.4}$$

It is important to note that the resolution values quoted in Sec. 5.3 were for the individual Geiger cells without the introduction of errors due to the reconstruction algorithm.

6.2.3 The two electron vertex resolution

The $\beta\beta$ analysis reconstructs events with two tracks coming from the same vertex. It is therefore important to study the two electron vertex resolution in order to check the measured transverse and longitudinal dispersions $\delta R\phi$ and δZ respectively, and are defined as the distance between the vertices associated with the two reconstructed tracks. Two simultaneous electron events from $^{207}\mathrm{Bi}$ sources (relative intensity of $\sim 2\%$) is used to build the $\delta R\phi$ and δZ distributions which produce the resolutions, as published in Ref. [95]

$$\sigma(\delta R\phi) = 0.6\,\mathrm{cm} \quad \text{and} \quad \sigma(\delta Z) = 1.3\,\mathrm{cm}\,. \tag{6.2.5}$$

The reconstruction algorithm has been optimized to minimize the difference between the two track vertices and this improves the transverse resolution to $\sigma(\delta R\phi) = 0.1\,\mathrm{cm}$ which allows the distinction between source foil strips in a given sector. This is crucial for sectors composed of different sources, for example sector 05 contains $^{100}\mathrm{Mo}$, $^{150}\mathrm{Nd}$, $^{48}\mathrm{Ca}$, and $^{96}\mathrm{Zr}$ source strips.

6.3 Data and MC preprocessing

Specific event vertex location and event topology are selected for preprocessing the data and MC. A plot of $1e$ events in Fig. 6.3 show the $^{96}\mathrm{Zr}$ ITEP source with $115 > Z > 65$, the $^{96}\mathrm{Zr}$ INR source with $65 > Z > 0$, the $^{48}\mathrm{Ca}$ disks with $0 > Z >$ -60,

and empty Mylar at $Z <$ -60. Using this positional information, events with a vertex originating from the ^{96}Zr area are selected for analysis. The three channels of the

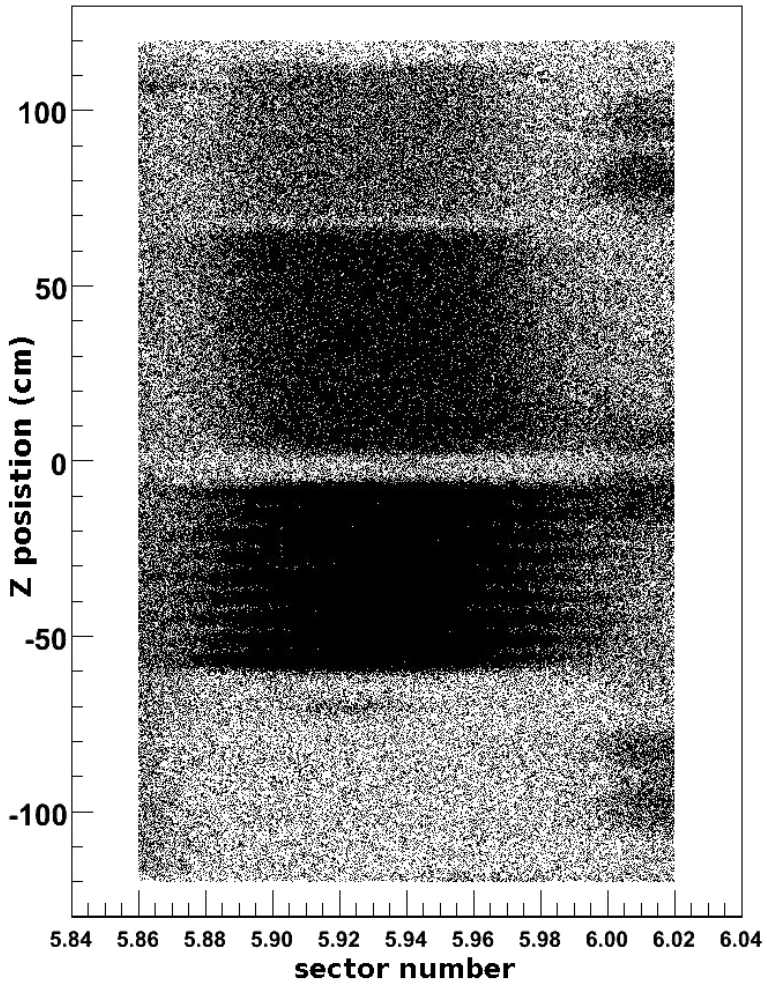

Figure 6.3: Single electron event vertices (black dots) in sector 05 show three active partitions (^{96}Zr ITEP, ^{96}Zr INR, and ^{48}Ca). The ^{96}Zr ITEP source is located $115 > Z > 65$, the ^{96}Zr INR source positioned $65 > Z > 0$, and the ^{48}Ca source with $0 > Z >$ -60.

^{96}Zr analysis are the $1e$, $e\gamma$, and ee channels and each has a loosely defined set of selection criteria which checks the event vertex location, the track curvature and the energy deposited in the scintillator. The general selection criteria are further refined during the analysis.

6.4 Statistical analysis package

The statistical analysis package ROOTANA is written in C/C++/ROOT and is the main software used for sophisticated data analysis such as internal and external event vertex hypotheses (Sec. 6.4.1 and 6.4.2), likelihood fitting (Sec. 6.4.3), and excluding the signal at predefined confidence levels (Sec. 6.4.5).

6.4.1 The two electron internal vertex hypothesis

The triggered TDC timing information t_i^{tdc} from the two PMTs ($i = 1, 2$) is used to compute the probability of the event origin being inside the source foil. Ionizing particles are characterized by their track length l_i and the energy deposited in the calorimeter E_i and each particle's time-of-flight (t_i^{tof}) is defined in natural units as

$$t_i^{tof} = \frac{l_i}{\beta_i}\,, \tag{6.4.1}$$

where

$$\beta_i = \frac{\sqrt{E_i(E_i + 2m_e)}}{E_i + m_e}\,, \tag{6.4.2}$$

and E_i includes corrections for the energy calibration and energy loss through the gas of the tracking volume. The time of emission assuming internal origin t_i^{int} of each particle is

$$t_i^{int} = t_i^{tdc} - t_i^{tof} = t_i^{tdc} - \frac{l_i}{\beta_i}\,, \tag{6.4.3}$$

and consequently the χ^2_{int} variable is written

$$\chi^2_{int} = \frac{\left(\left(t_2^{tdc} - \dfrac{l_2}{\beta_2}\right) - \left(t_1^{tdc} - \dfrac{l_1}{\beta_1}\right)\right)^2}{\sigma^2_{t^{int}}}\,. \tag{6.4.4}$$

Variable $\sigma^2_{t^{int}}$ is the sum of errors on the time σ_t, energy σ_E and track length σ_l and is written

$$\sigma^2_{t^{int}} = \sum_{i=1}^{2} \left(\frac{\partial t^{int}}{\partial t_i^{tdc}}\right)^2 \sigma^2_{t_i^{tdc}} + \left(\frac{\partial t^{int}}{\partial \beta_i}\right)^2 \sigma^2_{\beta_i} + \left(\frac{\partial t^{int}}{\partial l_i}\right)^2 \sigma^2_{l_i}\,, \tag{6.4.5}$$

which has the more explicit form

$$\sigma^2_{t^{int}} = \sum_{i=1}^{2} \sigma^2_{t_i^{tdc}} + \left(\frac{t^{tof} m_e^2}{E_i(E_i + m_e)(E_i + 2m_e)}\right)^2 \sigma^2_{E_i} + \left(\frac{1}{\beta_i}\right)^2 \sigma^2_{l_i}\,. \tag{6.4.6}$$

When calculating the internal hypothesis for $e\gamma$ events, a similar set of equations are used but differing in that $\beta \to c$ in Eq. 6.4.1 for the γ-ray, where c is the speed of light.

The probability that the event had internal origins $P(\chi^2_{int})$ is defined

$$P(\chi^2_{int}) = 1 - \frac{2}{\pi}\int_0^{\chi^2} e^{x^2} dx\,, \tag{6.4.7}$$

where

$$x = \frac{1}{1+\sqrt{2\chi^2_{int}}}\,. \tag{6.4.8}$$

6.4.2 The crossing electron external vertex hypothesis

The curvature identification via the magnetic field suppresses low energy crossing electrons, but electrons within the $0\nu\beta\beta$ energy window require more sophisticated techniques. The triggered TDC timing information t_i^{tdc} from the two PMTs ($i = 1, 2$) is used to compute the probability of the event origin being outside the source foil. Assuming only one ionizing particle crosses the two halves of the sector split by the source foil, it is characterized by track lengths l_i and the energy deposited in the calorimeter E_i. The particle's time-of-flight (t^{tof}) is defined in natural units as

$$t^{tof} = \frac{l_1}{\beta_1} + \frac{l_2}{\beta_2}\,, \tag{6.4.9}$$

where β_i has the same form as in Eq. 6.4.2, but β_2 differs from β_1 as it takes into account energy loss through the gas of the tracking chamber and source foil. Consequently the χ^2_{ext} variable is written

$$\chi^2_{ext} = \frac{\left(\left(t_2^{tdc} - t_1^{tdc}\right) - t^{tof}\right)^2}{\sigma^2_{t^{ext}}}\,, \tag{6.4.10}$$

where $\sigma^2_{t^{ext}}$ is explicitly written as

$$\sigma^2_{t^{ext}} = \sum_{i=1}^{2} \sigma^2_{t_i^{tdc}} + \left(\frac{t^{tof} m_e^2}{E_i(E_i+m_e)(E_i+2m_e)}\right)^2 \sigma^2_{E_i} + \left(\frac{1}{\beta_i}\right)^2 \sigma^2_{l_i}\,. \tag{6.4.11}$$

When calculating the external hypothesis for $e\gamma$ events, a similar set of equations are used but differing in that $\beta \to c$ in Eq. 6.4.9 for the γ-ray, where c is the speed of light. The probability that the event had external origins $P(\chi^2_{ext})$ is defined in the same way as Eq. 6.4.7.

6.4.3 Fitting Monte Carlo to data

Single and multi-channel least-χ^2 fits serve a general purpose, but a maximized binned log-likelihood function will take advantage of the energy distribution shape.

Assume that the MC predicts the number of events in the i^{th} bin of the histogram to be the sum of the signal (s_i) and background (b_i). Poisson statistics apply to each bin so the probability (p_i) of observing d_i events is

$$p_i = \frac{e^{-(s_i+b_i)}(s_i+b_i)^{d_i}}{d_i!}\,. \tag{6.4.12}$$

The likelihood (L) is defined as the product of binned probabilities

$$L = \prod_{i=0}^{N} p_i\,, \tag{6.4.13}$$

$$= \prod_{i=0}^{N} \frac{e^{-(s_i+b_i)}(s_i+b_i)^{d_i}}{d_i!}\,, \tag{6.4.14}$$

where N is the total number of bins in the histogram. The maximum of L is unaffected by monotone transformations, therefore one can take the logarithm of the function

$$\ln(L) = \sum_{i=0}^{N} \left(-(s_i+b_i) + d_i \ln(s_i+b_i) - \ln(d_i!)\right)\,, \tag{6.4.15}$$

and the first derivative with respect to the total signal S to find the maximum

$$\frac{\partial \ln(L)}{\partial S} = -1 + \sum_{i=0}^{N} \left(\frac{d_i}{s_i+b_i}\,\frac{\partial s_i}{\partial S}\right) = 0\,. \tag{6.4.16}$$

Eq. 6.4.16 is solved numerically for S to find the number of events. L follows the χ^2 distribution, therefore the one σ error on S is determined by the interval where $\ln(L)$ decreases by 1/2 its maximum value

$$\ln(L(S)) - \ln(L(S \pm \Delta S)) = \frac{1}{2}\,. \tag{6.4.17}$$

Eq. 6.4.17 is solved numerically for ΔS to find the error.

6.4.4 Determining the half-life of a decay

The half-life of the isotope under study is derived from the radioactive decay law

$$N = N_0 e^{-\lambda t}\,, \tag{6.4.18}$$

where N is the number of remaining atoms, N_0 is the number of atoms at the beginning of the experiment, $\lambda = \frac{1}{\tau} = \frac{\ln(2)}{T_{1/2}}$, and t is the experimental run time. The number of observed decays N_{obs} equals the number of atoms at the beginning minus the number of remaining atoms

$$N_{obs} = N_0 - N\,, \tag{6.4.19}$$

which gives

$$N_{obs} = N_0(1 - e^{-\lambda t}) \,. \tag{6.4.20}$$

The half-life of the isotope will be large, therefore we can apply a Taylor expansion to the exponential of Eq. 6.4.20 giving

$$N_{obs} = N_0 \lambda t = N_0 \frac{\ln(2)}{T_{1/2}} t \,, \tag{6.4.21}$$

and solve for $T_{1/2}$

$$T_{1/2} = \frac{N_0}{N_{obs}} \ln(2) t \,. \tag{6.4.22}$$

The number of atoms at the beginning of the experiment is expressed

$$N_0 = N_A \frac{m}{Z} \,, \tag{6.4.23}$$

where N_A is Avogadro's number, m is the isotopic mass, and Z is the atomic number of the isotope, therefore transforming Eq. 6.4.22 into

$$T_{1/2} = \frac{m}{Z} \frac{N_A}{N_{obs}} \ln(2) t \,. \tag{6.4.24}$$

The detector efficiency ε is not perfect therefore N_{obs} must be corrected

$$N_{obs} \to \frac{N_{obs}}{\varepsilon} \,, \tag{6.4.25}$$

which finally gives

$$T_{1/2} = \varepsilon \frac{m}{Z} \frac{N_A}{N_{obs}} \ln(2) t \,. \tag{6.4.26}$$

6.4.5 Limit setting and confidence levels

In the scenario where the statistical significance of a signal is too low for claiming a measurement, the signal is excluded at a determined confidence level (CL). Using data, background, and signal distributions and applying a similar procedure as Sec. 6.4.3, the limit on the signal can be improved relative to simple counting methods [96, 97].

The typical method for searches with small statistics is the log-likelihood ratio (LLR) test statistic [98, 99]. The signal-plus-background ($S + B$) hypothesis and the background-only hypothesis (B-only) are defined. The aim is to quantify the consistency between data and the two hypotheses and is written as the ratio between the

Poisson likelihood L of the $S+B$ hypothesis (as seen in Eq. 6.4.14) and B-only hypotheses

$$Q = \frac{L(S+B)}{L(B)}\,, \tag{6.4.27}$$

$$= \prod_{i=0}^{N} \frac{e^{-(s_i+b_i)}(s_i+b_i)^{x_i}/x_i!}{e^{-b_i}b_i^{x_i}/x_i!}\,, \tag{6.4.28}$$

$$= \prod_{i=0}^{N} e^{-s_i}\left(\frac{s_i+b_i}{b_i}\right)^{x_i}\,, \tag{6.4.29}$$

where i is the i^{th} bin of the distribution, s_i is the number of expected signal events in that bin, b_i is the predicted number of background events. Pseudo-data x_i is obtained randomly via the Poisson distribution given an expectation of $s_i + b_i$ events. The test statistic in Eq. 6.4.29 is recast as a negative log-likelihood ratio (NLLR) and defined

$$\chi = \mathrm{NLLR} = -2\ln(Q)\,, \tag{6.4.30}$$

$$= 2\sum_{i=0}^{N}\left(s_i - x_i\ln(1+\frac{s_i}{b_i})\right)\,. \tag{6.4.31}$$

The NLLR of the observed data (χ_d) is found by substituting the generated x_i with the real value d_i. One can calculate a confidence level (CL) corresponding to the outcomes which give a result appearing less like the $S+B$ hypothesis than the observed data. The confidence level in the $S+B$ hypothesis (CL_{S+B}) is given by

$$CL_{S+B} = P_{S+B}(\chi > \chi_d) = \int_{\chi_d}^{\infty} \frac{\partial P_{S+B}}{\partial \chi} d\chi\,, \tag{6.4.32}$$

and a similar nomenclature determines the confidence level in the B-only hypothesis (CL_B)

$$CL_B = P_B(\chi > \chi_d) = \int_{\chi_d}^{\infty} \frac{\partial P_B}{\partial \chi} d\chi\,. \tag{6.4.33}$$

Fig. 6.4 from Ref. [98] demonstrates the NLLR distributions for the $S+B$ hypothesis and B-only hypothesis compared to observed data. The confidence level in the signal CL_S is defined as

$$CL_S = \frac{CL_{S+B}}{CL_B}\,, \tag{6.4.34}$$

and the limit is found by scaling the signal until $1 - CL_S = 0.9$ or the 90% confidence level.

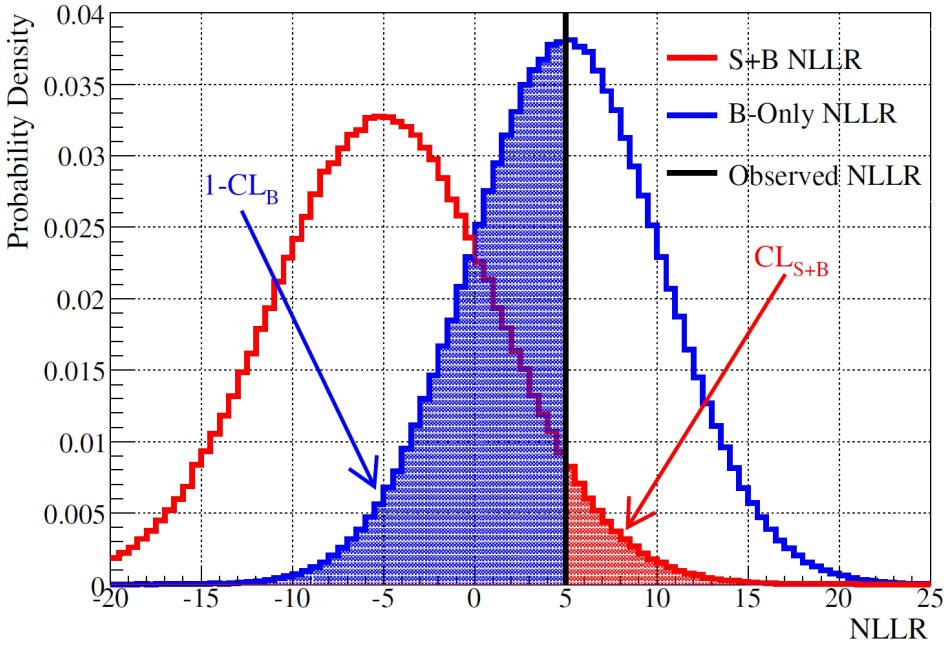

Figure 6.4: Example distributions from Ref. [98] of the NLLR test statistic evaluated for the $S+B$ hypothesis (red) and B-only hypothesis (blue) compared to observed data (black).

Chapter 7

Background estimation for the 96-Zr source

$2\nu\beta\beta$ decay experiments generally measure or reconstruct the energy sum of the two emitted electrons using methods described in Chap. 4. The backgrounds are therefore anything which mimics a two electron type event. The "smoking gun" signal of a $0\nu\beta\beta$ decay is the energy sum of the two emitted electrons equaling that of the $Q_{\beta\beta}$ of the decay. In this scenario the backgrounds must mimic a two electron type event and also have a high summed energy in the $Q_{\beta\beta}$ region of interest. The sensitivity of the experiment is dependent on the number of background events found in the $Q_{\beta\beta}$ energy region.

To determine if the experimental data contains signal events, it is necessary to suppress and subtract any backgrounds that are present after the event selection process. The small amounts of natural radioactivity found in raw materials are magnitudes above the level required to reach the NEMO-3 sensitivity. The majority of harmful background isotopes are daughters of the natural decay chains $^{238}\mathrm{U}$ and $^{232}\mathrm{Th}$ as displayed in Fig. 7.1. Small amounts of these isotopes are in the materials that make up the NEMO-3 detector, therefore all materials used in the construction of the detector were selected on a basis of their radioactive purity (measured with HPGe detector) and where permissible, new manufacturing processes were developed for the production of highly radiopure materials. The backgrounds to $0\nu\beta\beta$ decay include the irreducible $2\nu\beta\beta$ decay (to be discussed in Sec. 8) and radioactive decay which can mimic $\beta\beta$-type events. A unique feature of NEMO-3 is 2-electron events are the only background. Cosmic muons are a negligible background to NEMO-3 due to the very small flux (Sec. 5.7.2).

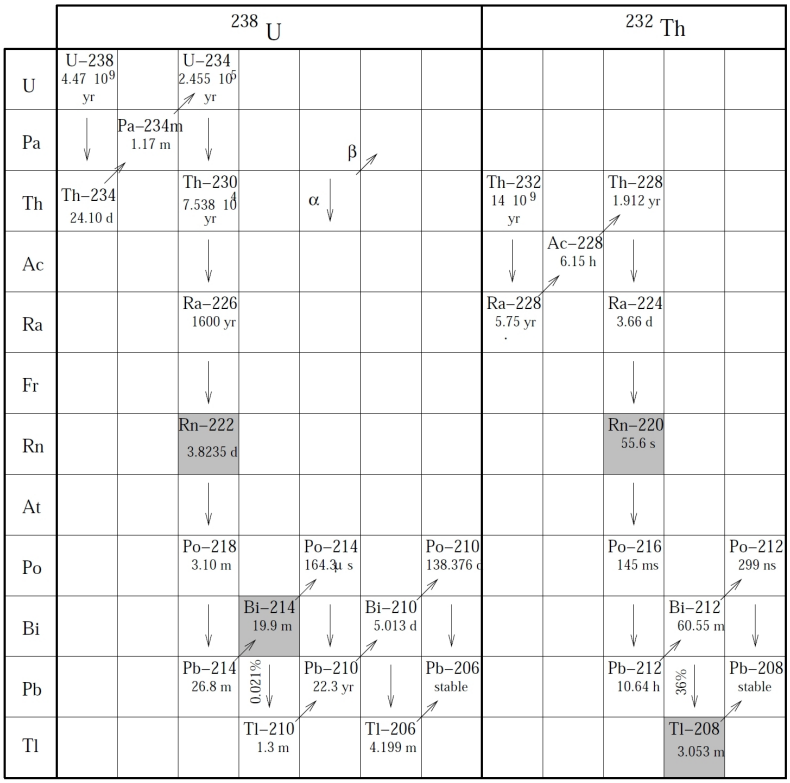

Figure 7.1: Natural decay chains of ^{238}U, and ^{232}Th.

7.1 Natural radioactivity

Isotopes with high Q_β values and strong gamma transitions at high energies that overlap the signal region are the most harmful backgrounds to $0\nu\beta\beta$ searches. The main candidates for being troublesome backgrounds are ^{214}Bi and ^{208}Tl. ^{214}Bi is a daughter of the ^{238}U decay chain, has a Q_β value of 3.27 MeV and a half-life of 19.9 min. The ^{214}Bi decay scheme Fig. 7.2 includes a 1.76 MeV gamma transition with 15.8% intensity and a 1.12 MeV gamma transition with 15.0% intensity. ^{208}Tl is a daughter of the ^{232}Th decay chain, has a Q_β value of 4.99 MeV and a half-life of 3.05 min. The ^{208}Tl decay scheme Fig. 7.3 includes a 2.62 MeV gamma transition with $\sim$100% intensity. The strict radiopurity selection process for detector materials suppresses the amount of ^{214}Bi and ^{208}Tl within the detector, but the isotopes of ^{222}Rn and ^{220}Rn from the surrounding rock enter the detector through diffusion and continue through their decay chains to produce ^{214}Bi and ^{208}Tl daughters. ^{220}Rn has a half-life of 55.6 s and does not pose as much a problem as ^{222}Rn which has a half-life of 3.82 days, giving it enough time to escape the rock and diffusely enter the detector volume. The radon trapping facility mentioned in Sec. 5.5 was commissioned to purify

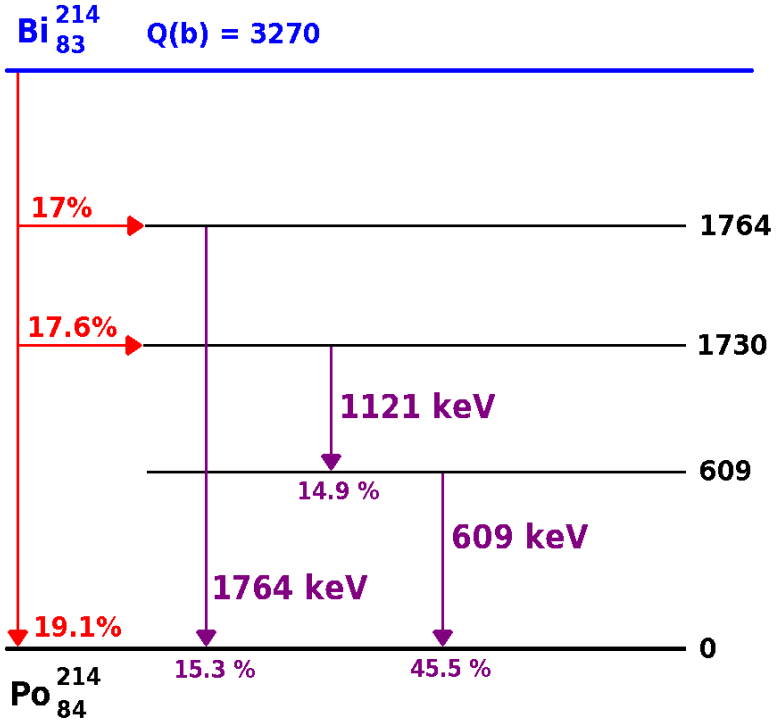

Figure 7.2: The simplified decay scheme of ^{214}Bi highlighting the harmful gamma transitions.

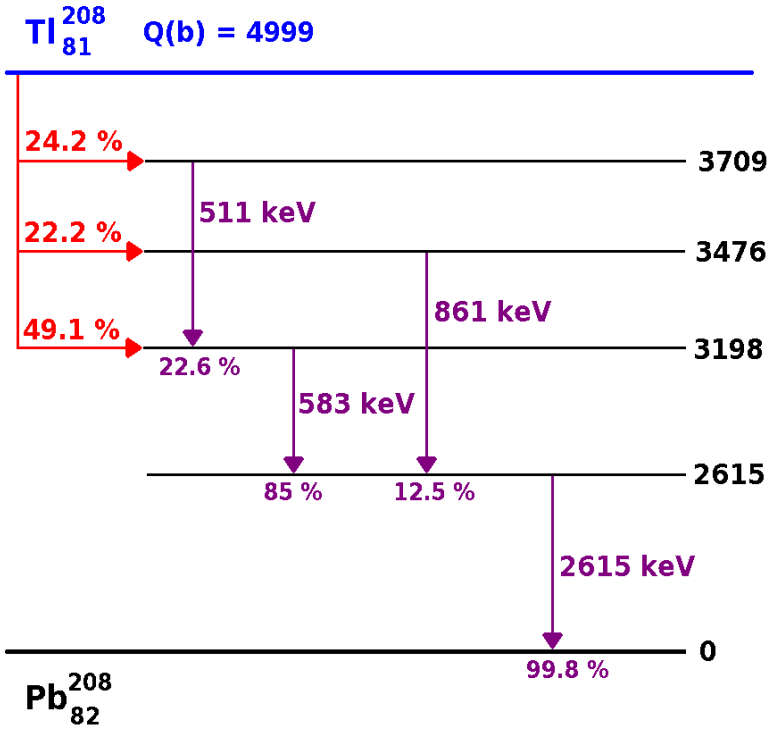

Figure 7.3: The highly simplified decay scheme of ^{208}Tl highlighting the harmful gamma transitions.

the air of radon and inject the pure air around the detector to suppress further radon diffusion.

7.1.1 Decay Schemes

The simplified decay schemes illustrated in Fig. 7.2 and Fig. 7.3 (and later in Fig. 11.1) are interpreted as follows. The parent nuclei is labeled at the top in BLUE. It decays and leaves the daughter nuclei (at the bottom in BLACK) in an excited state with energy (in keV) as labeled on the right side (in BLACK) and with a branching ratio as indicated on the left side (in RED). The strong gamma transitions from the excited state to ground state are indicated in PURPLE with their relative intensities also labeled in PURPLE.

7.2 Radon suppression

Radon diffusely permeates many materials and acts as a transport for its troublesome daughter isotope $^{214}\mathrm{Bi}$. $^{214}\mathrm{Bi}$ is suppressed by radon purification of the air around the detector as described in Sec. 5.5 and tagged as a so called Bi-Po event as mentioned in Sec. 5.6.2. As was shown in Fig. 7.1, $^{222}\mathrm{Rn}$ decays to $^{214}\mathrm{Bi}$ via two alpha decays and a beta decay. $^{214}\mathrm{Po}$ is the alpha emitting daughter isotope of $^{214}\mathrm{Bi}$ and has a half-life of 164.3 μs. The global trigger (tracking and calorimeter) time window remains open for 710 μs. It is therefore possible to tag $^{214}\mathrm{Bi}$ events by their delayed α-decays from the Bi-Po process (Fig. 7.4) to either measure the radon background or exclude them from the ee analysis.

The first data acquisition period (Feb 2003 – Oct 2004) is referred to as phase-1 and had a relatively high (1.2 Bq) level of radon in the tracking volume. Supporting evidence suggests [100] that a large fraction (87%) of α-decay daughters are positively charged and are attracted to electrically negative and grounded surfaces. NEMO-3 data are consistent with the radon daughters being deposited on the surfaces of the reflective wrapping around the scintillators, the drift cell cathode wires and the source foils [93].

The second data acquisition period (Nov 2004 – Dec 2007) is referred to as phase-2 and began after the installation of a radon purification facility (Sec. 5.5) to inject a flow of pure air around the detector. The purification facility suppresses the radon concentration in the immediate proximity of the detector by a factor of ~ 1000. However,

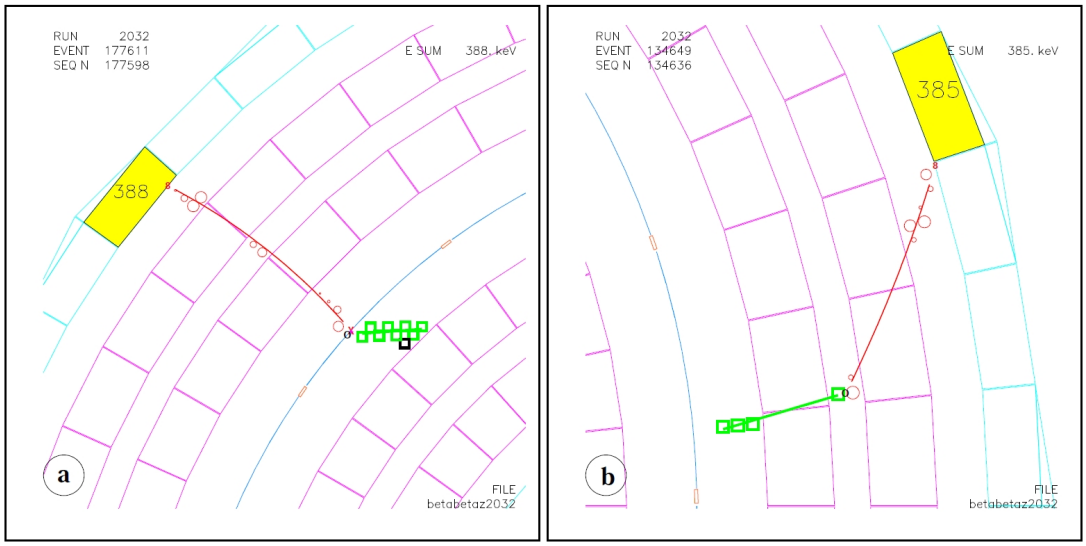

Figure 7.4: Examples of candidate Bi-Po events viewed from the top. For each event the triggering track is red (electron) and the delayed track is green (α-particle). The two tracks have a common vertex: on the source foil (a) and inside the tracking volume (b).

the out-gassing of detector components releasing radon due to their internal contamination with the $^{238}\mathrm{U}-^{226}\mathrm{Ra}$ chain leads to a smaller reduction factor inside the detector. The radon activity in the tracker volume decreased from 1.2 Bq in phase-1 to 0.2 Bq in phase-2 (Fig. 7.5).

7.3 External backgrounds

External backgrounds include all decays originating from outside the source foil but interacting with the source foil to mimic a $\beta\beta$-type event. The most harmful isotopes are those with strong gamma transitions and three dominant, contributing processes include pair production, double Compton scattering, and Compton plus Møller scattering and are graphically displayed in Fig. 7.6. Pair production occurs when a γ-ray interacts with the source foil to create an electron and positron to mimic a $\beta\beta$-type event. The 25 Gauss magnetic field provides 97% efficient electron-positron identification at 1 MeV and suppresses these events. One focus of the NEMO-3 research and development (R&D) was minimizing $^{214}\mathrm{Bi}$ and $^{208}\mathrm{Tl}$ contaminants in the detector materials. Component measurements done with a high purity germanium detector (HPGe) are tabulated in Tab. 7.1.

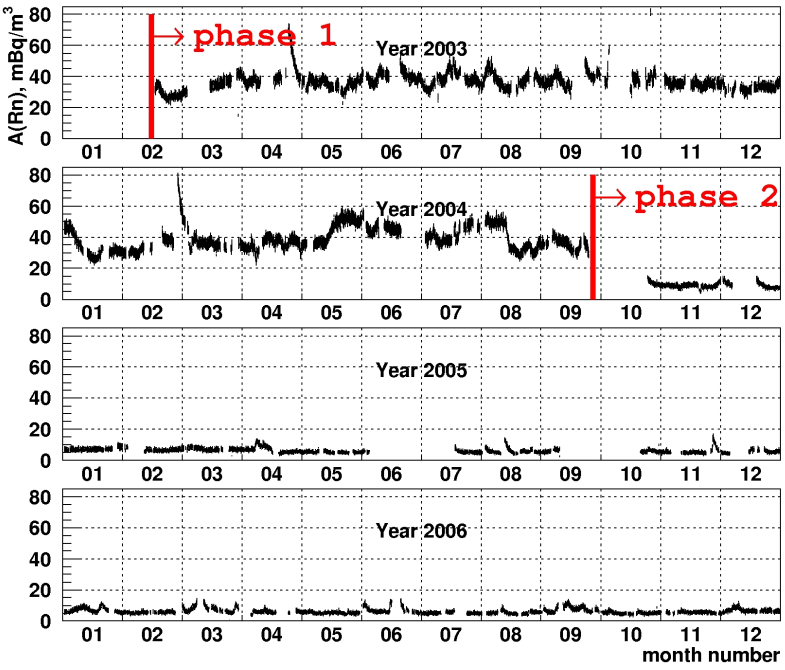

Figure 7.5: The ^{222}Rn activity (mBq/m^3) inside the tracking chamber measured on an hourly basis for phase-1 and phase-2 data periods.

Table 7.1: Activities of the main detector components, measured with a HPGe detector and extrapolated to the total mass of the component.

		Activity (Bq)	
Detector Component	mass (kg)	^{214}Bi	^{208}Tl
Iron shield	180000	< 300	< 300
Steel frame	10000	< 6	< 8
Copper frame	25000	< 25	< 10
PM μ-metal	2000	< 2	< 2.7
PMTs	600	302	17.8
Scintillator	5000	< 0.7	< 0.3
Tracker wires	1.7	$< 10^{-3}$	$< 6 \times 10^{-4}$

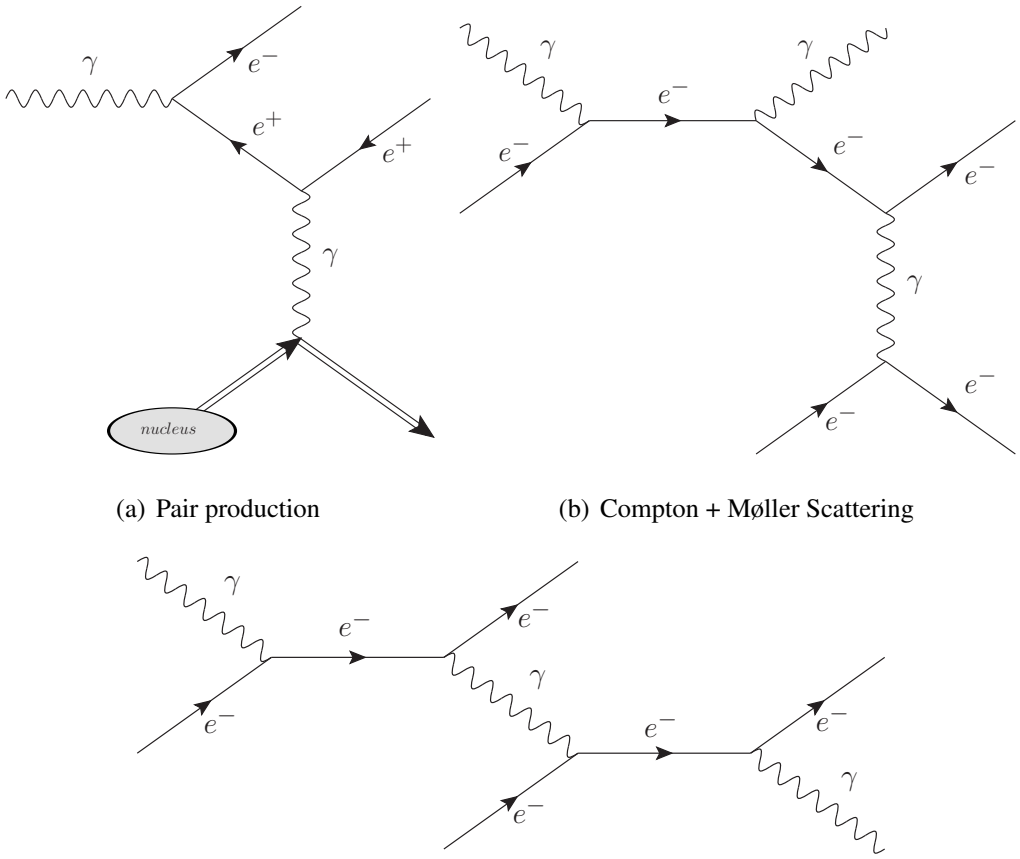

(a) Pair production

(b) Compton + Møller Scattering

(c) Double Compton Scattering

Figure 7.6: Three dominant processes through which external backgrounds mimic ee events.

7.3.1 The external background model

The external backgrounds to NEMO-3 consists of any process which produces γ-rays. The γ-ray flux is due to radioactive decay from within the surrounding rock of the LSM laboratory, neutron capture, and radioactive decay from within the NEMO-3 detector itself. As shown in [93], the γ-ray flux from the surrounding rock and neutron capture is negligible compared to detector component sources. The flux is best described by defining the support structure, PMTs, scintillators, and tracking chamber wires as the sources of radioactivity. To obtain a model of the external background, the NEMO-3 detector itself was used to measure the activities of the above stated sources of radioactivity. The external background model has been validated in the $1e$ and $e\gamma$ channels using the dedicated sectors of ultra-pure copper (OFHC – oxygen-free high conductivity) and is summarized in Tab. 7.2. A detailed discussion of the NEMO-3

Table 7.2: Summary of the external background model defined by origin and decay activity. The model has been validated in the $1e$ and $e\gamma$ channels using the dedicated sectors of ultra-pure copper.

	Activity (Bq)						
Component	^{40}K	^{214}Bi	^{214}Pb	^{208}Tl	^{228}Ac	^{60}Co	^{210}Bi
Iron shield		7360		484	1350		
Steel frame	100	9.12		3.07	8.54	6.09	
Copper frame						66.0	
PM μ-metal						14.6	
PMTs	1080	324		27.0	72.7		
Scintillators	21.5	0.38	0.38				30.4
Tracker wires		0.198	0.198				12.6

backgrounds can be found in [93]. The expected number of events from the external background in the ee channel is shown in Tab. 8.3.

7.4 Internal backgrounds

Due to topological event discrimination (Sec. 6.2.1), only two electron events are a background to the $2\nu\beta\beta$ and $0\nu\beta\beta$ studies. Internal backgrounds are defined as isotopes decaying from within the source foil itself. Harmful isotopes are the β emitters because they mimic $\beta\beta$-type events via β-decay with Møller scattering, β-decay with internal conversion, or β-decay with Compton scattering of the de-excitation photon. These processes are displayed in Fig. 7.7.

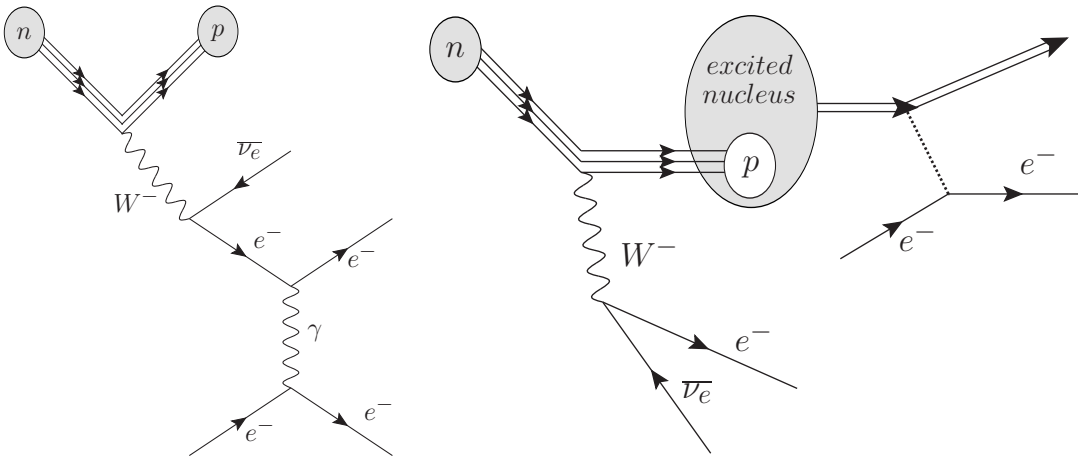

(a) Beta decay + Møller Scattering

(b) Beta decay + Internal Conversion

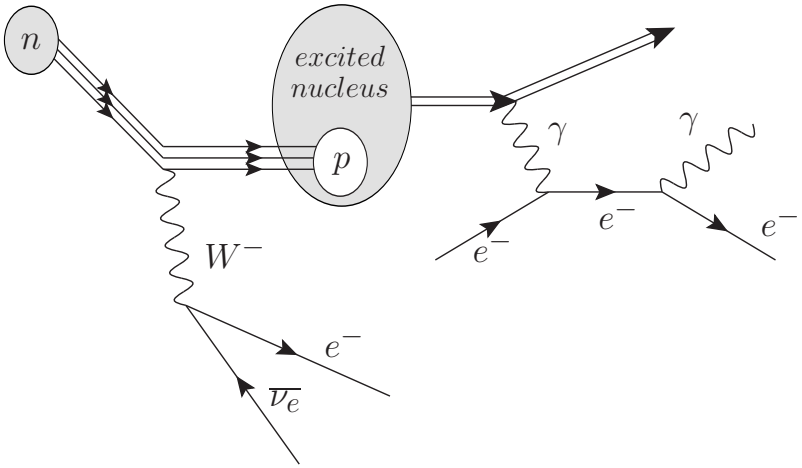

(c) Beta decay + Compton Scattering

Figure 7.7: Three dominant processes through which internal backgrounds mimic ee events.

7.4.1 Estimation of the internal backgrounds

Limits have been placed on the internal background activities of $^{96}\mathrm{Zr}$ by a high purity germanium (HPGe) detector, but ultimately the internal background activities are measured with the NEMO-3 apparatus. Internal background activities are measured in the $1e$ and $e\gamma$ channels. The $1e$ selection criteria are the following:

- One track is required with curvature consistent with a negative particle.
- One scintillator must have an energy deposit $> 500\,\mathrm{keV}$ to suppress copious low energy events.
- The track is required to originate on the $^{96}\mathrm{Zr}$ source foil and whose endpoint is associated with the registered scintillator.
- The track must have a hit in one of the first two layers of the Geiger cells to maximize the vertex resolution.
- There must be no Geiger cell hits opposite the side of the source foil with the reconstructed track within 15 cm of the event vertex to suppress γ's originating from the wires which interact with the source foil to mimic an internal background.
- Requiring a track length $> 50\,\mathrm{cm}$ maximizes track reconstruction efficiency and vertex resolution.

The $e\gamma$ selection criteria are the following:

- One track is required with curvature consistent with a negative particle.
- Two scintillators must each have energy deposits $> 200\,\mathrm{keV}$ to suppress copious low energy events.
- The track is required to originate on the $^{96}\mathrm{Zr}$ source foil and whose endpoint is associated with one of the registered scintillators.
- The track must have a hit in one of the first two layers of the Geiger cells to maximize the vertex resolution.

- There must be no Geiger cell hits opposite the side of the source foil with the reconstructed track within 15 cm of the event vertex to suppress γ 's originating from the wires which interact with the source foil to mimic an internal background.

- Requiring a track length > 50 cm maximizes track reconstruction efficiency and vertex resolution.

- Selecting events whose $\cos\theta$ between the track and presumed γ-ray path < 0.9 suppresses a fraction of the events from the dominant $^{40}\mathrm{K}$ internal background, thereby increasing the sensitivity to other backgrounds.

- The internal hypothesis (Sec. 6.4.1) probability is required to be $> 4\%$ and the external hypothesis (Sec. 6.4.2) probability is required to be $< 1\%$.

Studies have provided signal-to-background optimized $P(\chi^2_{int})$ and $P(\chi^2_{ext})$ values [101] as criteria for selecting internal events

$$P(\chi^2_{int}) > 0.04 \quad \text{and} \quad P(\chi^2_{ext}) < 0.01\,. \tag{7.4.1}$$

The internal background activities are distinguished and measured due to contrasting Q_β values and $1e$ and $e\gamma$ energy spectra shape. Certain isotopes are assumed to be in equilibrium because of their short half-lives. Chemical processing of a material can cause disequilibrium, but the isotopes with short half-lives soon regain equilibrium. $^{228}\mathrm{Ac}$, $^{212}\mathrm{Bi}$, and $^{208}\mathrm{Tl}$ are part of the $^{232}\mathrm{Th}$ chain and separated by short half-lives, therefore $^{228}\mathrm{Ac}$ and $^{212}\mathrm{Bi}$ activities are set equal and the $^{208}\mathrm{Tl}$ activity is set to its branching fraction of 36%.

$^{214}\mathrm{Bi}$ and $^{214}\mathrm{Pb}$ belong to the $^{238}\mathrm{U}$ chain and are set equal. $^{234m}\mathrm{Pa}$ is also part of the $^{238}\mathrm{U}$ decay chain but equilibrium with $^{214}\mathrm{Bi}$ cannot be assumed due to the large half-life of the intermediate isotope $^{226}\mathrm{Ra}$.

Internal $^{40}\mathrm{K}$ contamination was identified by the HPGe detected and is considered within the internal background model. An iterative fitting process to the $1e$ and $e\gamma$ energy distributions is made utilizing the least-χ^2 method. The activities of the isotopes being measured are left as free parameters of the fit. Fig. 7.8 shows the internal backgrounds of the $1e$ channel. Within the $1e$ channel, energies below 1.3 MeV

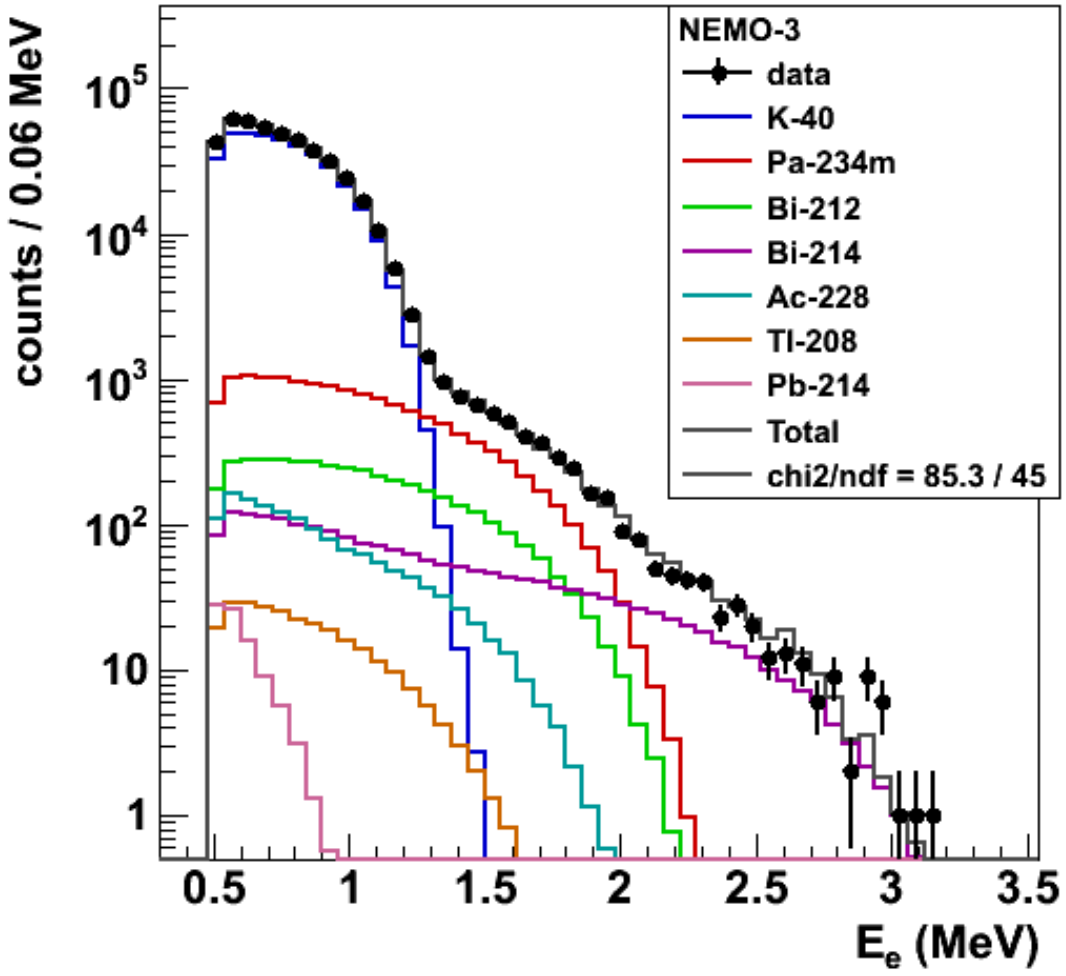

Figure 7.8: Energy spectrum of ^{96}Zr internal backgrounds in the $1e$ channel. External backgrounds are included in the total MC distribution but not displayed in order to highlight the internal background contribution.

are dominated by ^{40}K decays, energies between 1.3-2 MeV mainly consist of ^{234m}Pa, ^{212}Bi, and only ^{214}Bi has a significant contribution above 2.3 MeV. Fig. 7.9 shows the same $1e$ channel data with the internal and external backgrounds separately summed. The high Q_β and high energy gamma transitions of ^{214}Bi and ^{208}Tl are more evi-

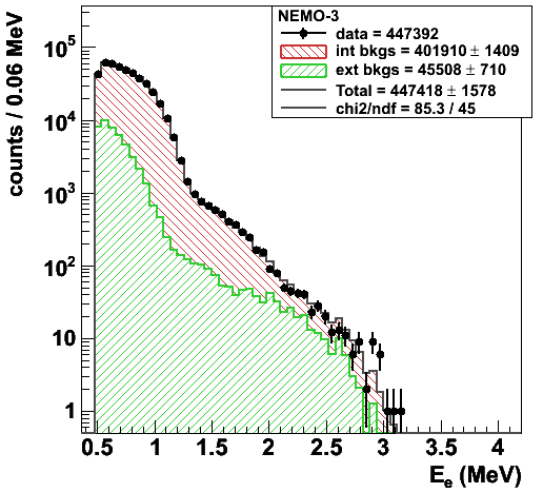

Figure 7.9: Energy spectrum of ^{96}Zr backgrounds in the $1e$ channel. The background contributions are divided into 2 sub-groups of summed internal (int) and external (ext) components.

dent in the $e\gamma$ channel as displayed in Fig. 7.10. Within the $e\gamma$ channel, energies below 1.5 MeV are dominated by ^{228}Ac decays, energies between 1.5-2.5 MeV mainly consist of ^{214}Bi, and only ^{208}Tl has a significant contribution above 2.8 MeV. Fig. 7.11 shows the summed and individual energy distributions of electrons and gammas as well as the angular distribution between them.

The measurements of the ^{96}Zr internal contamination obtained in the $1e$ and $e\gamma$ channels compared with previously obtained HPGe limits in Tab. 7.3 provide a cross-check for the NEMO-3 measurements. The obtained numbers are in agreement with the ^{214}Bi and ^{208}Tl activities (0.17 ± 0.05 mBq and 0.08 ± 0.01 mBq respectively) reported in Ref. [93] where different event topologies were used to identify signatures of the isotopes. Discrepancy between the data and MC reflects the imperfect modeling of the NEMO-3 detector in GEANT-3.21 and inaccuracy of the internal background model.

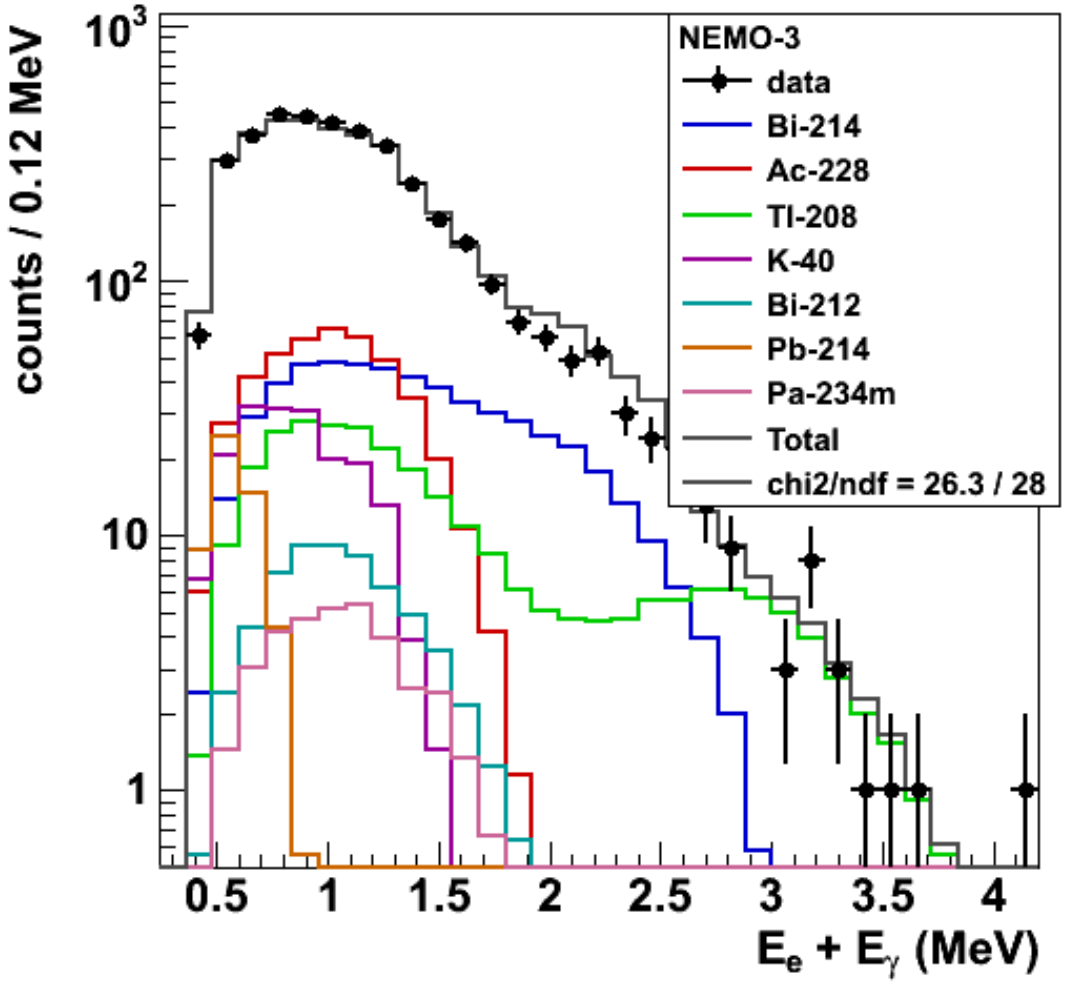

Figure 7.10: Energy spectrum of ^{96}Zr internal backgrounds in the $e\gamma$ channel. External backgrounds are included in the total MC distribution but not displayed in order to highlight the internal background contribution.

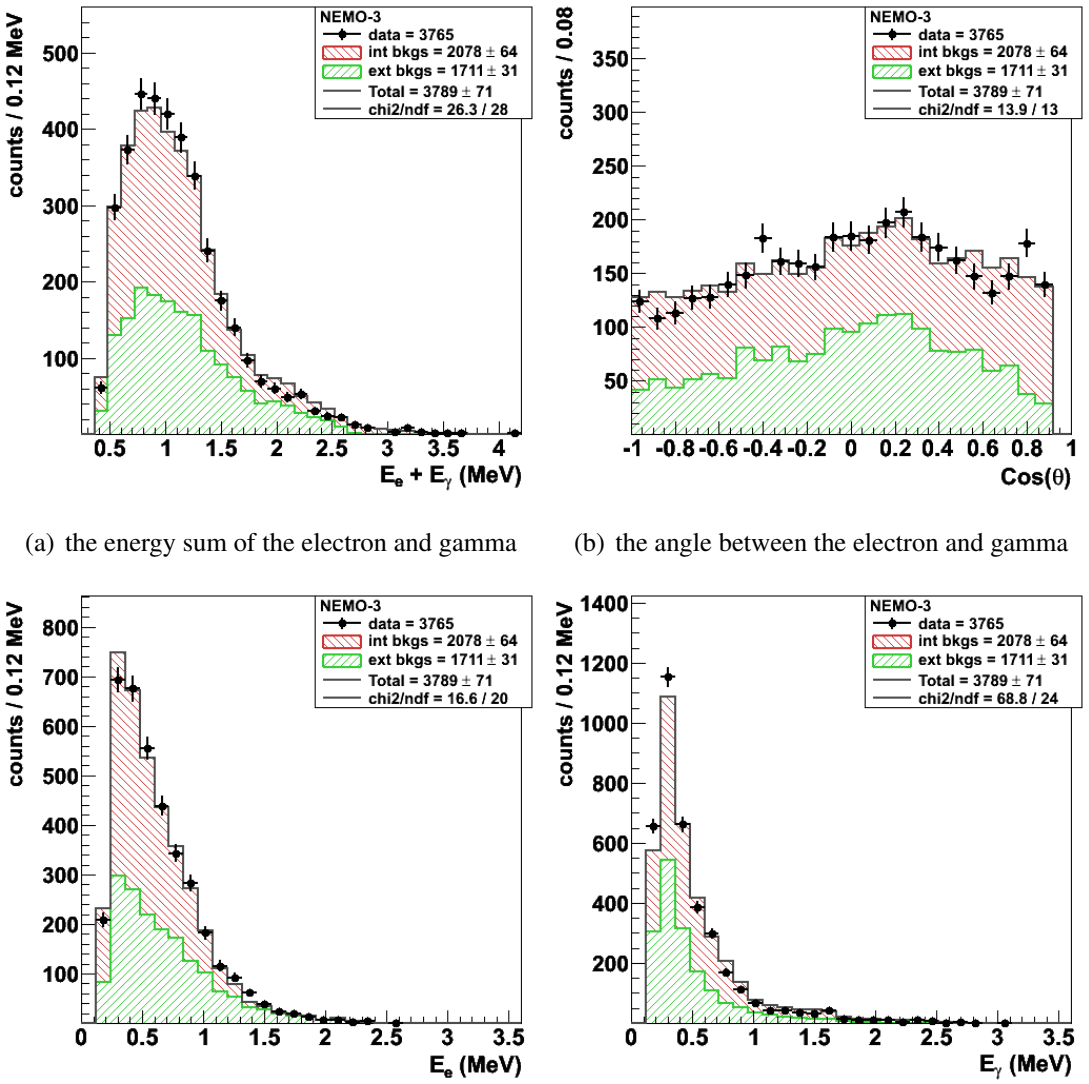

(a) the energy sum of the electron and gamma

(b) the angle between the electron and gamma

(c) the energy of the electron

(d) the energy of the gamma

Figure 7.11: The $e\gamma$ channel displaying (a) the summed energy $E_e + E_\gamma$, (b) the angular distribution between the electron and gamma $\cos(\theta)$, (c) the energy of the electron E_e, and (d) the energy of the gamma-ray E_γ. The background contributions are divided into 2 sub-groups of summed internal (int) and external (ext) components.

Table 7.3: Internal contamination of the ^{96}Zr source foil measured with NEMO-3 in the $1e$ and $e\gamma$ channels under the assumptions of the background model described in Sec. 7.4.1. The NEMO-3 measurements are compared to HPGe limits at 95% confidence level.

Isotope	NEMO-3 (mBq)	HPGe (mBq)
^{228}Ac	0.25 ± 0.02	< 0.75
^{212}Bi	0.25 ± 0.02	< 0.75
^{208}Tl	0.091 ± 0.007	< 0.23
^{214}Bi	0.19 ± 0.02	< 0.45
^{214}Pb	0.19 ± 0.02	< 0.45
^{40}K	19.7 ± 0.1	< 19
^{234m}Pa	0.49 ± 0.01	< 6.6

7.4.2 ^{150}Nd and ^{48}Ca internal backgrounds

The adjacent $\beta\beta$ source isotopes of ^{150}Nd and ^{48}Ca and their associated internal backgrounds [36, 53, 102] contribute events that pass the ^{96}Zr selection criteria due to the positional resolution of the Geiger cell tracker and accuracy of the reconstructed event vertex. These events have been studied and contribute $\sim 1\%$ in the $1e$ channel as seen in Fig. 7.12(a) and contribute $\sim 7\%$ in the $e\gamma$ channel as seen in Fig. 7.12(b). They are included in the background description for ^{96}Zr.

7.4.3 Confidence in the background description

Confidence that the backgrounds are being accurately described by the MC is gained through observing consistency among different channels ($1e$, $e\gamma$, ee), time periods (phase-1, phase-2), and locations (Cu, ^{130}Te). A large uncertainty is associated with the description of the low energy background (< 1 Mev) mainly because of the numerous possible low energy radioactive decays and copious X-rays. For simplicity, the background model is constructed to accurately describe the data and reproduce the true physics of the high energy (and dominant) sources of radioactivity. The background description therefore, does not reproduce the true physics of all radioactive decays and this consequence is exaggerated at low energies. Furthermore, photon in-

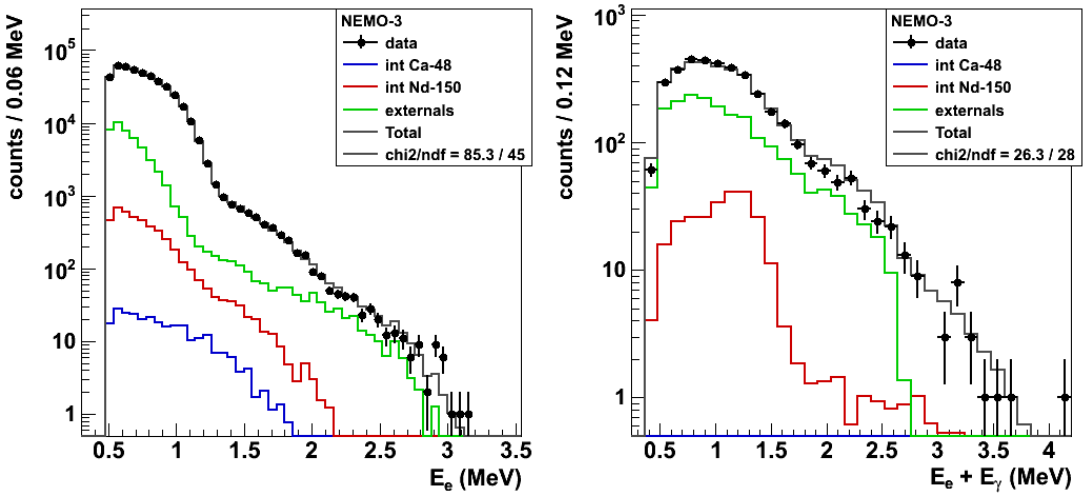

(a) ^{150}Nd and ^{48}Ca events in the $1e$ channel (b) ^{150}Nd and ^{48}Ca events in the $e\gamma$ channel

Figure 7.12: Energy spectra of the $1e$ (a) and $e\gamma$ (b) channels showing the total event contributions from ^{150}Nd and ^{48}Ca internal backgrounds. The sum of external backgrounds is show for comparison.

teractions modeled by GEANT-3.21 become less precise at low energy due to the steep slope of the photo-electric cross section. Fortunately the sensitivity to $0\nu\beta\beta$ decay does not depend on low energy backgrounds but requires an accurate background description in the energy region of interest (> 2 MeV). Accuracy of the background description is observed at high energy in both $1e$ and $e\gamma$ channels (see Fig. 7.13).

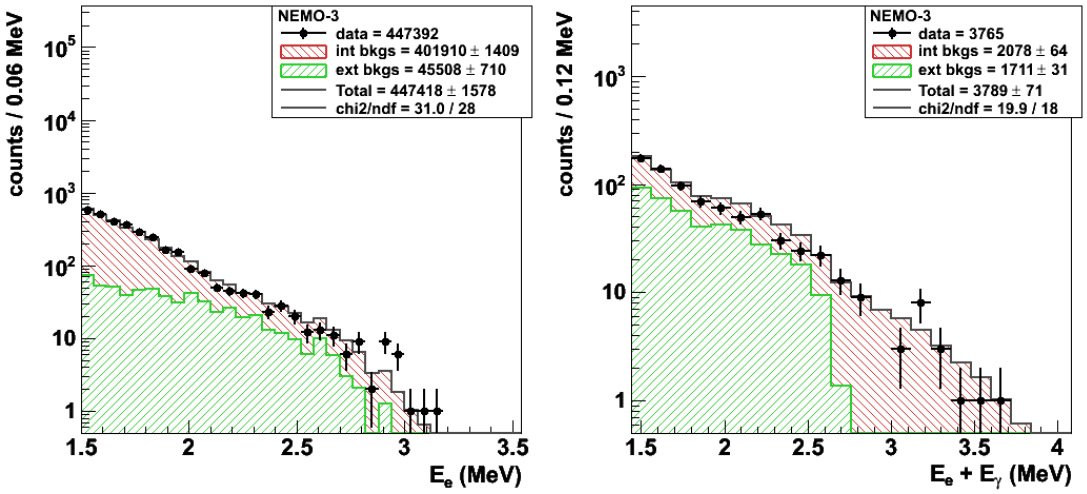

(a) $1e$ channel with $\chi^2 = 31.0/28$ (b) $e\gamma$ channel with $\chi^2 = 19.9/18$

Figure 7.13: The MC describes the data very well at high energy where the $0\nu\beta\beta$ sensitivity depends strongly on an accurate background description.

Chapter 8

^{96}Zr results and discussion

The $2\nu\beta\beta$ analysis follows the same procedure as outlined in Sec. 6. $2\nu\beta\beta$ signal events are generated and propagated through the detector description (Sec. 6.1), reconstructed (Sec. 6.2), and preprocessed (Sec. 6.3). Finally, specific selection criteria (to be described in Sec. 8.1) are defined to maximize the signal-to-background. The signal can be fit to data using the least-χ^2 method, but utilizing the log-likelihood method as described in Sec. 6.4.3 is appropriate for fitting to the shape of the $2\nu\beta\beta$ energy spectrum.

8.1 Selecting two-electron events

The experimental topological signature of $2\nu\beta\beta$ and $0\nu\beta\beta$ events is two electrons with an event vertex at the source foil. The following selection criteria maximize the signal-to-background of two electron events and test the quality of the reconstruction:

- Two tracks are required with curvature consistent with a negative particle.
- Each track must have a length > 30 cm opposed to 50 cm for $1e$ and $e\gamma$ events to increase the signal statistics, but the compromise is the signal to background ratio as indicated in Fig. 8.1.
- Require two scintillators, each with energy deposits > 200 keV to suppresses low energy events. The $2\nu\beta\beta$ signal is weakly affected since the continuous energy spectrum begins ~ 400 keV.
- The two track vertices must be within 2 cm of each other in the XY-plane (Fig. 8.2(a)) and 4 cm in the Z-plane (Fig. 8.2(b)) to maximize the positional reso-

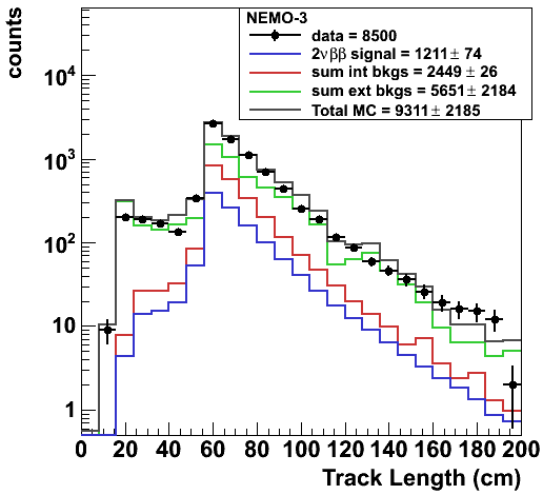

Figure 8.1: Individual track lengths of the two electron topology before applying selection criteria.

lution of the event origin. Backgrounds also display a small ΔR and ΔZ because the particle interactions which mimic a two electron event occur within the thin source foil and therefore do not have a large spatial dispersion.

- Each track must originate from the ^{96}Zr source foil and terminate at an independent scintillator.

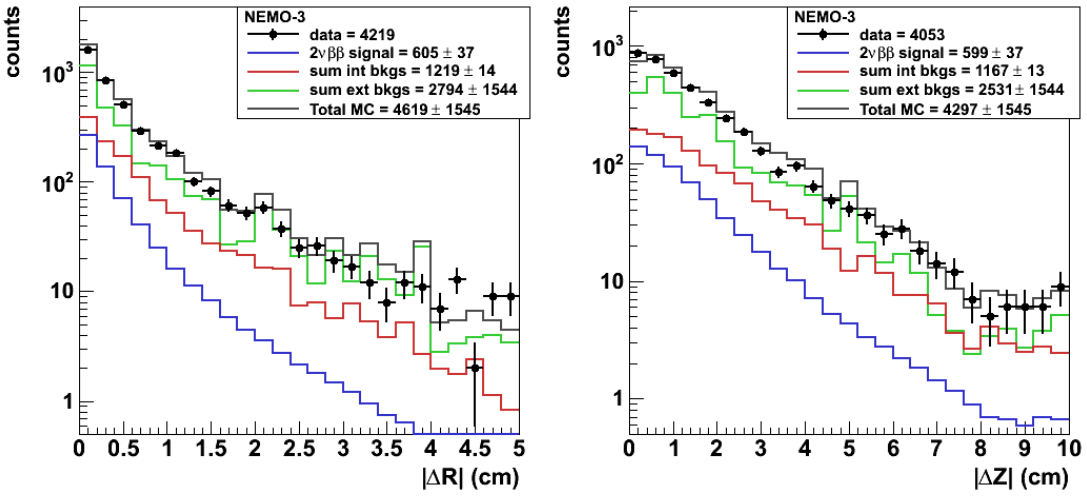

(a) transverse difference of the vertices (b) longitudinal difference of the vertices

Figure 8.2: Difference between vertices in the transverse ($|\Delta R|$) and longitudinal ($|\Delta Z|$) planes before applying selection criteria.

- There must be no Geiger cell hits opposite the side of the source foil with the reconstructed tracks within 15 cm of the event vertex to suppress γ 's originating from the wires which interact with the source foil to mimic a signal event.

- Each track must have a hit in one of the first two layers of the Geiger cells to maximize the vertex resolution.

- The internal hypothesis (Sec. 6.4.1) probability is required to be $> 4\%$. This eliminates a large fraction of the external background events as seen in Fig. 8.3(a).

- The external hypothesis (Sec. 6.4.2) probability is required to be $< 1\%$. This eliminates a large fraction of the external background events as seen in Fig. 8.3(b).

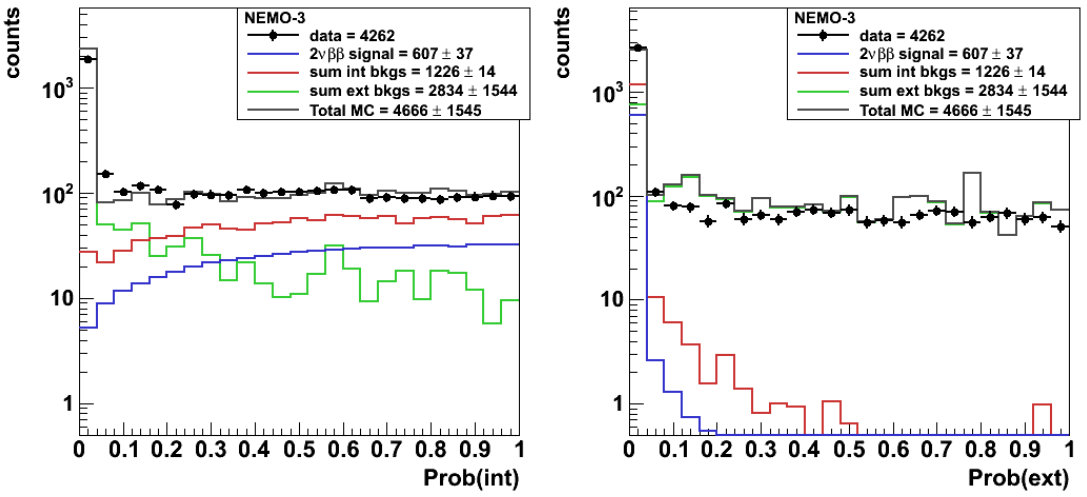

(a) internal hypothesis probability (b) external hypothesis probability

Figure 8.3: Internal and external hypothesis probabilities before applying selection criteria.

The selection criteria are efficient at maximizing the signal to background ratio. This is illustrated by tabulating the acceptance for signal and background (internal ^{40}K for example) events as a function of selection criteria as show in Tab. 8.1. The acceptance is with respect to the number of events which have been reconstructed. The selection criteria make up a fraction of the total efficiency. Other factors include the geometrical acceptance, hardware trigger, detector status, and event reconstruction. The

Table 8.1: Efficiency of the individual selection criteria after reconstruction for signal and background.

	event acceptance (%)	
selection criteria	^{96}Zr	^{40}K
2 electron tracks and 2 scints	39.30	4.62
vertex origin within Zr-96 geometry	56.33	34.42
less than 3 unassociated Geiger hits	98.91	99.39
tracks greater than 30 cm	94.40	94.24
A hit within first two Geiger layers	92.89	49.58
vertex ΔR $<$ 2 cm, ΔZ $<$ 4 cm	58.26	9.59
internal probability $>$ 4%	87.18	71.21
external probability $<$ 1%	66.46	57.13
track endpoint on scintillator face	91.98	94.89
energy deposit $>$ 200 keV	58.68	33.53
passed all the selection criteria	30.16	0.65

geometrical acceptance and hardware trigger are convoluted as one efficiency. The detector status depends on factors such as the efficiency of the radon purification facility, the triggering rate of the Geiger cells, and the PMT gain calibration. The event reconstruction efficiency is generally around 90% and is limited by the algorithm's ability to reconstruct multiple scattering events. The total efficiency of the signal is tabulated in Tab. 8.2 as a function of the contributing factors.

Table 8.2: Contributions to the total efficiency of the $2\nu\beta\beta$ signal.

	^{96}Zr signal efficiency (%)	
	individual	combined
hardware trigger	30.34	30.34
detector status	86.37	26.20
reconstruction	95.12	24.93
selection criteria	30.16	7.52
total efficiency	7.52	

8.2 Measurement of the $2\nu\beta\beta$ decay half-life

898 data events have been selected after 1221 days of data taking with a total expected background of 437.6 ± 7.2 events. The estimated background activities from Sec. 7.3.1 and 7.4.1 are applied for the two-electron analysis and the breakdown of individual background contributions is shown in Tab. 8.3. The $2\nu\beta\beta$ signal is fit to background-subtracted data using the log-likelihood method (Sec. 6.4.3), which predicts 429.2 ± 26.2 signal events (signal-to-background of 0.98) with a 7.5% efficiency. The two-electron summed energy data is described by the $2\nu\beta\beta$ signal and the sum of expected backgrounds as seen in Fig. 8.4(a) and the background-subtracted data is described by only the $2\nu\beta\beta$ signal in Fig. 8.4(b). A unique feature of the NEMO-3 detector is the obtained topological information. The angular distribution of the two electrons (as seen in Fig. 8.5(a)) provides information which discriminates between different $0\nu\beta\beta$ mechanisms. The angular distribution also verifies the background model. Distributions of the individual electron energy (Fig. 8.5(b)), the minimum energy elec-

Table 8.3: The number of events expected for the ^{96}Zr internal and external backgrounds in the ee channel for 1221 days of run time.

Background	Expected N_{bkg}	Eff. (%)
^{228}Ac	11.1 ± 0.9	0.042
^{212}Bi	9.6 ± 0.7	0.036
^{208}Tl	9.3 ± 0.7	0.098
^{214}Bi	22.8 ± 2.5	0.12
^{214}Pb	3.3 ± 0.4	0.017
^{40}K	280.0 ± 2.4	0.014
^{234m}Pa	38.3 ± 0.7	0.074
^{48}Ca internals	0.0 ± 0.0	
^{150}Nd internals	37.6 ± 3.2	
External	25.6 ± 5.2	
Total	$\mathbf{437.6 \pm 7.2}$	

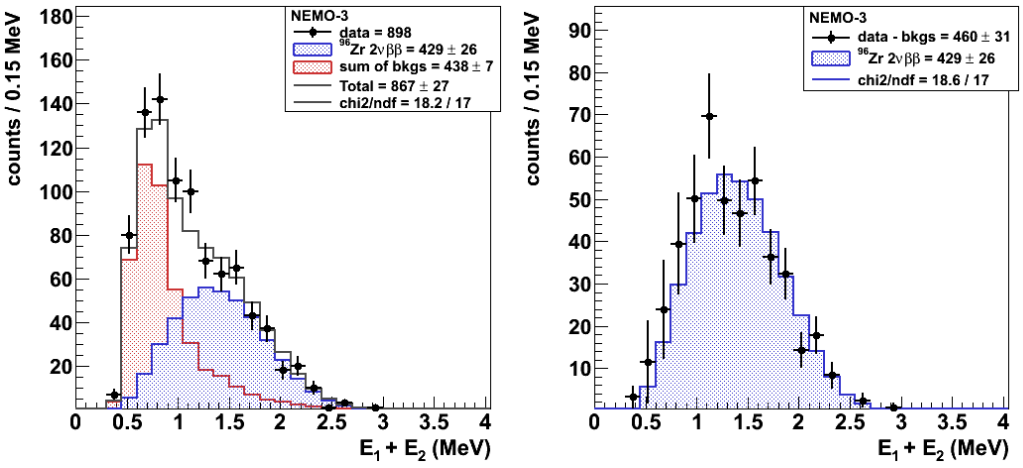

(a) data described by signal and backgrounds (b) background-subtracted data described by signal

Figure 8.4: The energy sum of both electrons $E_1 + E_2$ for (a) the data described by the $2\nu\beta\beta$ signal and the sum of expected backgrounds and (b) the background-subtracted data described by only the $2\nu\beta\beta$ signal.

tron (Fig. 8.5(c)), and the maximum energy electron (Fig. 8.5(d)) are useful for the same reasons of $0\nu\beta\beta$ mechanism discrimination and background model verification.

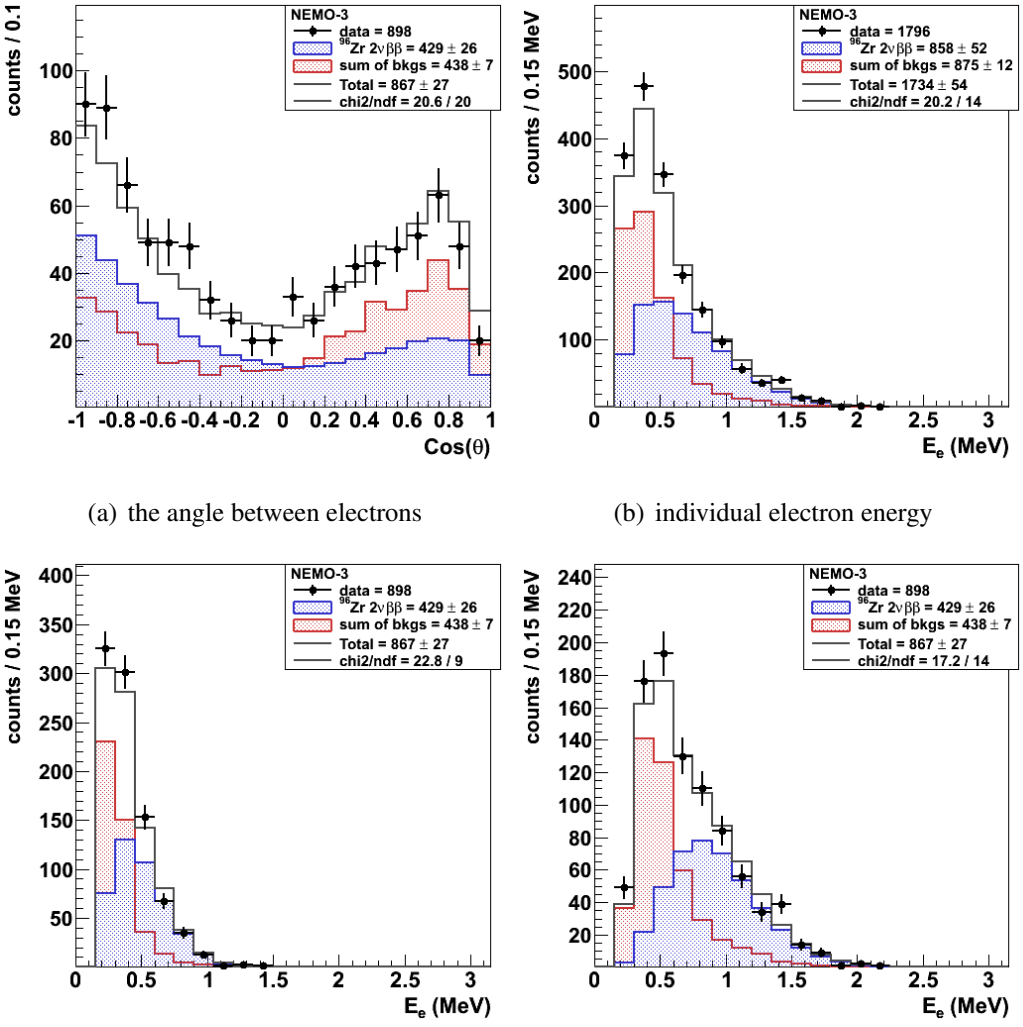

(a) the angle between electrons

(b) individual electron energy

(c) minimum energy electron

(d) maximum energy electron

Figure 8.5: Distributions of (a) the cosine of the angle between electrons, (b) individual electron energy E_e, (c) the minimum energy electron E_e, and (d) the maximum energy electron for 1221 days of run time in the two-electron channel. The data are described by the sum of the expected backgrounds from MC and the $2\nu\beta\beta$ signal from the log-likelihood fit (Sec. 6.4.3).

8.2.1 A study of the systematic error

The systematic error on the $2\nu\beta\beta$ measurement has thoroughly been investigated. The main contribution is from the error on the detector acceptance and reconstruction efficiency [94]. The ^{207}Bi calibration sources have a precisely known activity and

with this information the geometrical acceptance and reconstruction efficiency of $\beta\beta$ type events are evaluated. The detector is not perfectly simulated in GEANT-3.21 and therefore introduces a systematic error. The reconstruction algorithm constrains the two tracks to have a common vertex and thereby introduces a systematic error. The total acceptance and reconstruction systematic error is evaluated by comparing the precising calculable number of expected ee type ^{207}Bi events with observation and is $\pm 5\%$.

The systematic uncertainty of the external background model is considered. ^{214}Bi and ^{208}Tl in the tracking chamber show a discrepancy between the channels they are measured in. ^{214}Bi is measured in the $e\gamma$ and $e\alpha$ channels and the obtained values differ by $\sim 10\%$ [93]. ^{208}Tl is measured in the $e\gamma\gamma$ and $e\gamma\gamma\gamma$ channels and the obtained values differ by $\sim 10\%$ [93]. A conservative estimation on the total external background uncertainty is therefore 10% and is evaluated by fluctuating the external background $\pm 10\%$. The attributed uncertainty on the measured half-life is $\pm 0.3\%$.

There is a 2% uncertainty in the mass of ^{96}Zr [94]. The precision of the energy calibration of the calorimeter is 1% and the effect was determined by coherently changing the gain of the PMTs $\pm 1\%$ and observing the change in half-life. The systematic error on individual internal background isotopes is estimated by the difference in measured activity in the $1e$ and $e\gamma$ channels. The difference never exceeded 5% for the internal backgrounds, therefore the uncertainty on the $2\nu\beta\beta$ half-life is estimated by fluctuating the internal backgrounds $\pm 5\%$ and recording the corresponding change in $2\nu\beta\beta$ half-life.

The recent world's best $2\nu\beta\beta$ half-life measurements for ^{150}Nd [36, 53] and ^{48}Ca [102] have been published by fellow NEMO-3 colleagues. These isotopes neighbour the ^{96}Zr source and are included as backgrounds. The uncertainty in their measured half-lives is applied and the change in the ^{96}Zr half-life is noted. The $2\nu\beta\beta$ half-life of ^{150}Nd is known to 10% (including statistical and systematic errors) and contributes a $\pm 0.7\%$ error on the obtained ^{96}Zr half-life. The $2\nu\beta\beta$ half-life of ^{48}Ca is known to 18% (including statistical and systematic errors) and contributes a $\pm 0\%$ error on the obtained ^{96}Zr half-life.

^{40}K is the dominant background in the ee channel and a systematic effect is observed by changing the energy window of the likelihood fit to exclude energy sums below 1.1 MeV. The strict energy window suppresses ^{40}K events and reduces the half-

life dependence on the activity of ^{40}K. The obtained systematic uncertainties are listed in Tab. 8.4 and give a total systematic error of +6.7% and –6.2%.

Table 8.4: Summary of systematic errors pertaining to the $2\nu\beta\beta$ measurement of ^{96}Zr.

Description	Syst. Error (%)	
acceptance and reconstruction	± 5.0	[94]
±1% energy calibration precision	+ 2.9, – 2.2	
the mass of ^{96}Zr	± 2.0	[94]
±10% external background precision	± 0.3	[93]
±10% ^{150}Nd precision	± 0.7	[53]
±5% internal background precision	± 1.9	
the likelihood fit energy window	+ 1.6, – 0.2	
Total Systematic Error	**+ 6.7%, – 6.2%**	

The final result for the $2\nu\beta\beta$ half-life of ^{96}Zr including statistical and systematic errors is

$$T_{1/2}^{2\nu} = [2.35 \pm 0.14(stat) \pm 0.16(syst)] \times 10^{19}\,\mathrm{yr}\,. \tag{8.2.1}$$

For comparison, (Eq. 8.2.1) is consistent and ∼4 times more precise than the previous direct measurement $(2.1^{+0.8}_{-0.4}(stat) \pm 0.2(syst)) \times 10^{19}$ yr [103].

8.3 $0\nu\beta\beta$ decay (neutrino mass mechanism)

The mass mechanism ($\langle m_{\beta\beta}\rangle$) is the most discussed scenario as previously described in Sec. 3.3.1. No excess of events is observed in the $0\nu\beta\beta$ energy region (3.35 MeV), therefore a limit on $\langle m_{\beta\beta}\rangle$ is evaluated using the LLR method as described in Sec. 6.4.5. The obtained half-life limit is visually represented in Fig. 8.6. Less than 2.9 $0\nu\beta\beta$ events are expected at the 90% CL and the detection efficiency for observing the $0\nu\beta\beta$ decay is 19.9%. The limit obtained at the 90% CL (Fig. 8.6) is

$$T_{1/2}^{0\nu} > 9.2 \times 10^{21}\,\mathrm{yr}\,. \tag{8.3.1}$$

This limit is validated with the so called Helene method as published in [104] using an energy window of 2.7-4.0 MeV. 1.48 ± 0.07 background events are expected, 1 data

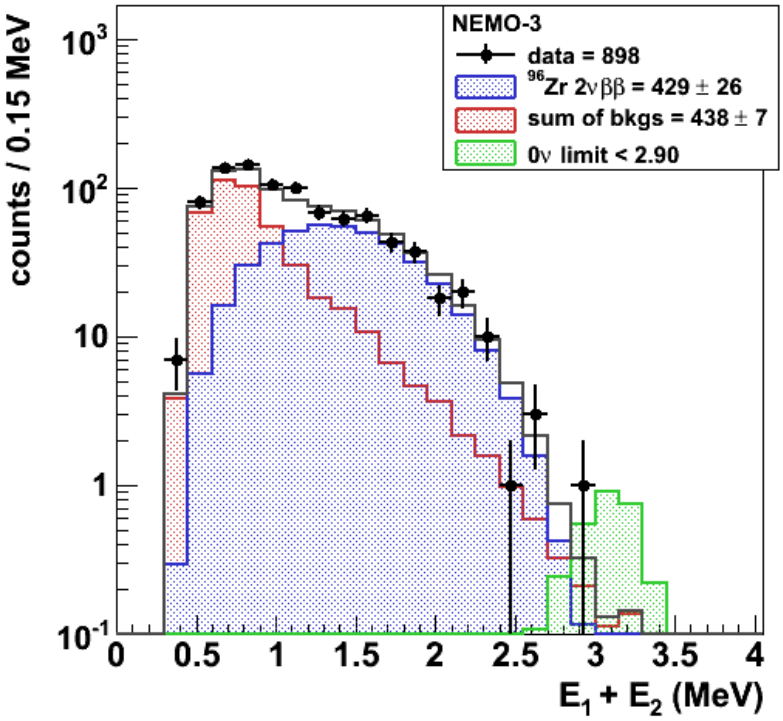

Figure 8.6: Energy sum distribution of two electrons $E_1 + E_2$ for 1221 days of run time. The data are described by the sum of the expected backgrounds from MC, the measured $2\nu\beta\beta$ signal, and the limit on the $0\nu\beta\beta$ mass mechanism at 90% CL using the LLR method described in Sec. 6.4.5. The $0\nu\beta\beta$ histogram is not included in the total MC (dark-grey line)

event is observed, and < 3.12 $0\nu\beta\beta$ events are expected at the 90% CL. The $0\nu\beta\beta$ detection efficiency is 18.4% and the limit obtained at the 90% CL is $> 7.9 \times 10^{21}$ yr.

8.3.1 Other $0\nu\beta\beta$ transitions

Other mechanisms include 0ν excited states, right-handed currents ($\langle\lambda\rangle$ and $\langle\eta\rangle$) and the emission of one or two Majoron particles as described in Sec. 3.3.2. The limits have been obtained using the LLR method described in Sec. 6.4.5 at the 90% CL. The limits obtained for $\langle m_{\beta\beta}\rangle$ and $\langle\lambda\rangle$ half-lives are presented in Tab. 8.5 and the limits obtained for Majoron emission half-lives are presented in Tab. 8.6. Naively one would expect the mass mechanism and $\langle\lambda\rangle$ limit to be identical because they have the same summed energy spectrum, but due to the asymmetrical energies and preferentially small angle ($\cos\theta \sim 1$) between the emitted electrons in the $\langle\lambda\rangle$ process, detector efficiencies decrease the acceptance, thereby weakening the $\langle\lambda\rangle$ limit.

Table 8.5: Summary of half-life limits $T_{1/2}$ (yr.) evaluated at the 90% CL for $0\nu\beta\beta$ mechanisms where $0^+_{gs}(\langle m_{\beta\beta}\rangle)$ is the standard $0\nu\beta\beta$ decay to the ground state, $0^+_1(\langle m_{\beta\beta}\rangle)$ is the first excited state, $0^+_{gs}(\langle\lambda\rangle)$ is the right-handed current decay to ground state and $2^+_1(\langle\lambda\rangle)$ is the first excited state.

			limit at 90% CL (yr)	
decay mech.	Eff. (%)	Exp. $N_{0\nu}$	NEMO-3	previous best
$0^+_{gs}(\langle m_{\beta\beta}\rangle)$	19.9	2.90	9.2×10^{21}	1.0×10^{21}[103]
$0^+_1(\langle m_{\beta\beta}\rangle)$	2.02	13.4	2.2×10^{20}	6.8×10^{19}[105]
$0^+_{gs}(\langle\lambda\rangle)$	11.1	2.93	5.1×10^{21}	-
$2^+_1(\langle\lambda\rangle)$	5.98	8.82	9.1×10^{20}	3.9×10^{20}[103]

The $n = 1$ Majoron emission mechanism ($\langle g_{\chi^0}\rangle$) is the most discussed Majoron scenario as previously described in Sec. 3.3.2. The obtained half-life limit is displayed in Fig. 8.7.

Table 8.6: Summary of half-life limits $T_{1/2}$ (yr.) evaluated at the 90% CL for Majoron emission decay mechanisms. The spectral index (n) for the Majoron modes refers to the dependence of $G^{0\nu} \propto (Q_{\beta\beta} - E_{sum})^n$ where E_{sum} is the electrons' kinetic energy sum. The bottom line is the previous best limit presented for comparison.

			limit at 90% CL (yr)	
Majoron	Eff. (%)	Exp. $N_{0\nu}$	NEMO-3	previous best
$n = 1$	15.6	11.0	1.9×10^{21}	3.5×10^{20}[106]
$n = 2$	13.0	17.6	9.9×10^{20}	-
$n = 3$	10.8	24.9	5.8×10^{20}	6.3×10^{19}[106]
$n = 7$	4.72	59.9	1.1×10^{20}	5.1×10^{19}[106]

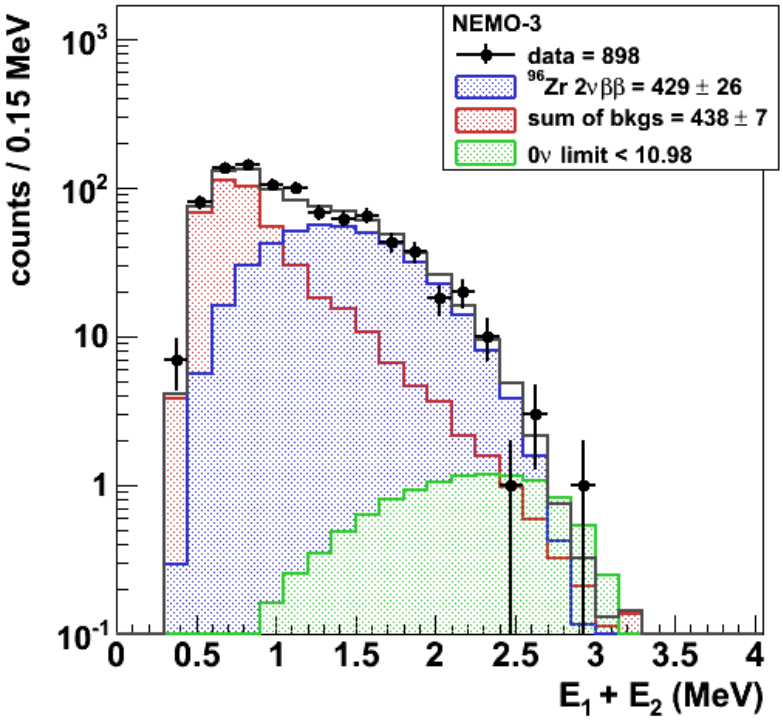

Figure 8.7: Energy sum distribution of two electrons $E_1 + E_2$ for 1221 days of run time. The data are described by the sum of the expected backgrounds from MC, the measured $2\nu\beta\beta$ signal, and the limit on $n = 1$ Majoron emission at 90% CL using the LLR method described in Sec. 6.4.5. The 0ν histogram is not included in the total MC (dark-grey line)

8.4 Discussion

8.4.1 $2\nu\beta\beta$ nuclear matrix element

The largest uncertainty in the effective Majorana mass determination is due to the uncertainty of $M^{0\nu}$. As described in Sec. 3.4 there is much discussion about the handling of g_{pp} and g_A parameters. Due to strong dependence of $M^{0\nu}$ on the unknown parameter g_{pp}, it is argued [43] to fix g_{pp} to the experimentally extracted value of $M^{2\nu}$ for accurate calculations of $M^{0\nu}$. Using the measured value of the ^{96}Zr $2\nu\beta\beta$ half-life (Eq. 8.2.1) we extract the experimental value of the corresponding NME according to Eq. 3.2.3 reiterated here

$$(T^{2\nu}_{1/2})^{-1} = G^{2\nu} \left|M^{2\nu}\right|^2 ,$$

where $G^{2\nu} = 1.8 \times 10^{-17}\,\mathrm{yr}^{-1}$ is the known phase space factor evaluated for $g_A = 1.25$ [43]. The obtained result is scaled by the electron rest mass and is

$$M^{2\nu} = 0.049 \pm 0.002\,. \tag{8.4.1}$$

One can compare this (Eq. 8.4.1) value with the PHFB (Sec. 3.4.3) calculation, $M^{2\nu} = 0.058$ [107]. The obtained precise value for $M^{2\nu}$ will be used to improve future $M^{0\nu}$ calculations for ^{96}Zr.

8.4.2 The effective Majorana neutrino mass

The limit on the $0\nu\beta\beta$ half-life (Eq. 8.3.1) is used to calculate an upper bound on the effective Majorana neutrino mass from Eq. 3.3.2. Using the NME computed in QRPA [108, 109], (R)QRPA [42, 110], and PHFB [47], Tab. 8.7 displays the obtained limits on effective Majorana neutrino mass as a function of g_A and g_{pp}. The effective

Table 8.7: Effective Majorana neutrino mass using NME from QRPA, (R)QRPA, and PHFB models as a function of g_A and g_{pp}.

Model	g_A	g_{pp}	$\langle m_{\beta\beta}\rangle$ (eV)	Ref.
QRPA	1.25	1.11	7.2–10.8	[108]
QRPA	1.00	1.06	8.1–11.2	[108]
QRPA	1.25	1.00	8.2	[109]
(R)QRPA	1.25	$2\nu\beta\beta$	16.3–17.5	[42]
(R)QRPA	1.00	$2\nu\beta\beta$	16.1–17.4	[42]
(R)QRPA	1.25	$2\nu\beta\beta$	15.0–19.4	[110]
(R)QRPA	1.00	$2\nu\beta\beta$	11.0–14.7	[110]
PHFB	1.25	–	15.1–15.4	[47]

Majorana neutrino masses are summarized by NME model

$$\langle m_{\beta\beta}\rangle < 7.2 - 11.2\,\mathrm{eV} \quad \mathrm{QRPA}\,[108,\ 109]\,, \tag{8.4.2}$$

$$\langle m_{\beta\beta}\rangle < 11.0 - 19.4\,\mathrm{eV} \quad \mathrm{(R)QRPA}\,[42,\ 110]\,, \tag{8.4.3}$$

$$\langle m_{\beta\beta}\rangle < 15.1 - 15.4\,\mathrm{eV} \quad \mathrm{PHFB}\,[47]\,. \tag{8.4.4}$$

8.4.3 The Majoron-neutrino coupling factor

A limit on the Majoron to neutrino coupling $\langle g_{\chi^0} \rangle$ is extracted for the most commonly discussed mechanism with $n = 1$ from Eq. 3.3.4. The Majoron matrix element is identical to that of the mass mechanism allowing the same NME for QRPA, (R)QRPA, and PHFB from Sec. 8.4.2 to be used. Tab. 8.8 displays the obtained limits on the Majoron to neutrino coupling as a function of g_A and g_{pp}. The obtained Majoron to

Table 8.8: Majoron to neutrino coupling using NME from QRPA, (R)QRPA, and PHFB models as a function of g_A and g_{pp}.

Model	g_A	g_{pp}	$\langle g_{\chi^0} \rangle$ ($\times 10^{-4}$)	Ref.
QRPA	1.25	1.11	2.1–3.2	[108]
QRPA	1.00	1.06	1.5–2.1	[108]
QRPA	1.25	1.00	5.2	[109]
(R)QRPA	1.25	$2\nu\beta\beta$	4.8–5.1	[42]
(R)QRPA	1.00	$2\nu\beta\beta$	4.8–5.1	[42]
(R)QRPA	1.25	$2\nu\beta\beta$	4.4–5.7	[110]
(R)QRPA	1.00	$2\nu\beta\beta$	3.2–4.3	[110]
PHFB	1.25	–	4.0–4.6	[47]

neutrino couplings are summarized by NME model

$$\langle g_{\chi^0} \rangle < (1.5 - 2.1) \times 10^{-4} \quad \text{QRPA [108, 109]}, \tag{8.4.5}$$

$$\langle g_{\chi^0} \rangle < (3.2 - 5.7) \times 10^{-4} \quad \text{(R)QRPA [42, 110]}, \tag{8.4.6}$$

$$\langle g_{\chi^0} \rangle < (4.0 - 4.6) \times 10^{-4} \quad \text{PHFB [47]}. \tag{8.4.7}$$

The obtained values are very competitive with the current best result $\langle g_{\chi^0} \rangle < 1.9 \times 10^{-4}$[111] especially considering only 9.4 g ^{96}Zr isotope is used.

8.4.4 G_F time variation hypothesis

It has been suggested in [112, 113] that observed differences in half-lives of $2\nu\beta\beta$ isotopes obtained in geochemical experiments with samples of different age could be related to time dependence of the Fermi constant G_F. Due to the stronger dependence

on the Fermi constant (G_F^4 rather than G_F^2), $2\nu\beta\beta$ decay offers a better sensitivity than single β decay studies. The $^{96}\mathrm{Zr}-^{96}\mathrm{Mo}$ transition is of particular interest since the daughter element is not a gas thus eliminating the main systematic error of the geochemical measurements. A comparison between the half-lives obtained with ancient zircon ($ZrSiO_4$) minerals characterizing the decay rate in the past with present day $2\nu\beta\beta$ decay rates obtained in a direct experiment like the one presented here allows the hypothesis to be probed with a high precision.

A previous geochemical measurement carried out in 1992 with a 1.7×10^9 yr old zircon yielded a $2\nu\beta\beta$ half-life of $(3.9 \pm 0.9) \times 10^{19}$ yr [114]. An independent measurement was performed in 2001 with a number of zircons aged $\sim 1.8 \times 10^9$ yr and a half-life of $(0.94 \pm 0.32) \times 10^{19}$ yr was measured [115]. The measurement presented here (Eq. 8.2.1) lies between the two geochemical measurements. More accurate studies of minerals of different age are needed in order to probe the G_F time variation hypothesis with high precision.

Part II

SuperNEMO calorimeter development

Chapter 9

The SuperNEMO baseline design

The success of NEMO-3 influenced the technical design of SuperNEMO which will contain 100 kg of source isotope and rely on the same tracking detector plus calorimeter concept as NEMO-3. SuperNEMO will not just be a scaled up version of NEMO-3, but will utilize developed technologies to surpass the performance of NEMO-3. SuperNEMO will have a sensitivity to the effective neutrino mass of ~ 50 meV which excludes the degeneracy model and gives access to the inverted hierarchy (Fig. 3.4). A comprehensive design study has been carried out in the last 4 years during which major technological challenges have been successfully addressed. SuperNEMO is now entering its construction phase and the first super-module will be ready for installation in an underground laboratory in 2013.

Due to the proven success of NEMO-3, SuperNEMO is designed with similar detector components. Thin foils at the center of the detector volume contain the source isotope. A drift-cell tracking chamber operating in Geiger mode surrounds the source foils for particle identification and background rejection. The tracking volume is enclosed by the calorimeter which will measure the deposited energy. All detector components need to be ultra radiopure and passive shielding and an underground location is required for background suppression.

9.1 The SuperNEMO detector

SuperNEMO (Fig. 9.1) is a 100 kg source isotope (^{82}Se is the baseline), calorimeter plus tracking detector with a projected neutrinoless double-beta decay half-life sensitivity of 10^{26} years (50-90 meV effective Majorana neutrino mass). The baseline design calls for 20 modules, each ~ 6 x 2 x 4 meters and holding 5 kg of source isotope.

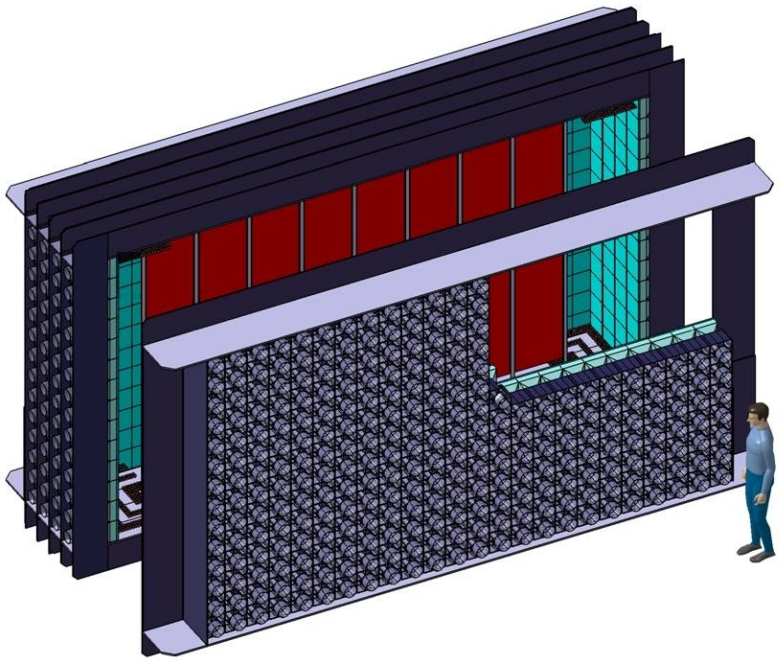

Figure 9.1: One of the SuperNEMO baseline modules $\sim$ 6 x 2 x 4 meters. The calorimeter wall is pulled out to expose the tracker volume and source foils (dark red) which span across the center of the module. There will be 20 modules in total, each holding 5 kg of source isotope.

The source is a thin ($\sim 40\,\mathrm{mg/cm^2}$) foil suspended vertically through the center of the module. Each module is a self-contained detector capable of operating independently. The modular design is beneficial because it provides locational flexibility (as underground laboratories have various floor area geometries), ease of transport (because the modules will not be constructed within the underground laboratory), a quicker commissioning time, and data taking will begin after the installation of the first module.

The project is coming to the end of its research and development (R&D) phase, and includes over 90 scientists from 12 countries, with the United Kingdom and France contributing the most effort. The source enrichment, tracker drift cells, and calorimeter block is based on the proven technology of NEMO-3, but necessary technological improvements have been made and the design study explores alternative options to further the detector performance. The R&D is focused on four main areas of study: source enrichment and purification, drift-cell tracking detector, scintillator calorimeter, and software development. The goals of SuperNEMO R&D are compared to the NEMO-3 performance in Tab. 9.1.

Table 9.1: SuperNEMO R&D parameters and baseline design objectives compared to NEMO-3. The SuperNEMO $T^{0\nu}_{1/2}$ and $\langle m_{\beta\beta}\rangle$ sensitivities are for 500 kg·y.

Parameter	SuperNEMO	NEMO-3
Source isotope	$^{82}\mathrm{Se}$	$^{100}\mathrm{Mo}$
Isotope mass	100 kg	7 kg
$0\nu\beta\beta$ detection efficiency	30%	18%
Energy resolution	7-8% at 1 MeV	14-17% at 1 MeV
$^{214}\mathrm{Bi}$ source purity	$< 10\,\mu$Bq/kg	$< 300\,\mu$Bq/kg
$^{208}\mathrm{Tl}$ source purity	$< 2\,\mu$Bq/kg	$< 20\,\mu$Bq/kg
$T^{0\nu}_{1/2}$ sensitivity	1×10^{26} yr	2×10^{24} yr
$\langle m_{\beta\beta}\rangle$ sensitivity	50 – 90 meV	0.3 – 0.9 eV

The SuperNEMO sensitivity has been studied as a function of parameters such as calorimeter energy resolution, source purity, and exposure and the target sensitivity of 50-90 meV (10^{26} yr) has been confirmed. Simulations show the sensitivity as a function

of energy resolution for three source purity models and a fixed exposure of 500 kg·y (as seen in Fig. 9.2(a)) and the sensitivity as a function of exposure (kg·y) for three source purity models and a fixed energy resolution of 7% FWHM at 1 MeV (as seen in Fig. 9.2(b)). The sensitivity curves follow the trend and confirm the expectation of the analytic expression Eq. 9.2.1.

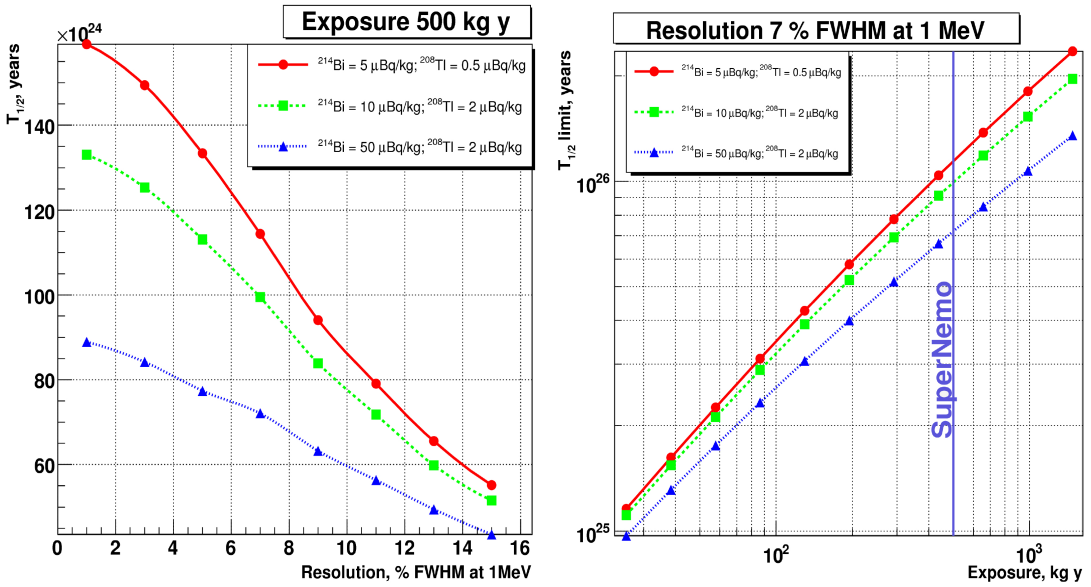

(a) sensitivity as a function of energy resolution (b) sensitivity as a function of exposure

Figure 9.2: SuperNEMO half-life sensitivity as a function of energy resolution with a fixed exposure of 500 kg·y (a) and a function of exposure with a fixed energy resolution of 7% FWHM at 1 MeV (b). Three background models are considered. The GREEN curve represents the radiopurity baseline design, the RED curve displays an enhanced radiopurity, and the BLUE curve shows a degraded radiopurity.

The energy resolution requirement is chosen to create a distinct separation between the high energy $2\nu\beta\beta$ tail and the peak of the $0\nu\beta\beta$ energy distribution (Sec. 9.2). The limiting factor in the SuperNEMO configuration is the partial energy loss of the electron exiting the source foil. This smears the energy distribution and causes an effective energy resolution of $\sim$5-6%. A calorimeter energy resolution better than this is negated by the energy smearing due to the source foil.

Source enrichment and purification is carried out through chemical and physical methods and mass production has become cheaper. An innovative Bi-Po detector measures the source radiopurity because modern HPGe detectors cannot reach the target

sensitivity. The detector has been successfully commissioned and a sensitivity of few μBq/kg for $^{238}\mathrm{U}$ and $^{232}\mathrm{Th}$ has been demonstrated [116]. The tracking detector of each module is composed of $\sim$2000 drift-cells operating in Geiger mode. Challenges in drift-cell technology include plasma initiation and propagation efficiency, crosstalk, physical wiring of the cell, aging, and radiopurity. A full chain of MC simulation and analysis software has been developed based on C++, ROOT, and GEANT-4.9 and the tracking reconstruction efficiency has been improved through new algorithms. Two designs have been investigated for the calorimeter. The so-called bar design requires less PMTs, is more compact, provides better background suppression, and is much cheaper. The disadvantages of this approach are the degraded energy resolution, uniformity and timing. The so-called block design is the focus of this presented research. The block design is advantageous due to unprecedented energy resolution and fast timing but requires more PMTs and scintillator mass and is therefore more expensive.

9.2 SuperNEMO calorimeter

The baseline design calls for each SuperNEMO module to be equipped with $\sim$700 scintillator blocks coupled to $\oslash$8" PMTs. Many geometries were studied but optical simulations [117] and data show a hexagonal design to perform better. Unprecedented energy resolution is required for SuperNEMO low Z scintillator calorimeter. The significance of energy resolution is best illustrated by the following expression for the half-life sensitivity from Ref. [118]

$$T_{1/2} \propto \frac{\varepsilon}{\kappa_{CL}} \frac{N_A ln(2)}{A} \sqrt{\frac{M \cdot t}{N_{bkg} \cdot \Delta E}}\,, \tag{9.2.1}$$

where ε is the detector efficiency, κ_{CL} is the number of excluded events at the desired confidence level, A is the atomic number of the isotope under study, and N_A is Avogadro's number. The energy resolution (ΔE) factors in with equal importance as isotope mass (M), run time (t), and rate of background events (N_{bkg}). Eq. 9.2.1 has limitations in accurately predicting the sensitivity of the specific SuperNEMO detector, but demonstrates the significance of energy resolution. The dominating background to $0\nu\beta\beta$ is the irreducible $2\nu\beta\beta$ channel, therefore the energy resolution of the calorimeter becomes the dominating parameter determining the detector's overall sensitivity to neutrinoless double-beta decay.

Simulations done for ^{82}Se with an effective calorimeter energy resolution of 12% and 7% FWHM at 1 MeV and normalized to 10^{26} year $0\nu\beta\beta$ half-life (seen in Fig. 9.3), clearly displays the importance of energy resolution for this experiment. At 12%

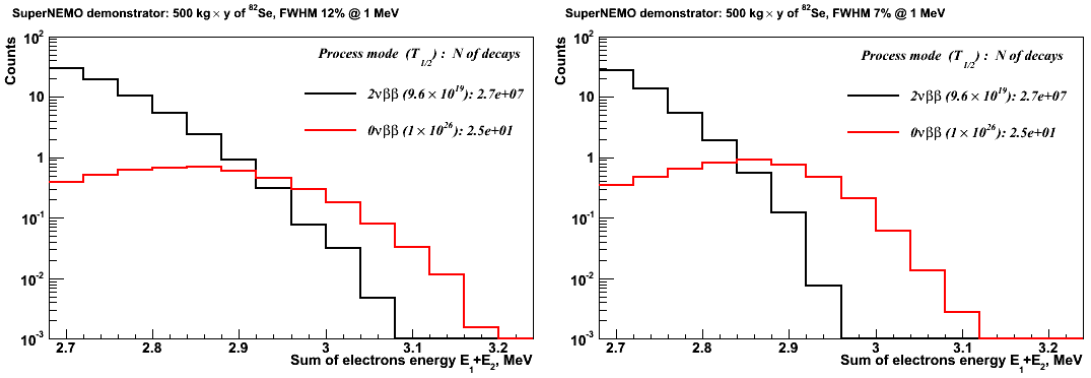

(a) 12% FWHM at 1 MeV (b) 7% FWHM at 1 MeV

Figure 9.3: Simulations for 500 kg·y ^{82}Se. The $0\nu\beta\beta$ half-life (RED) is normalized to 10^{26} years. Expectations for energy resolutions 12% (a) and 7% (b) FWHM at 1 MeV.

FWHM at 1 MeV, the high energy tail from the $2\nu\beta\beta$ energy spectrum significantly overlaps the $0\nu\beta\beta$ peak, but at 7% FWHM at 1 MeV energy resolution there is clear separation.

The calorimetry R&D is subdivided into three main objectives: calibration, PMT radio-purity, and the main focus on achieving an energy resolution $< 7\%$ FWHM at 1 MeV. As with all PMT based calorimeters, PMT gain stability and linearity must be both intrinsically good and experimentally well understood to ensure the accurate reconstruction of data. Calibrated light injection systems and embedded α sources are investigated for gain and linearity monitoring solutions.

PMTs are one of the main sources of external contamination (Sec. 7.2) with emphasis on the purity of the glass due to its proximity to the active volume. The Barium salt used to make conventional glass is chemically similar to Radium, and therefore very difficult to purify during the production of the glass. Various manufacturers have developed recipes for low-background glass, but the requirements of SuperNEMO have motivated this development to a new level of radiopurity. Preliminary samples of a new ultra-pure synthetic silica glass (provided by Photonis) have met the R&D target of < 40 mBq/kg of ^{214}Bi (Fig. 9.4).

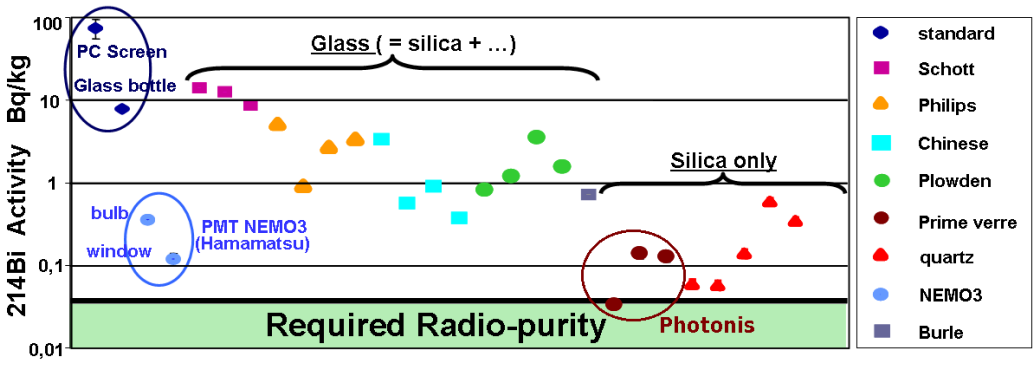

Figure 9.4: Radioactive purity measurements for types of glass used for PMT windows.

Chapter 10

Factors influencing energy resolution

As illustrated in Fig. 9.2, the calorimeter energy resolution plays an important role in achieving a 10^{26} yr half-life sensitivity, but other calorimeter requirements limit the options. Probability for back-scattering must be low to maintain the detection efficiency. A high gamma efficiency is needed for background suppression. Fast timing of the scintillator and PMT is required for accurate time-of-flight information. Radiopurity of the scintillator and PMT must be considered. The gain stability and linearity of the PMT are also important. The underlying factor is cost. This chapter addresses these factors, the limitations they present, and how they are overcome.

10.1 The energy resolution

The energy resolution $\Delta E/E$ for scintillation detectors is dominated by stochastic photon fluctuations. For large N_{pe} (>20) a valid approximation for the energy resolution is expressed

$$\frac{\Delta E}{E} = \frac{2.35\,\sigma}{E} = \frac{2.35}{\sqrt{N_{pe}}}\,. \tag{10.1.1}$$

where N_{pe} is the number of photo-electrons and the factor of 2.35 translates 1σ to the full-width at half-maximum (FWHM). This is simplified into three experimental objectives described by

$$N_{pe} \propto \frac{N_{ph}}{E_e} \cdot \varepsilon_{col}^{light} \cdot \left(QE^{PMT} \cdot \varepsilon^{PMT}\right)\,, \tag{10.1.2}$$

where $\dfrac{N_{ph}}{E_e}$ is the number of photons produced per unit energy deposited and is determined by the scintillator light yield. $\varepsilon_{col}^{light}$ is a generalized light collection efficiency which depends upon the scintillator geometry, light attenuation length, reflector re-

flectance, and optical coupling quality. Intrinsic characteristics of the PMT include the quantum efficiency of the photo-cathode QE^{PMT}, and the collection efficiency ε^{PMT}.

10.2 Scintillator types

Non-organic scintillators have a high light yield but are disadvantaged by their high back-scattering, slow timing, and often non-sufficient level of radiopurity. Organic liquid scintillator was a contender due to its advantageous low back-scattering, good uniformity, fast timing, and radiopurity, but it has major drawbacks of the mechanical containment design, entrance window and health and safety issues. Organic solid scintillators are preferred for their low back-scattering, fast timing, high radiopurity and simple mechanical design relative to liquid. The focus of this research is therefore on the organic solid scintillator, PVT (polyvinyl toluene) in particular.

The scintillator choice is restricted to low Z materials because electron back-scattering is proportional to Z^2. Back-scattering reduces the detection efficiency and is therefore an undesirable effect. Consequently NaI, CsI, mineral oils, and other high Z types are not candidates for the SuperNEMO calorimeter. PST (polystyrene) based scintillator light conversion efficiency is not to the standard of high Z types but innovative advances have been made. The PST type scintillators generally produce ~ 7000 ph/MeV while PVT types produce $\sim 10{,}000$ ph/MeV. Good timing resolution (< 250 ps @ $1\,\sigma$) is required from the scintillators for low level triggering and accurate TOF information and this requirement excludes mineral oils and other inorganic scintillators. Tab. 10.1 lists the candidates which were chosen for testing compared to typical PST characteristics. Scintillator uniformity can be problematic for large geometries because uniform cooling during manufacturing is directly related to the uniformity of the light yield. Cast scintillators tend to be more uniform than extruded types but also cost more. Fortunately, PST and PVT are both generally very pure of radioactive contamination. PVT has a better light yield than PST but PVT presents additional concerns. PVT corrodes ("crazes") when in contact with many common substances including the natural oils on your hands and fingers. For this reason, gloves are always worn when handling the scintillator. PVT will craze when exposed to sudden temperature fluctuations as discovered when using ethanol or methanol to clean the surface. Propanol is therefore used because it evaporates less quickly. PVT is also brittle and can chip

Table 10.1: Candidate scintillators and characteristics. The refractive index is quoted at a wavelength of 589.3 nm.

type	Light Yield (ph/MeV e^-)	Refractive Index	Rise Time (ns)	Attenuation Length (cm)
PST	$\sim$7,000	1.58	$\sim$1	$\sim$200
Bicron BC-404	10,400	1.58	0.7	160
Bicron BC-408	10,000	1.58	0.9	380
Bicron BC-412	9,200	1.58	1.0	400
ELJEN EJ-204	10,400	1.58	0.7	160
ELJEN EJ-200	10,000	1.58	0.9	380
ELJEN EJ-212	9,200	1.58	1.0	400

or crack if impacted. PVT is consequently very difficult to machine due to the above factors.

10.3 Reflector types

The desired characteristics for the reflective material are low Z, low density, highly reflective, and dimensionally thin. As stated in Sec. 10.2 a low Z material is required to minimize back-scattering. We require a low density and dimensionally thin material to reduce energy loss of the electron while it passes through the material, and a highly reflective material more efficiently redirects light towards the PMT photo-cathode. The radioactive purity of the reflective material is a concern but due to its small mass there is some flexibility. The characteristics of the tested reflector types are tabulated in Tab. 10.2. It is interesting to plot the reflectivity as a function of wavelength as done in Fig. 10.1.

10.3.1 Enhanced specular reflector

A relatively new product referred to as ESR (enhanced specular reflector) is on the market. The material is polymer based and composed of many layers forming a gradient of refractive indices. Light with an incident angle $\theta_i < \theta_c$ will refract to the next layer until $\theta_i > \theta_c$ where θ_c is the critical angle. The Vikuiti company markets the product

Table 10.2: Candidate reflective materials and characteristics. Where referenced, independent measurements were carried out.

type	Thickness (μm)	reflectance (%)	Density (mg/cm^2)	Density (g/cm^3)
PTFE ribbon	25	>70	1.0	0.4
PTFE (3 layers)	75	>80	3.0	0.4
Goodfellow Al-Mylar	6	79 ± 4 [119]	0.78-0.84	1.2
Goodfellow Al-Mylar	12	~80	1.6-1.7	1.2
Goodfellow Al-Mylar	25	~80	3.0-3.2	1.2
Vikuiti ESR	65	>98	7.8	1.2
ReflechTech ESR	100	94 ± 4 [119]	12	1.2

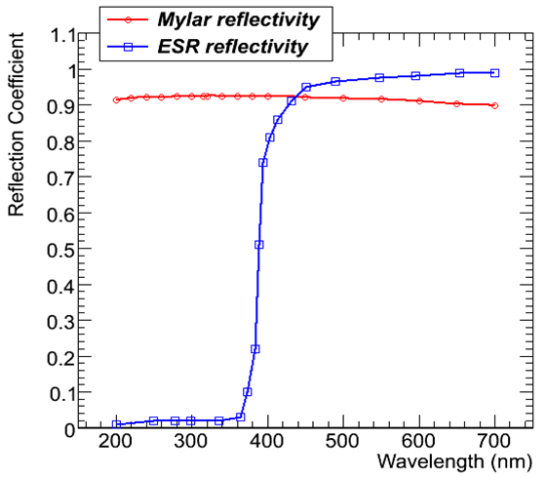

Figure 10.1: Reflectivity as a function of wavelength for Al-Mylar and ESR.

to aid back-lighting of LCDs (liquid crystal display) and is very expensive ($\sim$400 GBP for a 12"$\times$12"sheet). An alternative company ReflechTech markets the product for massive solar reflector applications and sells a 1×60 m roll for $\sim$120 USD. The drastic difference in price suggests the Vikuiti ESR might have a much better reflectance, but the company's specification sheets give similar reflectivity and this is confirmed by our measurements.

10.3.2 PTFE (Teflon)

Reflectance of the PTFE ribbon is difficult to quantify. One layer of PTFE is fairly transparent to the naked eye and better energy resolution is obtained when using three layers. Generally three layers of PTFE performs as well as Al-Mylar and in some scenarios as well as ESR. This is better understood when taking into account the geometry of the scintillator (Sec. 10.3.3). Reflectance measurements of diffusive surfaces require special apparatus to collect the isotropically scattered light and were therefore not carried out on the PTFE.

10.3.3 Diffusive vs. specular reflection

It is possible to obtain two different energy resolutions using diffusive or specular reflectors with the same reflectance. Comprehensive optical simulations [117, 120] help us understand the many factors influencing the amount of light incident on the photo-cathode. Simulations for cubic geometries suggest that large scintillators perform better with diffusive reflection around the lateral sides and small scintillators perform better with specular reflection around the lateral sides. In both cases the face of the scintillator should have specular reflection to redirect light back towards the photo-cathode. This generalization is not true for all geometries because factors such as bulk absorption and surface effects contribute to the total light collection at the photo-cathode. A long bar scintillator for example has a better energy resolution when using specular reflection [121].

10.4 The optical coupling material properties

The overall quality of the optical coupling of the scintillator to PMT affects the energy resolution. The refractive index and transmittance of the coupling material are most important but other factors such as viscosity and corrosivity will indirectly effect the energy resolution. Viscous optical gels such as Bicron's BC-630 generally work well for small flat surfaces and in scenarios where there is no structure to contain a fluid coupling material. Optical gels become problematic with large surface areas and with more complex surfaces. The hemispherical surface of a PMT for example, is troublesome because of the difficulty of removing the air bubbles in the gel. In this case a containment ring fastened around the PMT and scintillator creates a sealed cavity for

optical coupling fluid.

Cargille's type-06350 fluid works well for PST scintillators and PMMA light-guides but crazes PVT scintillator. A coupling fluid which does not craze the PVT is mandatory; therefore new fluids have been investigated. Propanol is an option because it is known to not craze the PVT, but its refractive index does not match the scintillator or PMT glass well and there is concern about evaporation. Glycerol was suggested because its refractive index value is better matched to the scintillator and PMT glass and tests exposing PVT to glycerol show no sign of crazing. Glycerol is more viscous than Cargille type-06350 and propanol but proves sufficient. For the final construction of SuperNEMO an optical epoxy (Stycast-1264) will be used to permanently couple the PMT to scintillator. This is for structural and safety reasons.

Tab. 10.3 shows the optical coupling materials tested for the SuperNEMO calorimeter block. The optimal index of refraction is a value between that of the scintillator and PMT glass to create a gradual change in refractive index.

10.5 Photomultiplier types

Many factors are considered for the candidate PMTs but the dominant parameter affecting the energy resolution is the quantum efficiency (QE) of the photo-cathode. To our advantage, PMT manufactures are developing photo-cathodes with high QE (35-45%). These include Hamamatsu and until recently Photonis. In the spring of 2009 Photonis announced they were shutting down their photo-multiplier branch. The UK group is responsible for the study of Hamamatsu and ETL (Electron Tubes Limited) PMTs while the French group is (was) responsible for studying the Photonis PMTs. ETL is still in the R&D stage of their high QE development and were not able to provide a test PMT. Hamamatsu has developed the so-called Super-Bialkali (SBA) and Ultra-Bialkali (UBA) photo-cathodes whose wavelength vs. QE is given in Fig. 10.2. Hamamatsu SBA technology has been scaled to all cathode sizes, but the UBA technology has only been commissioned for cathodes $\leq \oslash 5$". The Photonis PMTs have been included in Tab. 10.4 because experimental methods (Sec. 11.1) were cross-checked at CENBG (Centre d' Etudes Nucléaires de Bordeaux Gradignan) with both Hamamatsu and Photonis PMTs and results are presented in Sec. 12.3.

Table 10.3: Candidate optical coupling materials and characteristics. The refractive index is quoted at the wavelength of 589.3 nm. For reference, PMMA and a few typical PMT glasses are listed at the bottom. Dynamic (absolute) viscosity values are quoted in centi-Poise (cP) at 25^{o} C. Viscosity of corn syrup and peanut butter are added for comparison.

type	Refractive Index	Viscosity (cP)	Crazes PVT
air	1.000	0.018	no
water	1.333	0.894	no
Propanol	1.378	1.945	no
Cargille 06350	1.459	65.9	yes
Glycerol	1.473	1495	no
Bicron BC-630	1.465	$\sim 10^5$	no
Stycast-1264	1.41-1.56 [119]	–	no
olive oil	–	81	–
corn syrup	–	1380	–
peanut butter	–	2.5×10^5	–
PMMA	1.491	–	–
Crown glass	1.50-1.54	–	–
BK-7	1.517	–	–
borosilicate	1.470	–	–
fused silica	1.458	–	–

10.5.1 ETL (Electron Tubes Limited)

ETL has a reputation for producing extremely radiopure PMTs. From Eq. 9.2.1 the number of background events and energy resolution factor in with equal weight. It is therefore possible that ETL PMTs do not have as good QE as Hamamatsu and Photonis but achieve a radiopurity which maintains the SuperNEMO sensitivity. There are other intrinsic factors which affect energy resolution that are not explicitly stated by manufactures, specifically the first dynode collection efficiency. It is also possible

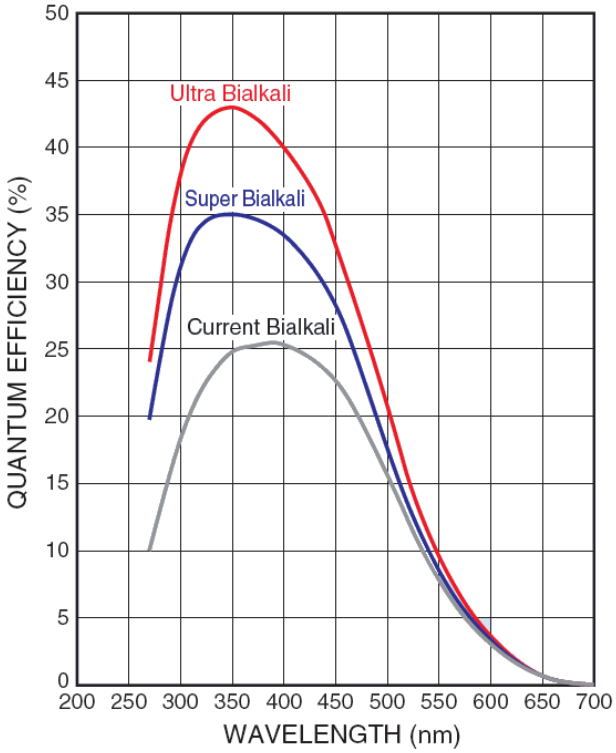

Figure 10.2: Wavelength vs. QE of Hamamatsu photo-cathodes for the standard Bialkali (bottom curve), Super-Bialkali (middle curve), and Ultra-Bialkali (top curve) from Ref. [122].

for a PMT to have a lower QE but higher collection efficiency thereby maintaining performance.

10.5.2 Hamamatsu

Hamamatsu has an R&D program to scale their UBA technology to ⌀ 8" PMTs which is an exciting prospect, but to date is still in development. The ⌀ 8" SBA option is a likely candidate for SuperNEMO and discussions with Hamamatsu were held to improve the linearity and timing of the PMT. Saturation (deviation from linearity) occurs due to the space-charge effect between the last dynode and anode. SuperNEMO $2\nu\beta\beta$ and $0\nu\beta\beta$ measurements are sensitive to the combined energy sum of the two emitted electrons, therefore a PMT linearity past the $Q_{\beta\beta}$ of the source isotope (~ 3 MeV) is required. The baseline energy resolution of 7% FWHM at 1 MeV corresponds to $\sim 1000\, N_{pe}$ using Eq. 10.1.1, and the signal current is determined by the N_{pe} multiplied by the effective gain of the PMT.

Table 10.4: Candidate PMTs and their characteristics.

type	cathode ⌀ (in.)	quoted max QE (%)	QE at 400 nm (%)
Hamamatsu R5912	8”	22	21
Hamamatsu R5912-MOD	8”	33	32
Hamamatsu R6233-100	3”	35	32
Hamamatsu R6233-100-S	3”	43	40
ETL 9360KB	11”	25	23
ETL 9354KB	8”	30	28
ETL 9390KB	5”	28	26
ETL D724KB	5”	25	25
Photonis XP1886-100	8”	25	25
Photonis XP1886-124	8”	28	28
Photonis XP1886-160	8”	35	34

A possible solution suggested by Hamamatsu was the implementation of an 8-dynode chain (typically 10-dynodes) into the 8” Hamamatsu R5912-MOD. The 8-dynode chain offers an improved linearity (2% deviation at ~ 100 mA) and faster timing than the 10-dynode chain. Measurements of the gain and linearity (Sec. 11.3) were therefore necessary for comparison to the values expected by Hamamatsu.

Chapter 11

The calorimeter test-bench

The test-bench has been developed and built capable of performing energy resolution measurements of the full calorimeter block (scintillator + reflector + lightguide + PMT) and also characterizing the gain and linearity of the PMT. The energy resolution measurement is carried out by exciting the scintillator with a flux of electrons of precisely known energy and then analyzing the resulting distribution. The mono-chromatic source of electrons should approximate the delta function and therefore any smearing of the energy distribution is due to the calorimeter resolution. The gain of the PMT is characterized by the single photo-electron (SPE) method [123, 124] and the linearity is measured through the process of increasing the intensity of light incident on the photo-cathode and observing a change of the total charge of the signal.

11.1 The mono-chromatic electron source

Two methods are discussed in this section. The $^{207}\mathrm{Bi}$ method uses the conversion electrons of precisely known energy to measure the resolution of the calorimeter. This method is cheap and simplistic but requires a relatively more complicated method for extracting the energy resolution due to the large γ background. The $^{90}\mathrm{Sr}$ method uses an energy calibrated beam of β's to measure the resolution of the calorimeter. Extraction of the energy resolution is straight forward but the setup is complicated, expensive, and relatively bulky. Both techniques of measuring energy resolution were cross-checked against each other with identical calorimeter blocks and were found consistent within experimental errors (Sec. 12.6). The primary interest is to verify the parametrized fit (Sec. 11.4) used to extract the energy resolution from the measured $^{207}\mathrm{Bi}$ energy spectra. The $^{207}\mathrm{Bi}$ technique is used to obtain the values presented in this

paper except where specified differently.

11.1.1 The ^{207}Bi technique

^{207}Bi decays via electron capture (Sec. 3.1) to an excited nuclear state of ^{207}Pb. The de-excitation γ 's have a relatively high conversion efficiency of $\sim 7\%$. An overlap of the electron and nuclear wave functions corresponds to a small probability for the electron to be found within the nucleus. The emission of a conversion electron is a process which instead of nuclear de-excitation via γ emission, the energy is transferred to a shell electron resulting in ejection from the atom.

The mono-chromatic source of electrons is produced by the K-shell 976 keV conversion electrons (CE) from ^{207}Bi decay. This is the cheapest and most simple solution, but the drawback to this method is fitting the convolution of additional x-rays, γ-rays, L-shell and M-shell conversion electrons. The decay scheme is similar to the descrip-

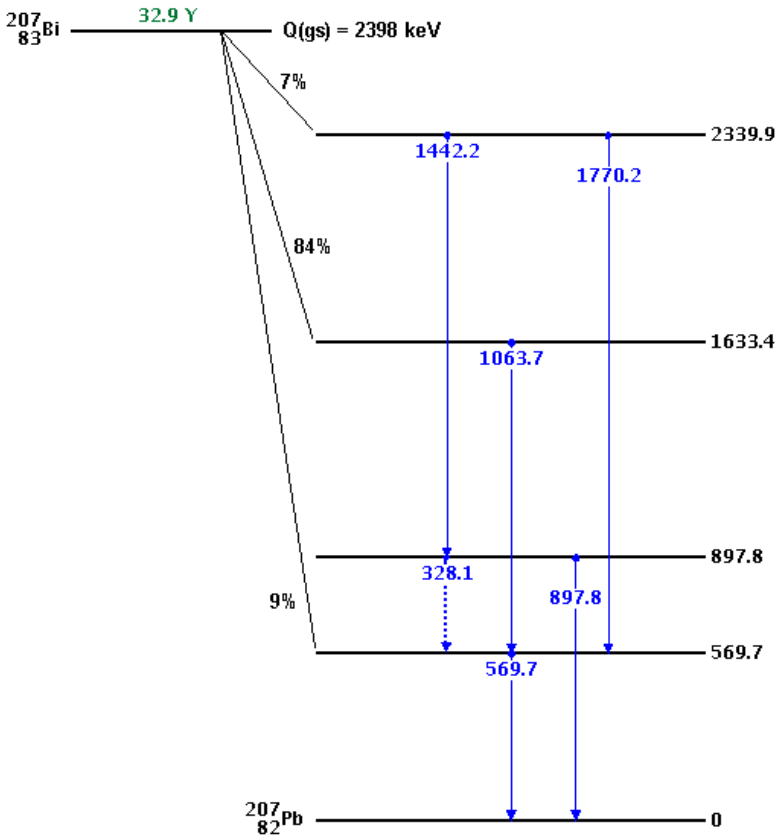

Figure 11.1: Decay scheme for ^{207}Bi showing the excited states of ^{207}Pb and the corresponding de-excitation transitions.

tion in Sec. 7.1.1. The crucial difference is that the gamma transitions indicated here in

BLUE can manifest as conversion electrons. The electron wave-function overlaps that of the nucleus and therefore gives the excited nucleus some probability to transfer energy directly to the electron. Simultaneous detection of two or more particles/photons is an effect known as pile-up. At least one coincident γ-ray is associated with the conversion electron emission (see decay scheme Fig. 11.1), and as the test scintillator occupancy of the solid angle of the isotropic $^{207}\mathrm{Bi}$ emissions increases, the probability for pile-up of the conversion electron and γ-ray increases. Edge effects are so-called because the electron can pass through the edge of the scintillator depositing a fraction of its energy effectively increasing the variance of the deposited energy. Electron energy loss through ionization of the air and reflective material (following the Landau distribution) contributes to the smearing of the energy spectrum thereby worsening the measured energy resolution. Pile-up, edge effects and energy loss are not intrinsic to the calorimeter block, but do affect the experimentally measured energy resolution. Special consideration must therefore be given to these factors. An analytical method is used to extract the energy resolution of the test block from the measured energy and variance of the 976 keV K-shell conversion electron.

11.1.2 The $^{90}\mathrm{Sr}$ technique

Calorimeter R&D done in parallel at CENBG (Centre d' Etudes Nucléaires de Bordeaux Gradignan) focuses on the use of Photonis PMTs (Sec. 10.5). CENBG uses a different technique to achieving a mono-chromatic electron source. Referred to as a test-beam, electrons from the continuous $^{90}\mathrm{Sr}$ β-decay energy spectrum are selected by momentum via magnetic field. The test-beam injects a flow of electrons into the calorimeter block at a user-defined energy. The test-beam has a dynamic range 0.4-2.0 MeV limited by β-decay statistics at low and high energies and an injection energy precision of $\pm 1\%$ due to the resolution of the silicon detector used for the calibration and the physical diameter of the beam aperture.

11.2 The data collection electronics

Two standards are used for the data acquisition. The signal discrimination and logic electronics run under the NIM standard and the charge integration and computer communications electronics are on the VME standard. At the heart of the acquisition

electronics is the gated charge integration to digital converter (QDC). An 8 channel, 12-bit QDC model V965A manufactured by CAEN is used. The QDC integrates the signal in two charge resolutions simultaneously. The high resolution mode has a LSB (least significant bit) of 25 fC (femto Coulombs) and dynamic range $\sim$95 pC, and the low resolution mode has 200 fC LSB and dynamic range $\sim$760 pC (bins $>$3800 are overflow).

There are two modes of operation for the data acquisition stack. The gain and linearity (and pedestal) measurements use the pulse generator to drive the LED and also generate the gate for the QDC integration window. During the energy resolution measurements the PMT signal is passively split in half between the electronics generating the gate for charge integration and the QDC (Fig. 11.2). The source of the initial signal

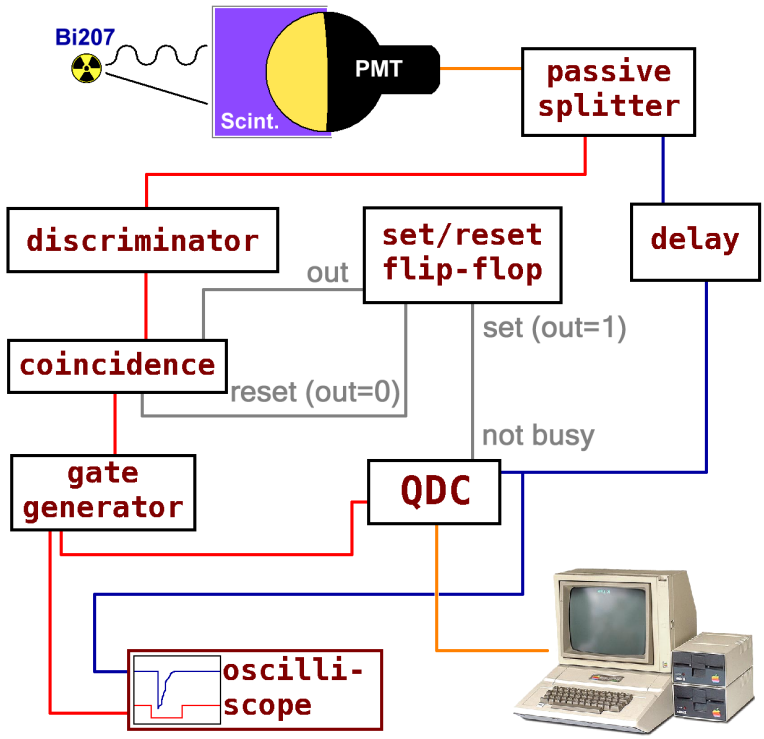

Figure 11.2: Block diagram of the ^{207}Bi data acquisition setup. The BLUE path represents the unaltered signal, the RED path depicts the logic circuitry, and the GREY path shows the set-reset flip-flop loop.

which is triggering the electronics is the only difference between the two modes as the following chain of events is identical in both systems. The triggering signal must be in coincidence with the QDC's *NOT BUSY* logic which then generates a *TRUE* logic

pulse from the coincidence unit. Successful coincidence activates the gate generating unit (CAEN 2255A) which creates an output pulse with predefined width which then becomes the integration gate for the QDC. A set/reset flip-flop unit (CERN N7337) interprets the *BUSY* or *NOT BUSY* signals from the QDC to provide the coincidence unit with the appropriate logic signal. This was needed to add flexibility to the test bench as QDC *BUSY / NOT BUSY* logic is manufacture dependent (for example CAMAC and VME standards).

11.3 Characterization of the PMTs

ETL is still developing their high QE technology, therefore the 8" Hamamatsu R5912-MOD PMT is our leading candidate for SuperNEMO. Characterization of the 8" Hamamatsu R5912-MOD was necessary to maintain discussions with Hamamatsu regarding the linearity and timing R&D. Measuring the PMT gain with the 1^{st}-PE method (Sec. 11.3.1) allows for the first dynode correction factor to be measured which must be known to make an accurate linearity measurement (Sec. 11.3.2). In the case of NEMO-3 and SuperNEMO where the precision of the main analysis depends on the precision of the energy distribution, it is best to ensure the linearity of the PMT past the $Q_{\beta\beta}$ of the source.

11.3.1 PMT gain measurement

Discussions with Hamamatsu lead to an 8-dynode chain implementation of the 8" R5912-MOD (typically it has 10-dynodes). The 8-dynode chain should have faster timing and better linearity at the sacrifice of lower gain. The gain g_i between two dynodes d_i and d_{i-1} is proportional to their voltage difference times the secondary emission coefficient δ_i

$$g_i = \varepsilon_{i-1}\delta_i\varepsilon_i V_i^{\alpha}\,, \tag{11.3.1}$$

where ε_i and ε_{i-1} are the collection efficiencies of d_i and d_{i-1} and the constant α is usually between 0.6 and 0.8.

The absolute PMT gain G_{PMT} is estimated using the pedestal-subtracted first photo-electron peak position in QDC bins (1PE_{QDC})

$$G_{PMT} = (1\text{PE} - \text{ped})_{QDC}\left(\frac{\text{QDC}_{\text{LSB}}\,(\text{C})}{e^-_{\text{charge}}\,(C)}\right)\,, \tag{11.3.2}$$

where ped_{QDC} is the pedestal position in QDC bins. QDC_{LSB} is needed to transform the QDC bin value into a charge. This is a precise method but in this particular case a 40x amplifier is needed to achieve pedestal to 1^{st}-PE peak separation and the gain of the amplifier is only known to $\pm 5\%$. The analytical parametrization described in Ref. [124] is used to fit the energy spectrum. A typical 1^{st}-PE plot and fit to data for the 8" Hamamatsu R5912-MOD at 1900 V is shown in Fig. 11.3. The first peak at bin

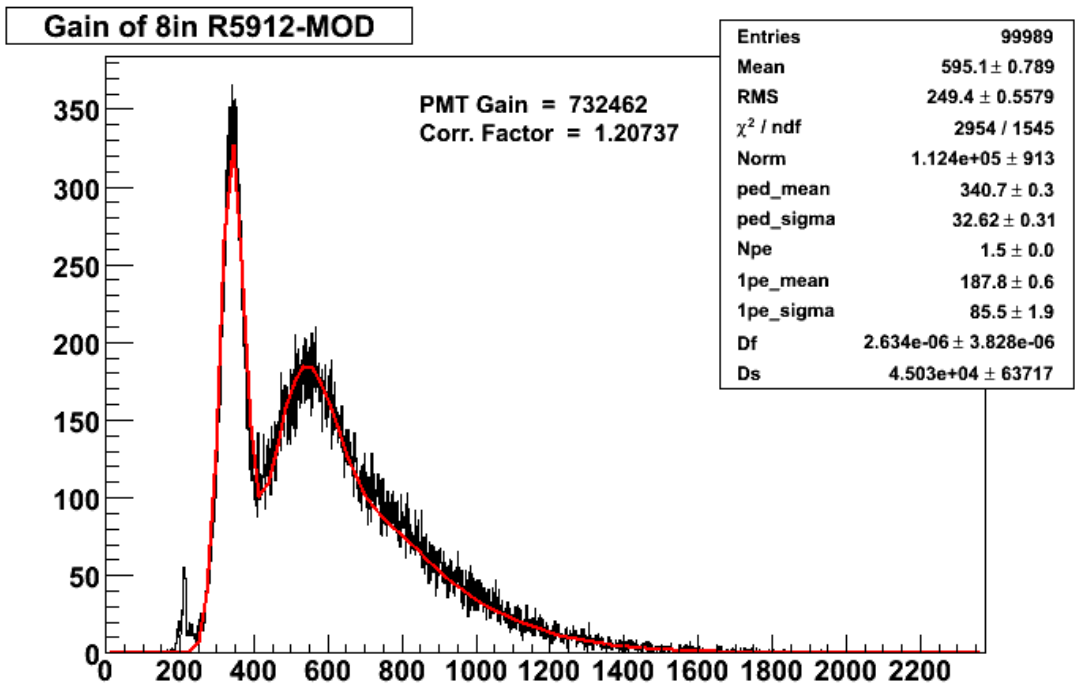

Figure 11.3: Typical 1^{st}-PE spectrum for the 8" Hamamatsu R5912-MOD PMT at 1900 V. The RED line is the fit to data. The correction factor is discussed in Sec. 11.3.2.

340 is the pedestal, the second peak at bin 550 is the 1^{st}-PE, and the large tail of the spectrum is the sum of higher order overlapping photo-electron peaks.

The PMT gain as a function of voltage $G(V)$ is expressed

$$G(V) = \prod_{n=1}^{N} k_i V_i^{\alpha} = k V^{\alpha N}\,, \tag{11.3.3}$$

where k is a constant, V is the high voltage and N is the total number of dynodes. The Eq. 11.3.3 power law is fit to data as shown in Fig. 11.4 providing a characteristic gain curve of the PMT. The measured gain is consistent with Hamamatsu's expectation of a few $\times 10^5$. An operating voltage of 1900 V was chosen to achieve a gain of

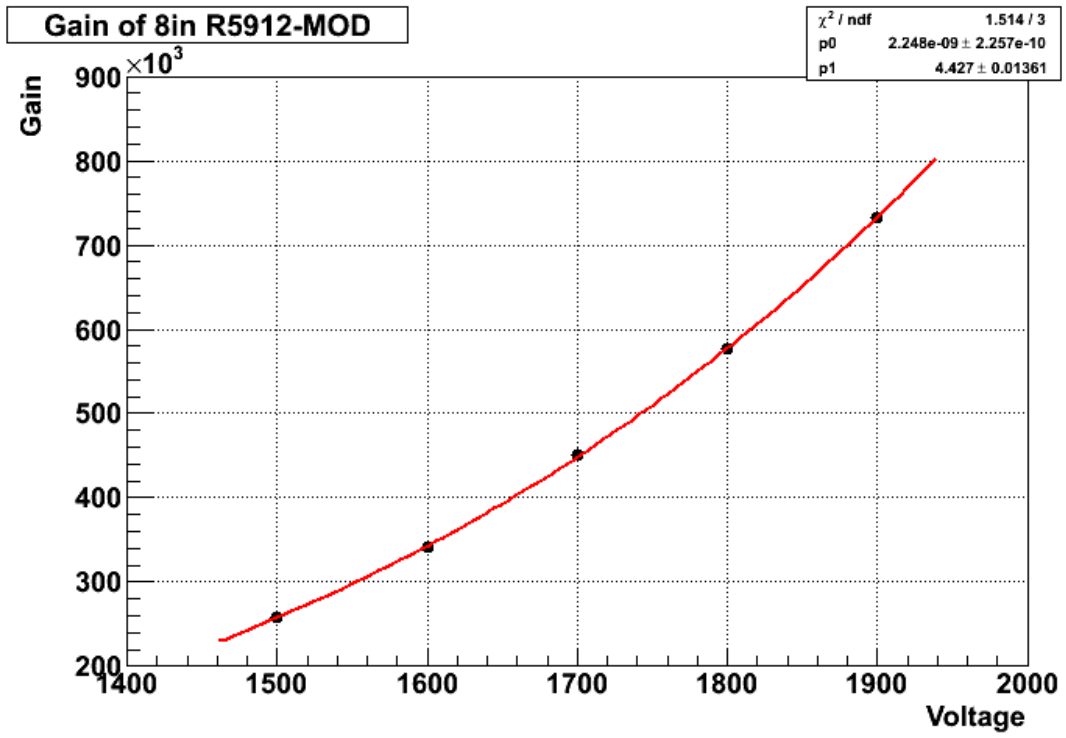

Figure 11.4: Gain curve for the 8" Hamamatsu R5912-MOD PMT at 1500-1900 volts.

$\sim 7 \times 10^5$ while maintaining a safety margin from the 2000 V maximum specified by Hamamatsu.

11.3.2 PMT linearity measurement

Ideally the ratio between the incident light and anode current should remain constant. In reality this relationship deviates from linearity with increasing light. Cathode and anode characteristics contribute to the overall linearity of the PMT. The photocathode is a semiconductor and the photo-electric conversion efficiency behaves non-linearly at high light intensities. The cathode to first dynode collection efficiency displays non-linear behavior at large currents but is suppressed by maintaining a higher voltage of 100-300 V between the cathode and first dynode to reduce space-charge effects.

The anode linearity is limited by space charge effects due to a large current flow between dynodes. The linearity can be improved with a special voltage divider circuit called the "tapered" voltage divider designed to increase the voltage between the latter dynode stages. Capacitors are also added to the latter dynode stages to compensate the effect of large anode currents on the voltage divider.

Motivation for the 8-dynode chain is increased linearity due to suppressed space charge effects and fast timing. A schematic of the resistor chain used for the 8” Hamamatsu R5912-MOD is Fig. 11.5. The above solutions are implemented into the voltage

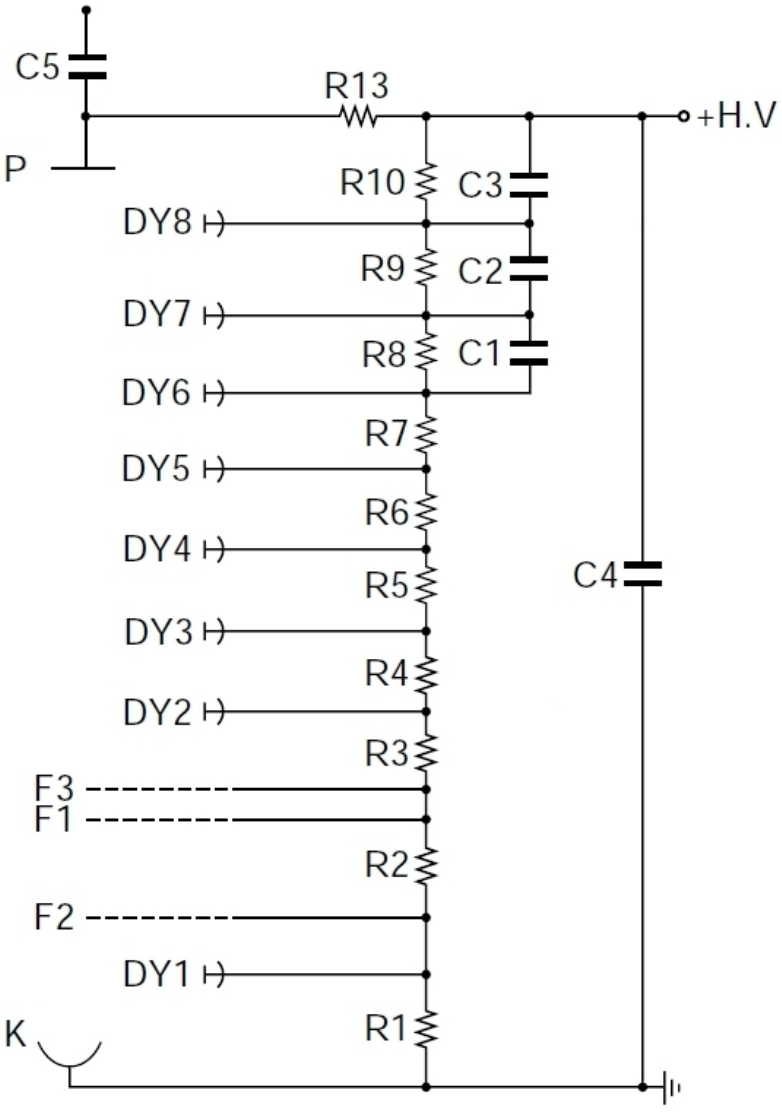

Electrodes	K	Dy1	F2	F1	F3	Dy2	Dy3	Dy4	Dy5	Dy6	Dy7	Dy8	P
Ratio	11.3	0	0.6	0	3.4	5	3.3	2	2.5	3.5	4.8	4	
Capacitors in uF										0.01	0.01	0.01	

K : Cathode, Dy : Dynode, P : Anode, F : Focus

Figure 11.5: Electronic schematic of the voltage divider and resistor ratios for the Hamamatsu ZQ0030 type base. This base is designed for improved linearity (Fig. 11.7) and positive high voltage.

divider. A large resistive ratio between the photocathode and first dynode provides a large voltage difference. The last four dynodes have an increasing resistive ratio to

suppress space charge effects and the last three dynodes have capacitors to compensate the effect of large anode currents.

Linearity measurements were obtained using a calibrated light injection system. Neutral density (ND) filters were used to attenuate light from a stabilized LED source. The motivation behind using the ND filters was to suppress any non-linear effects from the LED and power supply. The number of photo-electrons (N_{pe}) is approximated by (assuming $N_{pe} > 20$)

$$N_{pe} \approx \left(\frac{\mu}{\sigma}\right)^2 , \tag{11.3.4}$$

where μ and σ are the pedestal subtracted mean and sigma of the Gaussian distribution. This approximation always underestimates the true N_{pe} due to stochastic dynode fluctuations and is corrected by the factor $f_{\rm pmt}$ which is experimentally extracted from the 1^{st}-PE fit (Fig. 11.3)

$$N_{pe} = \left(\frac{\mu}{\sigma}\right)^2 \times f_{\rm pmt} , \tag{11.3.5}$$

where

$$f_{\rm pmt} = 1 + \frac{1}{g_1} + \frac{1}{g_1\, g_2} + \frac{1}{g_1\, g_2\, g_3} + ... \frac{1}{g_1 \cdots g_n} , \tag{11.3.6}$$

The N_{pe} correction factor is generally truncated to

$$f_{\rm pmt} = 1 + \frac{1}{g_1} , \tag{11.3.7}$$

and

$$g_1 \approx \left(\frac{\mu_1}{\sigma_1}\right)^2 , \tag{11.3.8}$$

where μ_1 and σ_1 are the pedestal subtracted mean and sigma of the 1^{st}-PE peak. Typical values of $f_{\rm pmt}$ range between 1.1 and 1.5, and for the 8" Hamamatsu R5912-MOD operating at 1900 V the $f_{\rm pmt} = 1.21$ (see "Corr. Factor" displayed at the top-center of Fig. 11.3).

We are interested in the linearity as a function of energy so we assume 1000 pe to equal 1 MeV because from Eq. 10.1.1 1000 pe corresponds to an energy resolution of $\sim 7\%$ FWHM at 1 MeV. The linearity is measured by plotting the pedestal subtracted mean of the QDC histogram ($\text{QDC}_{mean-ped}$) verses the calculated N_{pe} and observing the deviation from a linear fit. Characterization of the 8" Hamamatsu R5912-MOD at a voltage of 1900 V (Fig. 11.6) shows less than 1% deviation from linearity at $\sim 3700\ N_{pe}$ (~ 3.7 MeV). The current of a pulse is estimated by

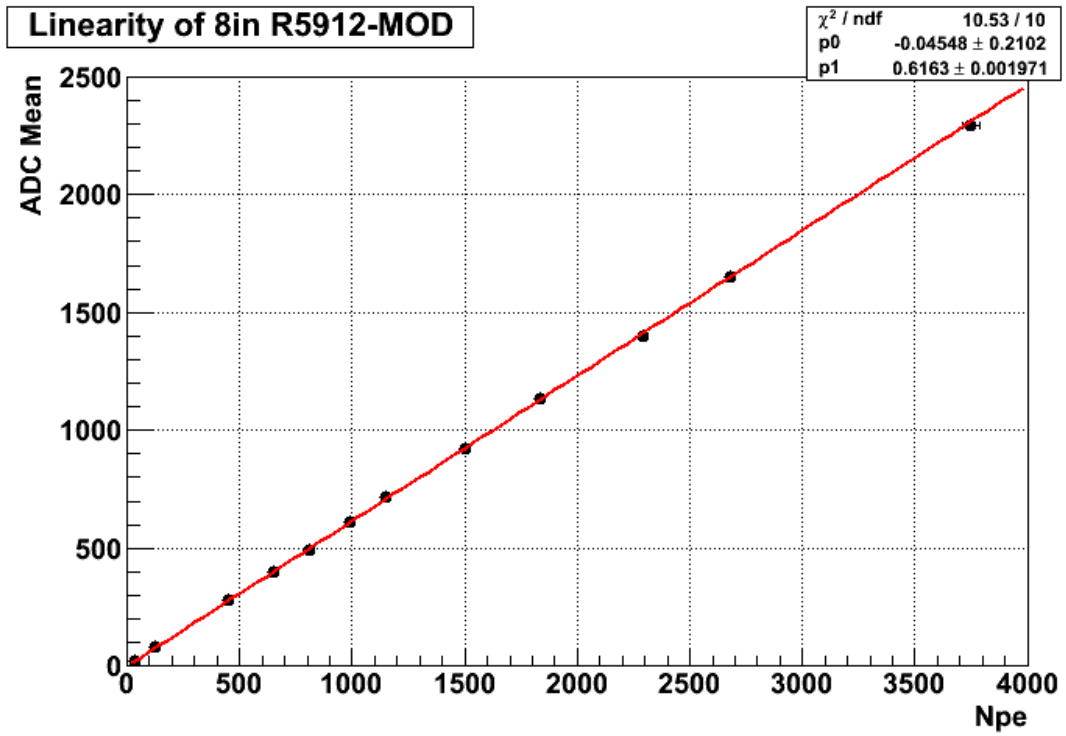

Figure 11.6: Linearity measurement of the 8" Hamamatsu R5912-MOD at 1900 volts shows less than 1% deviation from linearity at $\sim 3700\ N_{pe}$ calculated by Eq. 11.3.5 and using the correction $f_{\text{pmt}} = 1.21$.

$$\text{current}\,(\mu A) = (\text{mean} - \text{ped})_{QDC} \left(\frac{QDC_{\text{LSB}}\,(fC)}{\text{time}_{FWHM}\,(ns)} \right) , \tag{11.3.9}$$

where the time$_{FWHM}$ is the full width at half the maximum of the incident light source pulse assuming the rise time and decay time are similar. A QDC mean of 2300 bins (200 fC/bin) and a pulse time$_{FWHM}$ of 10 ns produces an average current of 46 mA. The obtained value is consistent with Hamamatsu expectations as shown in Fig. 11.7.

11.4 Parametrization of the ^{207}Bi energy spectrum

The parametrization is an analytical method in which a function is "fit" to the shape and normalization of ^{207}Bi energy spectra. The energy resolution measurement requires three separate data acquisitions. Data runs must be taken to obtain a pedestal, an energy spectrum of the γ background (achieved by shielding out the electrons with 2 mm of aluminum) and the total energy spectrum of the γ's + CEs (conversion electrons). The mean of the pedestal run is required to subtract the QDC offset induced by the acquisition electronics and the sigma of the pedestal provides an estimation of

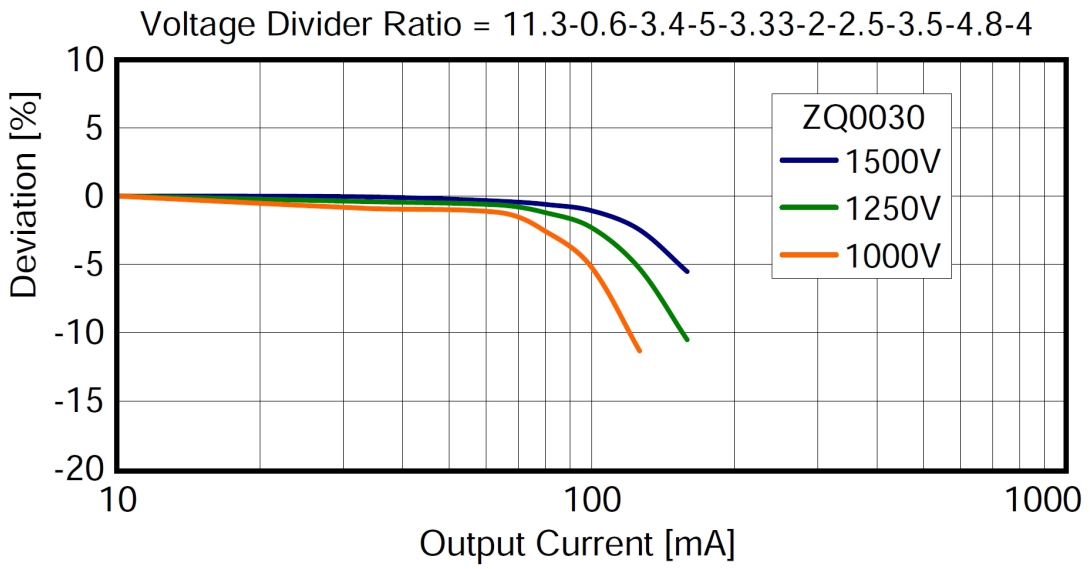

Figure 11.7: Deviation from linearity as a function of current for the 8" Hamamatsu R5912-MOD using the ZQ0030 type voltage divider at three voltages. At 1500 V a 1% deviation occurs at 90 mA.

the electronic noise. An energy spectrum of the γ background is required to fix certain parameters before fitting the γ + CE spectrum.

The Compton edges from the γ distribution are sufficiently described by a modified Heaviside step-function

$$\frac{1+e^{xP_1}}{1+e^{(x-P_2)/P_3}}\,, \tag{11.4.1}$$

where P_2 is the approximate energy of the experimental Compton edge and x notates the QDC bin number. P_1, P_2, and P_3 are free parameters of the function. The free parameters are determined using the γ-only data and then fixed for the fit to γ + CE data. The conversion electrons at 482 keV and 976 keV are each described by the sum of 3 Gaussian distributions due to the K, L, and M shell electrons of the transition. The Gaussian distribution is defined

$$G(\mu,\sigma) \equiv \frac{1}{\sigma\sqrt{2\pi}} \cdot e^{\left(\frac{-(x-\mu)^2}{2\sigma^2}\right)}\,, \tag{11.4.2}$$

where x notates the QDC bin number. To minimize the number of free parameters, the L and M shell Gaussian functions are set dependent on the K shell parameters. By assuming the number of photo-electrons per unit of deposited energy to be a linear relation, we can write

$$\frac{N_{pe}}{\mu} = \frac{N'_{pe}}{\mu'}\,, \tag{11.4.3}$$

and substitute μ^2/σ^2 for N_{pe} (from Eq. 11.3.4) on both sides to give

$$\frac{\mu}{\sigma^2} = \frac{\mu'}{\sigma'^2}\,. \tag{11.4.4}$$

We can define

$$\mu' = \mu + E\alpha\,, \tag{11.4.5}$$

where E is a real energy and α is the QDC calibration constant ($bins/energy$). Substitute Eq. 11.4.5 into Eq. 11.4.4 and solve for σ' to arrive at

$$\sigma' = \sigma\sqrt{1+\frac{E\alpha}{\mu}}\,. \tag{11.4.6}$$

Finally the K, L, and M shell convolution is given by

$$I_1 G\left(\mu_K, \sigma_K\right) + I_2 G\left(\mu_K + E_{KL}\alpha, \sigma_K\sqrt{1+\frac{E_{KL}\alpha}{\mu_K}}\right) + I_3 G\left(\mu_K + E_{KM}\alpha, \sigma_K\sqrt{1+\frac{E_{KM}\alpha}{\mu_K}}\right)\,, \tag{11.4.7}$$

where μ_K, σ_K, and α are free parameters of the fit and x notates the QDC bin number. μ_K and σ_K are the mean and sigma of the K-shell conversion electron, and E_{KL} and E_{KM} are the known energy differences between K-L and K-M shells [90]. I_1, I_2, and I_3 factors preceding the $G\left(\mu_K, \sigma_K\right)$ functions are the known transition intensities in percent (%) [90] and are tabulated in Tab. 11.1. For convenience I will refer

Table 11.1: Relative intensities of the 482 keV and 976 keV conversion electrons from Ref. [90].

Transition		Relative Intensity (%)
482 keV	K-shell	1.52
554 keV	L-shell	0.44
566 keV	M-shell	0.15
976 keV	K-shell	7.03
1048 keV	L-shell	1.84
1060 keV	M-shell	0.54

to Eq. 11.4.1 as the function $GC(keV)$ being dependent on the energy of the Compton

edge and I will refer to Eq. 11.4.7 as the function $CE(keV)$ being dependent on the energy of the K-shell conversion electron. Two Compton edges at approximately 500 keV and 1000 keV and two conversion electrons at 482 keV and 976 keV are required for an analytical description of the ^{207}Bi energy spectrum and written as

$$GC(500\,keV) + CE(482\,keV) + GC(1000\,keV) + CE(976\,keV)\,. \qquad (11.4.8)$$

11.5 Validation of the parametrized fit

In order to evaluate the systematic error, the parametrization is applied to simulated ^{207}Bi spectra. Monte Carlo energy spectra are created with the same software packages as described in Sec. 6.1. Events are generated for the ^{207}Bi decay with DECAY0 [91] and propagated through the geometry of the calorimeter. A simulated 2 mm aluminum filter is inserted or withdrawn between the ^{207}Bi source and scintillator to generate the needed γ run and γ + CE run (Sec. 11.4). Crucial parameters such as the scintillator dimensions and the distance of the ^{207}Bi source from the scintillator are user defined. The N_{pe} (and therefore energy resolution) of the simulated setup is also user defined and allows the analytical method to be validated on a range of energy resolutions. This is a feature of the simulation package because it bypasses the need for a detailed description of the optical properties of the scintillator and PMT, yet reproduces the physics of the ^{207}Bi events incident on the scintillator such as gamma interaction rates, edge effects, pile-up and Landau energy loss of the electrons. Two geometries are considered for simulations.

11.5.1 Small volume test geometry

A thin scintillator with small surface area more accurately tests the analytical description of the 976 keV CE because the gamma interaction rate and pile-up effects (Sec. 11.1) are suppressed by this geometry leading to a better signal to background ratio. The effects of the Landau energy loss upon the measured resolution are reduced by keeping the ^{207}Bi source close (6 cm) to the scintillator. A scintillator geometry of 5×5×2 cm allows ⌀3" PMTs to be tested while maintaining full cathode coverage of the scintillator's surface area. Surface areas smaller than this begin to be dominated by edge effects (Sec. 11.1). Simulated γ and γ + CE energy spectra at 7% FWHM at 1 MeV for a 5×5×2 cm geometry are shown in Fig. 11.8.

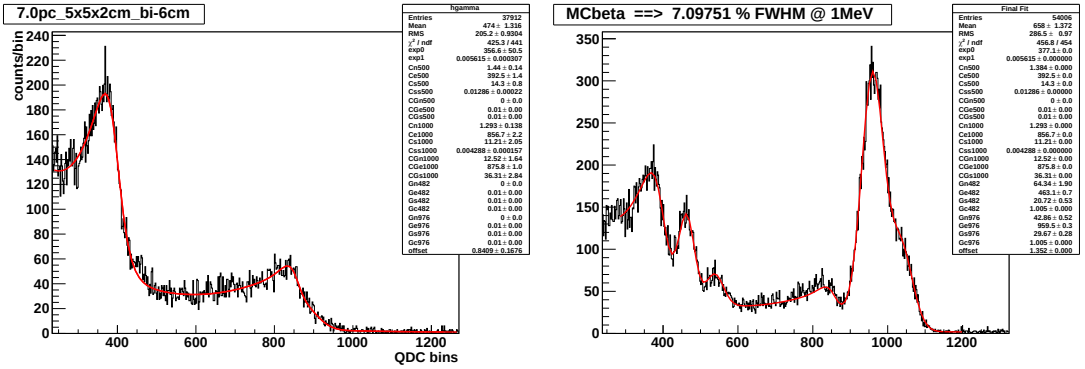

(a) energy spectrum of γ 's-only (b) energy spectrum of γ's + CEs

Figure 11.8: Simulated MC truth of 7% FWHM at 1 MeV for a $5\times5\times2$ cm scintillator geometry. Displayed are the γ energy spectrum (a) and the γ + CE energy spectrum (b) which are fit with the analytical method (red line).

Systematic error on the obtained energy resolution is evaluated through variation of initial parameters and parameter limits of the fit and the difference between the MC truth and reconstructed resolutions. An error of $\pm 0.3\%$ is observed when fluctuating the parameter limits and initial values. Differences between simulated and reconstructed resolutions are shown in Tab. 11.2 and have an average systematic of - 0.2% which ultimately becomes a correction to the measurements carried out on thin (2 cm) geometries.

11.5.2 Baseline design geometry

The SuperNEMO baseline design for the calorimeter is a hexagonal block spanning $\sim$25 cm across the surface and a minimum thickness of 10 cm. Optical simulations [117] and data (Sec. 12) have shown hexagonal geometries to produce better energy resolutions than square geometries and a 10 cm thickness is required for detecting γ-rays (Sec. 5.4). The hexagonal test block has a surface area of $\sim$400 cm^2 and an average thickness of $\sim$15 cm due to the concave cavity for coupling to the PMT. For convenience a square block with similar surface area and thickness ($20\times20\times15$ cm) is simulated. The ratio of the 976 keV CE peak height (QDC bin $\sim$950) to Compton edge peak height (QDC bin $\sim$850) in the γ + CE spectra demonstrates the increased γ detection efficiency for 15 cm thick simulation (Fig. 11.9) compared to the 2 cm thick simulation (Fig. 11.8). Multiple Compton scattering is evident in the γ-only spectrum

Table 11.2: Comparison of the simulated energy resolution (FWHM at 1 MeV) to the energy resolution extracted with the analytical method and extrapolated to 1 MeV for a 5×5×2 cm block. The energy resolution is extracted from the 976 keV CE.

MC Truth $\frac{\Delta E}{E}$ (%)	Reconstructed $\frac{\Delta E}{E}$ (%)	Difference
5.5	5.7	0.2
6.0	6.2	0.2
6.5	6.9	0.4
7.0	7.1	0.1
7.5	7.6	0.1
8.0	8.1	0.1
8.5	8.8	0.3
9.0	9.2	0.2

of Fig. 11.9 corresponding to the secondary "bumps" past the Compton edges at QDC bins ∼450 and 950.

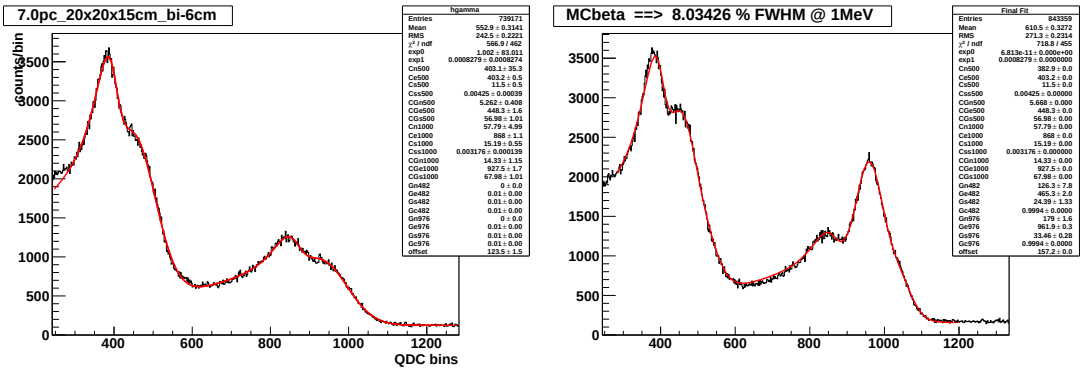

(a) energy spectrum of γ's-only (b) energy spectrum of γ's + CEs

Figure 11.9: Simulated MC truth of 7% FWHM at 1 MeV for a 20×20×15 cm scintillator geometry. Displayed are the γ-only energy spectrum (a) and the γ + CE energy spectrum (b) which are fit with the analytical method (red line).

The parametrization of multi-Compton bumps required a modification to Eq. 11.4.1.

The addition of a Gaussian distribution to Eq. 11.4.1

$$\frac{1+e^{xP_1}}{1+e^{(x-P_2)/P_3}} + G(P_4, P_5)\,, \tag{11.5.1}$$

was sufficient to accurately describe the γ-ray energy spectrum of the thick scintillator (Fig. 11.9). Free parameters P_4 and P_5 are the mean and sigma of a Gaussian distribution describing the multi-Compton bump.

The large γ background relative to $5\times5\times2$ cm block and the effects of pile-up increase the systematic error of the analytical method. As in Sec. 11.5.1 the error is estimated by comparing the known energy resolution of the simulated spectra with the obtained value from the analytical method (Tab. 11.3) and results show an average systematic of - 0.8% which ultimately becomes a correction to the measurements carried out on this geometry.

Table 11.3: Comparison of the simulated energy resolution (FWHM at 1 MeV) to the energy resolution extracted with the analytical method and extrapolated to 1 MeV for a $20\times20\times15$ cm block. The energy resolution is extracted from the 976 keV CE.

MC Truth $\frac{\Delta E}{E}$ (%)	Reconstructed $\frac{\Delta E}{E}$ (%)	Difference
5.5	6.4	0.9
6.0	7.0	1.0
6.5	7.4	0.9
7.0	8.0	1.0
7.5	8.4	0.9
8.0	9.1	1.1
8.5	9.6	1.1
9.0	10.0	1.0
9.5	10.6	1.1
10.0	10.8	0.8
11.0	12.1	1.1

11.6 Discussion and future ideas

The ^{207}Bi analytical parametrization describes the data well for small and large block geometries but has trouble accurately reconstructing the energy resolution for a large geometry. The three factors presumably most responsible for degrading the accuracy of the method are the simulated geometry approximation, multi-Compton scattering, and pile-up.

The fact that the hexagonal scintillator with a concave face is approximated by a square block with uniform thickness of 15 cm needs to be addressed. The physics of multi-Compton scattering is parametrized as Gaussian and pile-up is not described in the parametrization. Ultimately most of the uncertainty is due to the low signal to background of the 976 keV CEs. Another shortcoming of the analytical method is the need for two data runs which is very time consuming. A more preferable method would require only one data run of the γ's + CEs.

If the - 0.8% correction obtained from MC is taken into account, the energy resolution measurements for large blocks with the ^{207}Bi technique are reliable and consistent with the ^{90}Sr beam results as shown in Sec. 12.3.

11.6.1 Simulated geometry approximation

The hexagonal scintillator with a concave face (as seen in Fig. 12.6) is approximated in simulation by a square block with uniform thickness of 15 cm. The accuracy of the reconstructed energy resolution has dependence on the relative amplitude of the γ background. The difference between the γ interaction efficiencies of the real scintillator and simulated geometry is a source of error which can be resolved by simulating the full scintillator geometry. Simulations of the full geometry have been realized [125, 120] in GEANT-4.9, but the parametrization described in this paper has yet to applied to the updated geometry.

11.6.2 Multi-Compton scattering

The multi-Compton scattering is not described well and it is preferable to suppress all gamma events from the resolution measurement. In principle, this is accomplished by triggering the gated QDC (Sec. 11.2) only on electron events but this is technically challenging. Pulse shape discrimination is not an ideal choice because of the similarity between gamma and electron pulse shapes. Another approach uses a thin scintilla-

tor (100 μm) coupled to a PMT as the electron trigger (Fig. 11.10). The Hamamatsu

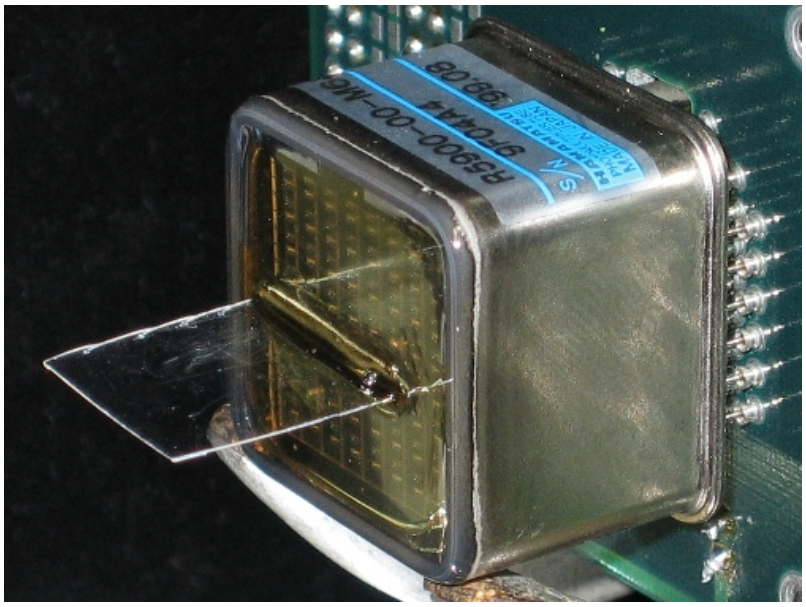

Figure 11.10: The 100 μm BC-404 scintillator is coupled to a 64 pixel Hamamatsu R5900-M64 to be used as an electron trigger.

R5900-M64 is the chosen PMT because of its small size, high collection efficiency ($>90\%$), and many pixels allows for sophisticated coincidence logic to suppress noise. The electron loses a small amount of energy (~ 10 keV) in the scintillator (BC-404) and the interaction probability for γ 's is small. There are a few downsides to this approach, for example the analytical fit must account for the Landau energy loss through the thin scintillator (and reflective wrapping and air) and the effects of pile-up still contribute to the measured energy resolution. Only one data run is required but a longer duration is required to gather sufficient statistics because of the reduced counting rate.

There was insufficient time to complete the electron trigger setup and analysis program for this paper. The parametrization of the Landau energy loss requires more development and simulations are needed to better understand the effects of the thin scintillator trigger, but this method shows potential as a simplistic alternative. The ^{207}Bi energy spectrum obtained from BC-404 $5\times5\times2$ cm scintillator coupled to the 3" Hamamatsu R6233-100 using the thin scintillator electron trigger and the analytical fit including Landau energy loss is shown in Fig. 11.11.

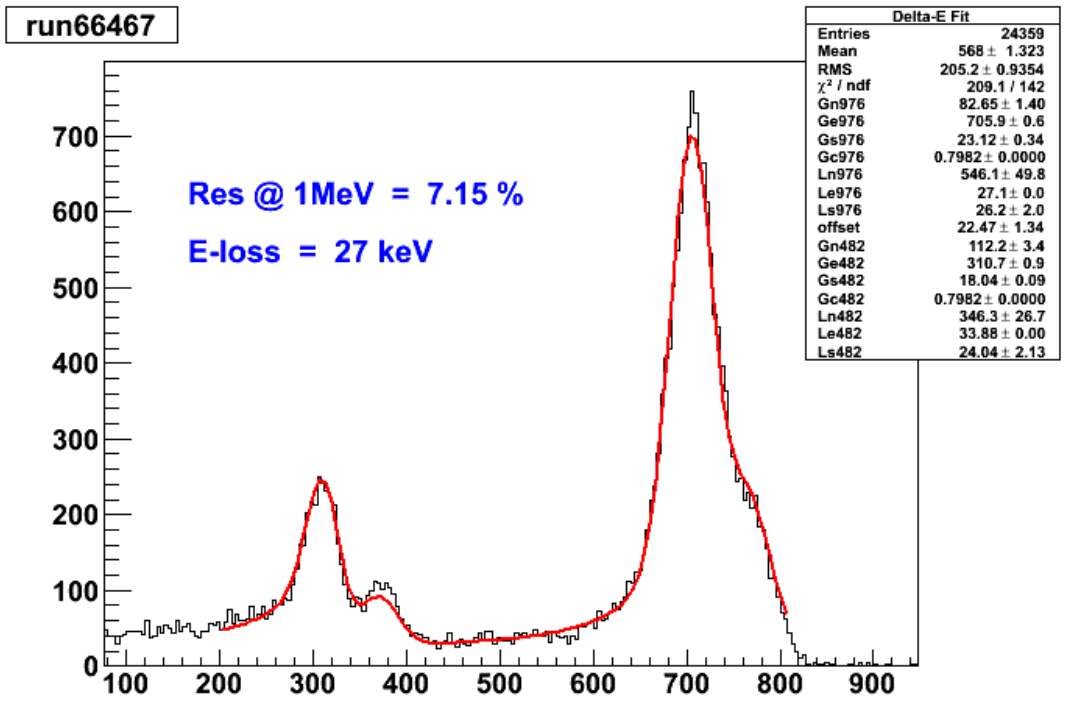

Figure 11.11: The energy spectrum of ^{207}Bi using the thin scintillator electron trigger and the analytical fit implementing the Landau energy loss.

11.6.3 Pile-up

Due to pile-up, the resolution measurements carried out on the test-bench are not representative of the block's intrinsic resolution. The effects of pile-up are complex and difficult to parametrize so a simpler method is needed. One possible solution is a numerical fit which would compare the data spectrum to pre-generated MC spectra using the Kolmogorov-Smirnov (K-S) test [126] or similar. The effects of pile-up (and multi-Compton scattering Sec. 11.6.2) are simulated into the MC spectra and would therefore not contribute to the measured energy resolution. Another advantage of the K-S method is the need for only one data run of the γ's + CEs.

Implementation of the K-S method was troublesome because of the sensitivity to differences in data and MC histograms. For example, the data and MC gamma efficiencies are slightly different and require time consuming fine-tuning to achieve the correct normalization. This means generating MC for many scintillator thicknesses until the gamma to CE peak height ratio of the MC matches that of the data and this procedure would have to be repeated for all new geometries being measured. More

development is needed towards the K-S method, which in principle will provide an accurate measurement of the intrinsic energy resolution without degradation from pile-up (or multi-Compton scattering Sec. 11.6.2).

Chapter 12

Energy resolution measurements

Many parameters of the calorimeter block were varied and measured. The different optical configurations tested are summarized in Tab. 12.1. Emission spectra of the

Table 12.1: Tested calorimeter block configurations.

Parameter	Tested Options	
Scintillators	Bicron, Eljen, PST	Tab. 10.1
Scintillator shape and size (cm)	$5\times5\times2$, $9\times9\times2$, $14\times14\times2$, $15\times15\times2$, $20^{hex}\times2$, $25^{hex}\times10$	
Reflectors	PTFE, Al. Mylar, ESR	Tab. 10.2
Optical couplings	Bicron, Cargille, Glycerol	Tab. 10.3
Photomultipliers	ETL, Hamamatsu, Photonis	Tab. 10.4
Lightguides	with lightguide, without lightguide, polished lightguide, abrased lightguide	
High voltage	dynamic range of PMT	

scintillators are needed to appropriately match with the PMT QE profile. Quoted emission spectra from Bicron are obtained via a thin scintillator reflection technique which suppresses the effects of bulk absorption. Independent measurements were carried out at UCL [127] to determine the effects of bulk absorption on the scintillator emission spectrum. A $5\times5\times2$ cm scintillator was excited with a 337 nm nitrogen LASER and an X-ray source. An optical fiber tunneled into the center of the scintillator (and optically epoxied) transferred the light to an Ocean Optics USB2000+UV-VS spectrometer with

dynamic range 200-850 nm. Measurements confirmed absorption at wavelengths below 400 nm. The measured spectra are shown in Fig. 12.1 and compared to the quoted emission spectra from Bicron.

Due to flexibility in the mechanical construction of the calorimeter, different possible configurations are tested. The use of PMTs < 5" is not feasible for the baseline design because of the many channels and high cost. The 5" PMTs have a flat cathode window and this generally leads to poor timing resolution because of the variation in drift time from cathode to 1^{st}-dynode. PMTs > 8" have hemispherical cathode glass and better timing resolution but QE uniformity and effects of an external magnetic field are a concern. Uniformity and magnetic effects become increasingly troublesome for larger PMTs and for this reason an 8" PMT is the baseline design.

The hemispherical cathode window of the large PMTs introduces new obstacles. A PMMA lightguide can be used to match the PMT cathode profile at one end and couple to a flat scintillator block at the other end. This is the standard approach for large PMTs and scintillators but had poor energy resolution due to the multiple optical coupling layers. Alternatively a large scintillator can be machined or cast to match the hemispherical profile of the PMT glass. The direct coupling of scintillators and PMTs of this size has not been done before and the required energy resolution was achieved with this new configuration. The measurements of the possible configurations are organized into 3 groups:

- **Configuration A** $\Longrightarrow$ PMTs ≤ 5" flat cathode window with the scintillator coupled directly to cathode window (Fig. 12.2-A)
- **Configuration B** $\Longrightarrow$ PMTs ≥ 8" hemispherical cathode window with the scintillator coupled to an intermediate lightguide which is coupled to cathode window (Fig. 12.2-B)
- **Configuration C** $\Longrightarrow$ PMTs ≥ 8" hemispherical cathode window with a concave scintillator coupled directly to cathode window (Fig. 12.2-C)

12.1 Configuration A

A comprehensive study is carried out with the 3" and 5" PMTs and $5\times5\times2$ cm scintillators to gain a better understanding of the factors influencing the energy resolu-

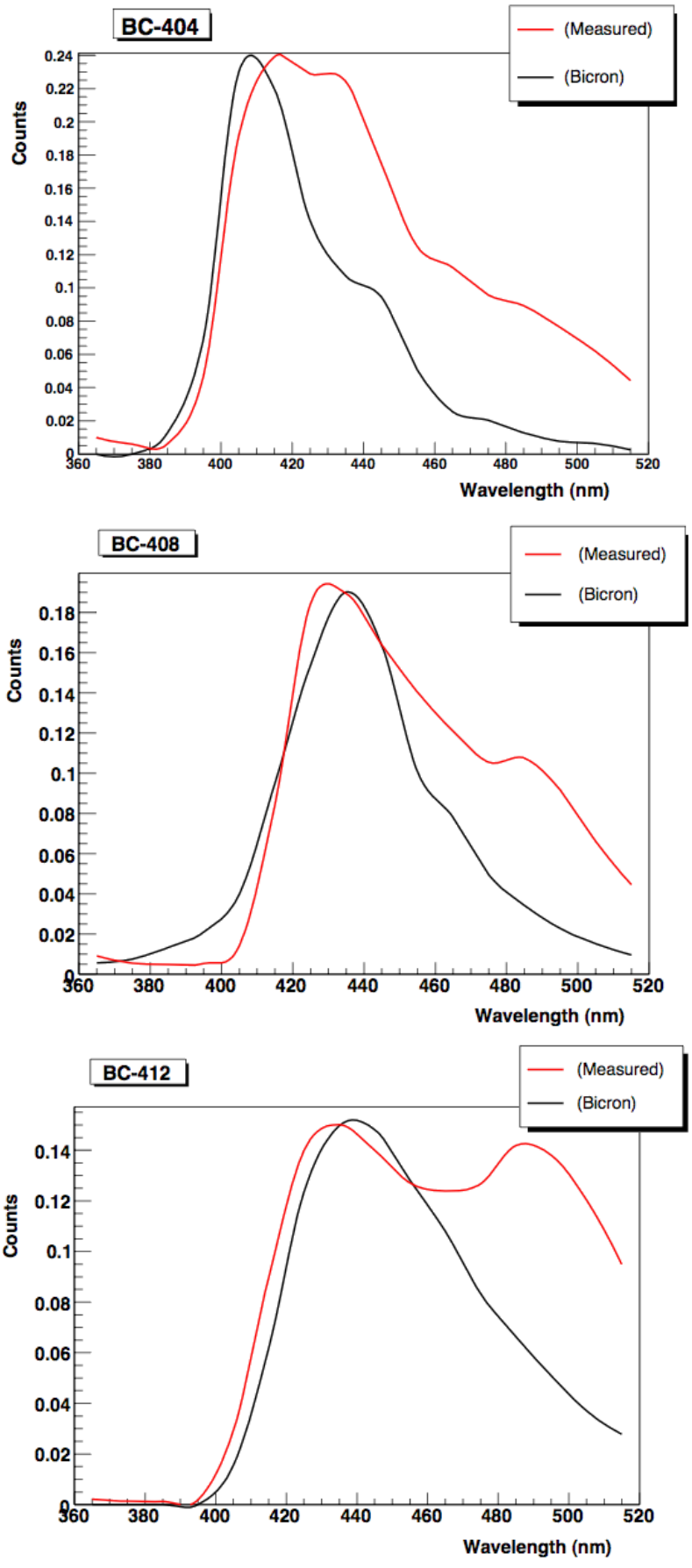

Figure 12.1: Measured emission spectra (red) compared to the quoted spectra from Bicron (black).

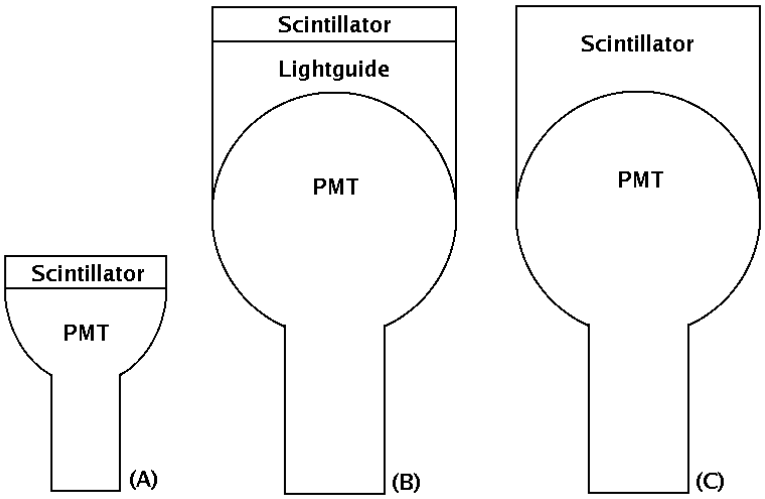

Figure 12.2: Three configurations under study.

tion. We need to verify that 7% FWHM at 1 MeV is achievable with a small scale setup because degradation of the resolution is expected with increasing size.

The best energy resolution to date was measured using Bicron BC-404 scintillator wrapped in Vikuiti ESR (Enhanced Specular Reflector) and coupled with BC-630 optical gel to a 3" Hamamatsu R6233-100 PMT. An energy resolution of 6.5% FWHM at 1 MeV was obtained (Fig. 12.3) which is better than the goal stipulated by the R&D. This is an unprecedented result for plastic scintillators.

The 3" Hamamatsu R6233-100-S has a max QE about 8% greater than the 3" Hamamatsu R6233-100 and we expect a better energy resolution from this PMT but we obtain a similar result. An intrinsic limitation of the 3" Hamamatsu R6233-100-S seems likely because other measurements [121] obtained with the 3" Hamamatsu R6233-100-S have been consistent with the 3" Hamamatsu R6233-100. The scintillators have suppressed light emissions below 400 nm, therefore one possible reason for similar performance of the 3" Hamamatsu R6233-100-S is the shift of the QE profile to shorter wavelengths (see Fig. 10.2). A summary of the obtained measurements is shown in Tab. 12.2.

The ETL D724KB PMT has a "green extended" photo-cathode meaning the QE extends further into the green wavelengths (Fig. 12.4). An ETL D724KB PMT coupled to a green extended Bicron BC-412 scintillator might have a better energy resolution than the standard 5" PMT setup, but presumably due to the decreased QE of the PMT

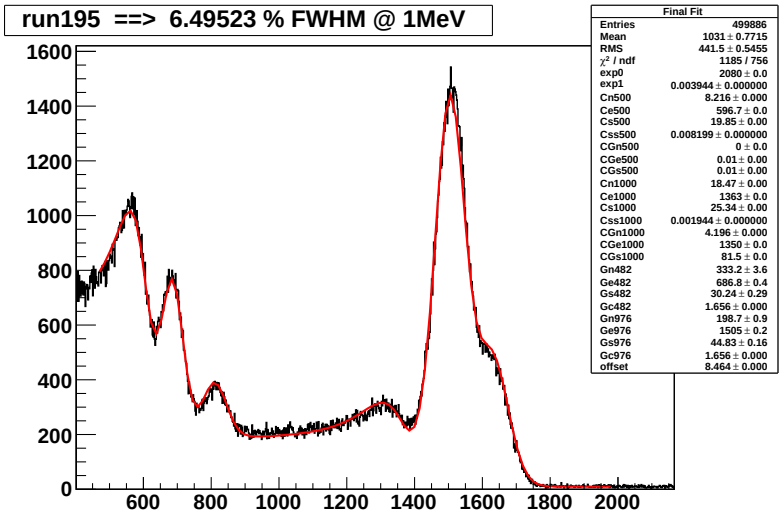

Figure 12.3: ^{207}Bi energy spectrum obtained with a 5×5×2 cm BC-404 scintillator wrapped in ESR, and coupled with BC-630 optical gel to a 3" Hamamatsu R6233-100 PMT. The fit to data returns a 6.5% FWHM at 1 MeV energy resolution.

Table 12.2: Results of measurements obtained with configuration A. The 0.2% offset found from simulation has not been subtracted and there is a ±0.2% error on the measurements.

	Scintillator			
PMT Size & Make	Type	Dim. (cm)	Refl.	$\frac{\Delta E}{E}$ (%)
3" Ham. R6233-MOD	BC-404	5×5×2	Vikuiti	6.5
3" Ham. R6233-MOD	BC-408	5×5×2	Vikuiti	6.7
3" Ham. R6233-MOD	BC-408	5×5×2	PTFE	6.7
3" Ham. R6233-MOD	BC-412	5×5×2	Vikuiti	6.7
3" Ham. R6233-MOD-S	BC-404	5×5×2	Vikuiti	6.8
5" ETL 9390KB	BC-408	5×5×2	PTFE	7.7
5" ETL D724KB	BC-404	5×5×2	Vikuiti	11.9
5" ETL D724KB	BC-408	5×5×2	PTFE	10.5
5" ETL D724KB	BC-412	5×5×2	Vikuiti	9.3

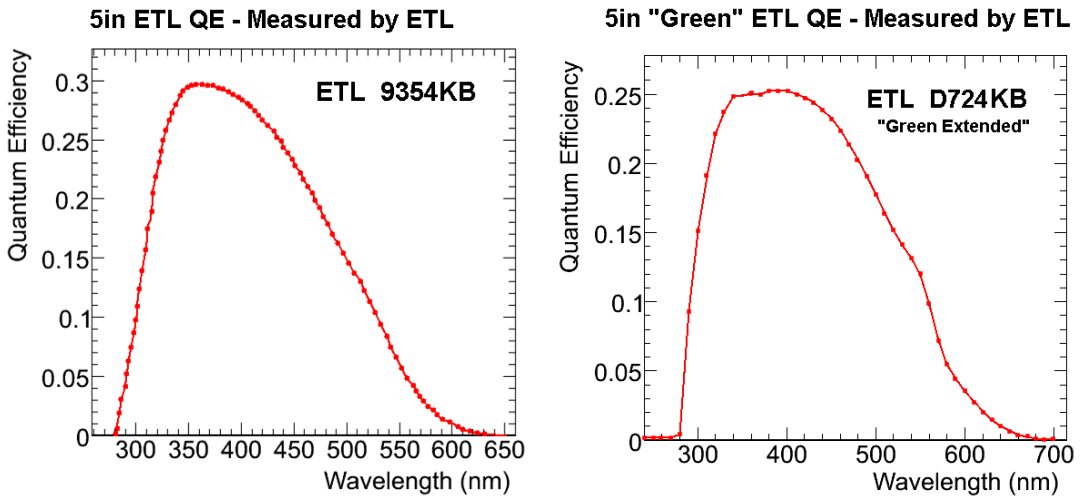

(a) standard ETL QE (b) green-extended ETL QE

Figure 12.4: A comparison of the QE profiles for the standard ETL PMT (a) and the green-extended PMT (b).

and decreased light yield of the scintillator, this was not the case.

12.2 Configuration B

Configuration B (Sec. 12) is motivated by the robustness of the PMMA lightguide and by using ≥ 8" PMTs the number of PMTs and electronic channels is reduced. Lightguides with a polished surface and abrased surface were used to study the effects of specular and diffusive internal reflection. PMT cathodes with diameter > 5" must be hemispherical to withstand vacuum (and minimize glass thickness) and the cylindrical lightguide must therefore have a concave end for coupling to the PMT. The PMT window (individually hand blown) is not a hemisphere with one radius but a convolution of 4-5 hemispheres of different radii and origin. Machining of the lightguide cavity was accomplished by choosing a large enough radius to envelope the PMT window, but the physical coupling of the lightguide to the PMT was problematic. Bicron BC-630 optical gel is too viscous and costly for the large volume between PMT and lightguide, so the optical coupling fluid type-06350 produced by Cargille was finally chosen. The results are categorized by PMT type. Note that the 0.2% correction associated with the thin (2 cm) scintillators (Sec. 11.5.1) is not applied to the measurements in the following tables. A summary of the obtained measurements for the $\oslash 8$" Electron Tubes Ltd.

(ETL) 9354KB PMT is shown in Tab. 12.3. A summary of the obtained measurements

Table 12.3: Measurements obtained with the ⌀ 8" ETL 9354KB PMT. The 0.2% offset found from simulation has not been subtracted and there is a $\pm 0.2\%$ error on the measurements.

Lightguide			Scintillator			
Finish	Side Refl.	Face Refl.	Type	Dim. (cm)	Refl.	$\frac{\Delta E}{E}$ (%)
abrased	Al-Mylar	Al-Mylar	BC-404	5×5×2	PTFE	10.4
abrased	PTFE	Al-Mylar	BC-404	5×5×2	PTFE	9.2
polished	none	none	BC-404	5×5×2	PTFE	11.0
polished	Al-Mylar	Al-Mylar	BC-404	5×5×2	PTFE	7.7
polished	PTFE	Al-Mylar	BC-404	5×5×2	PTFE	7.9
polished	PTFE	Al-Mylar	BC-404	5×5×2	Vikuiti	8.5
polished	PTFE	Al-Mylar	BC-404	14×14×2	Vikuiti	9.3

for the ⌀ 8" Hamamatsu R5912-MOD PMT is shown in Tab. 12.4. A summary of the obtained measurements for the ⌀ 11" ETL 9360KB PMT is shown in Tab. 12.5.

12.3 Configuration C

Configuration B was not able to achieve 7% FWHM at 1 MeV for realistic geometries. A machined or cast scintillator to couple directly to the PMT window is advantageous because of the increased active volume for γ detection and simple design (only one coupling layer) but PVT has a downside of not being very robust. PVT is very sensitive to chemicals and experiences aging effects which scale with exposed surface area, but these obstacles can be suppressed through careful preparation and handling of the scintillators. The main problem with this configuration is reliably producing the correct coupling shape but has proven to be feasible.

Special consideration is given to the baseline configuration of an 8" PMT coupled directly to a large hexagonal PVT scintillator. This setup achieves an unprecedented 7% FWHM at 1 MeV (Tab. 12.6) and is also promoted for its uniformity, reduced number of PMTs and electronic channels, relatively simplistic design, and background suppres-

Table 12.4: Measurements obtained with the ⌀ 8" Hamamatsu R5912-MOD PMT. The 0.2% offset found from simulation has not been subtracted and there is a $\pm 0.2\%$ error on the measurements.

Lightguide			Scintillator			
Finish	Side Refl.	Face Refl.	Type	Dim. (cm)	Refl.	$\frac{\Delta E}{E}$ (%)
polished	Al-Mylar	Al-Mylar	BC-408	9×9×2	Al-Mylar	11.3
polished	Al-Mylar	Al-Mylar	BC-404	14×14×2	Vikuiti	11.0
polished	Al-Mylar	Al-Mylar	BC-408	15×15×2	Al-Mylar	10.4
polished	PTFE	Al-Mylar	BC-404	5×5×2	Vikuiti	7.4
polished	PTFE	Al-Mylar	BC-404	14×14×2	Vikuiti	12.1
polished	ReflecTech	Al-Mylar	BC-404	5×5×2	Vikuiti	8.5
polished	ReflecTech	Al-Mylar	BC-408	$20^{(hex)}$×2	ReflecTech	10.9

Table 12.5: Measurements obtained with the ⌀ 11" ETL 9360KB PMT. The 0.2% offset found from simulation has not been subtracted and there is a $\pm 0.2\%$ error on the measurements.

Lightguide			Scintillator			
Finish	Side Refl.	Face Refl.	Type	Dim. (cm)	Refl.	$\frac{\Delta E}{E}$ (%)
abrased	Al-Mylar	Al-Mylar	BC-404	5×5×2	Vikuiti	10.4
abrased	Al-Mylar	Al-Mylar	BC-404	5×5×2	PTFE	10.2
polished	Al-Mylar	Al-Mylar	BC-404	5×5×2	Vikuiti	11.9

sion. The obtained energy spectra are seen in Fig. 12.5 using the Hamamatsu and Photonis PMT. Due to the systematic uncertainties in the analytical method used to extract the energy resolution, it was necessary to cross-check the measurements at CENBG using their calibrated mono-chromatic $^{90}\mathrm{Sr}$ electron beam (Sec. 11.1.2).

The following tabulated results (Tab. 12.6) were obtained using different PMTs but the scintillator sample is identical for all measurements. An Eljen type EJ-200 scintillator with hexagonal geometry measuring $25.5^{(hex)} \times 10$ cm is used (see technical specifications Fig. 12.6). Different optical coupling fluids and reflectors were tested and are specified with the energy resolution measurement. The extracted value from the analytical method is listed and the correction subtracted values obtained with the $^{207}\mathrm{Bi}$ and $^{90}\mathrm{Sr}$ methods are displayed. A picture of the EJ-200 scintillator coupled to

Table 12.6: Results of measurements obtained with a $25.5^{(hex)} \times 10$ cm EJ-200 scintillator in configuration C. The three PMTs tested are the 8" ETL 9354KB, 8" Hamamatsu R5912-MOD, and 8" Photonis XP1886-124 and XP1886-100. The - 0.8% correction has been applied to the measurements in the "Corr." column and there is a $\pm 0.3\%$ error on the measurements.

	Reflector				Corr. $\frac{\Delta E}{E}$	
PMT type	Side	Face	Coupling	$\frac{\Delta E}{E}$ (%)	$^{207}\mathrm{Bi}$	$^{90}\mathrm{Sr}$
9354KB	ReflecTech	ReflecTech	Glycerol	13.6	12.8	-
R5912-MOD	ReflecTech	Al-Mylar	Glycerol	8.0	7.2	7.6
R5912-MOD	PTFE	PTFE	Glycerol	8.1	7.3	7.8
R5912-MOD	PTFE	Al-Mylar	Glycerol	-	-	7.4
R5912-MOD	PTFE	Al-Mylar	Propanol	-	-	7.5
XP1886-124	ReflecTech	Al-Mylar	Glycerol	-	-	7.0
XP1886-124	PTFE	Al-Mylar	Glycerol	7.4	6.6	6.9
XP1886-124	PTFE	Al-Mylar	Propanol	-	-	7.1
XP1886-100	PTFE	Al-Mylar	Glycerol	-	-	7.2

the 8" Hamamatsu R5912-MOD is shown in Fig. 12.7.

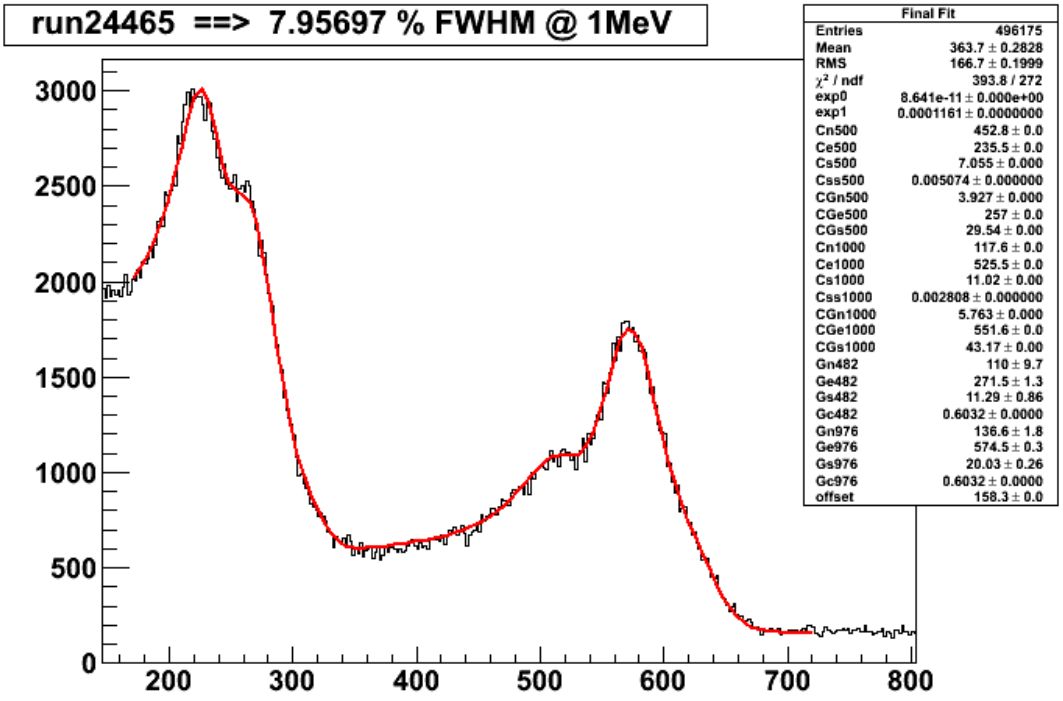

(a) $25.5^{(hex)} \times 10$ cm PVT scintillator coupled to a 8" Hamamatsu R5912-MOD

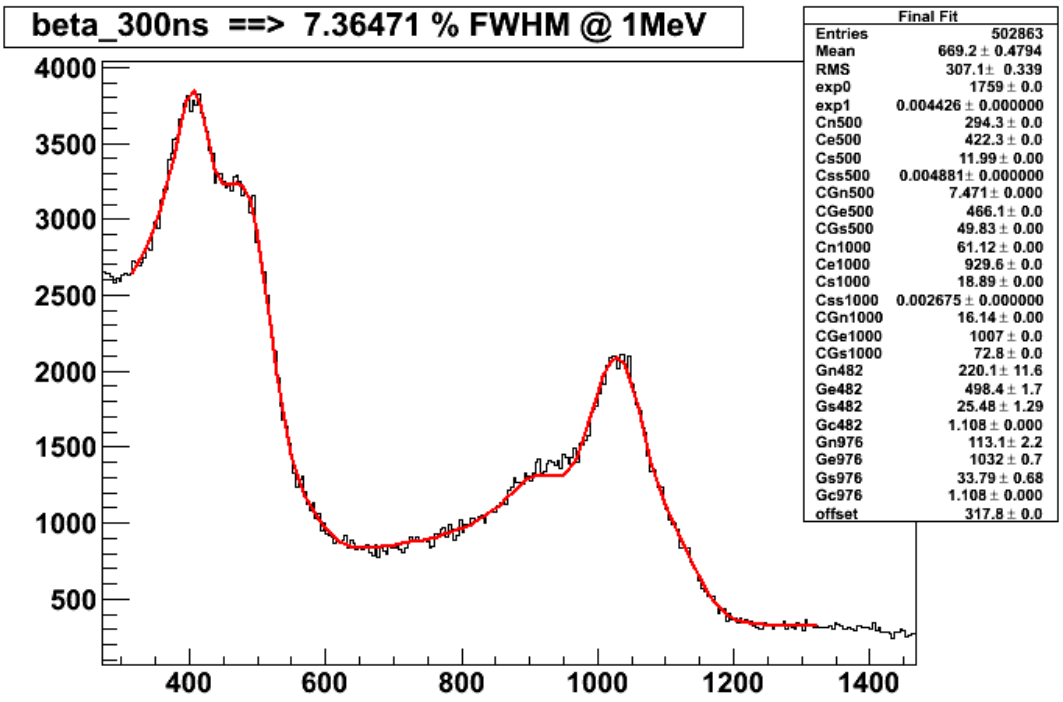

(b) $25.5^{(hex)} \times 10$ cm PVT scintillator coupled to a 8" Photonis XP1886-124

Figure 12.5: Unprecedented energy resolutions obtained for the $25.5^{(hex)} \times 10$ cm Eljen type EJ-200 PVT scintillator using 8" Hamamatsu and Photonis PMTs.

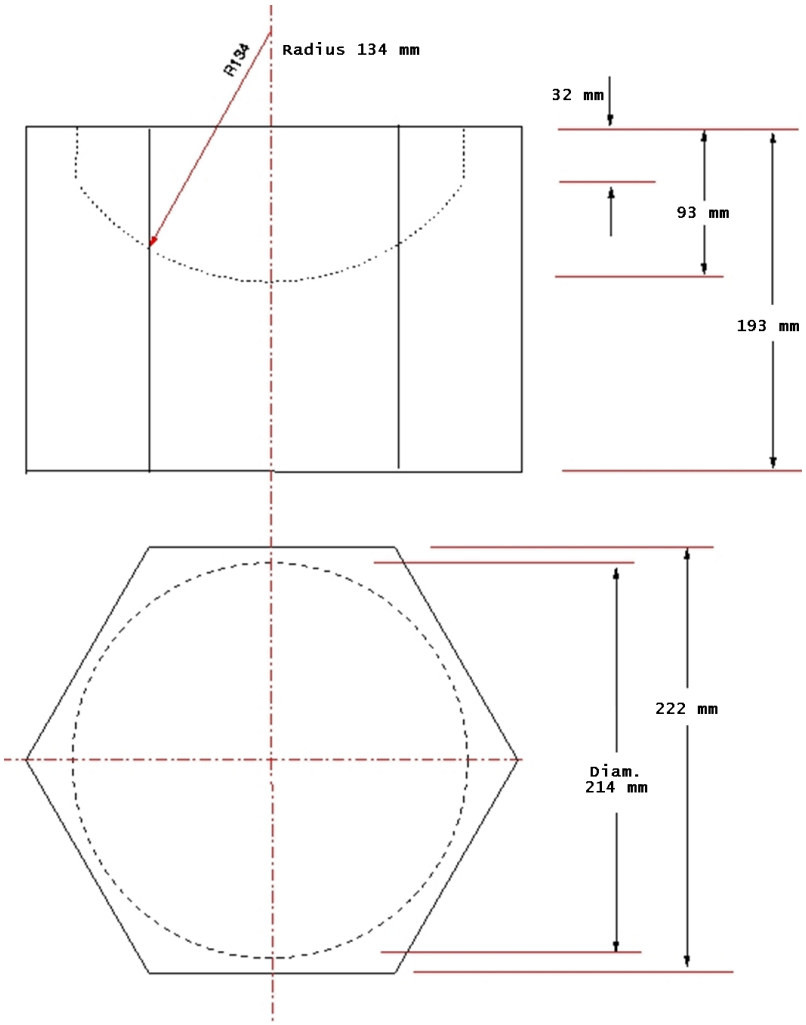

Figure 12.6: Technical specifications of the large hexagonal EJ-200 scintillator.

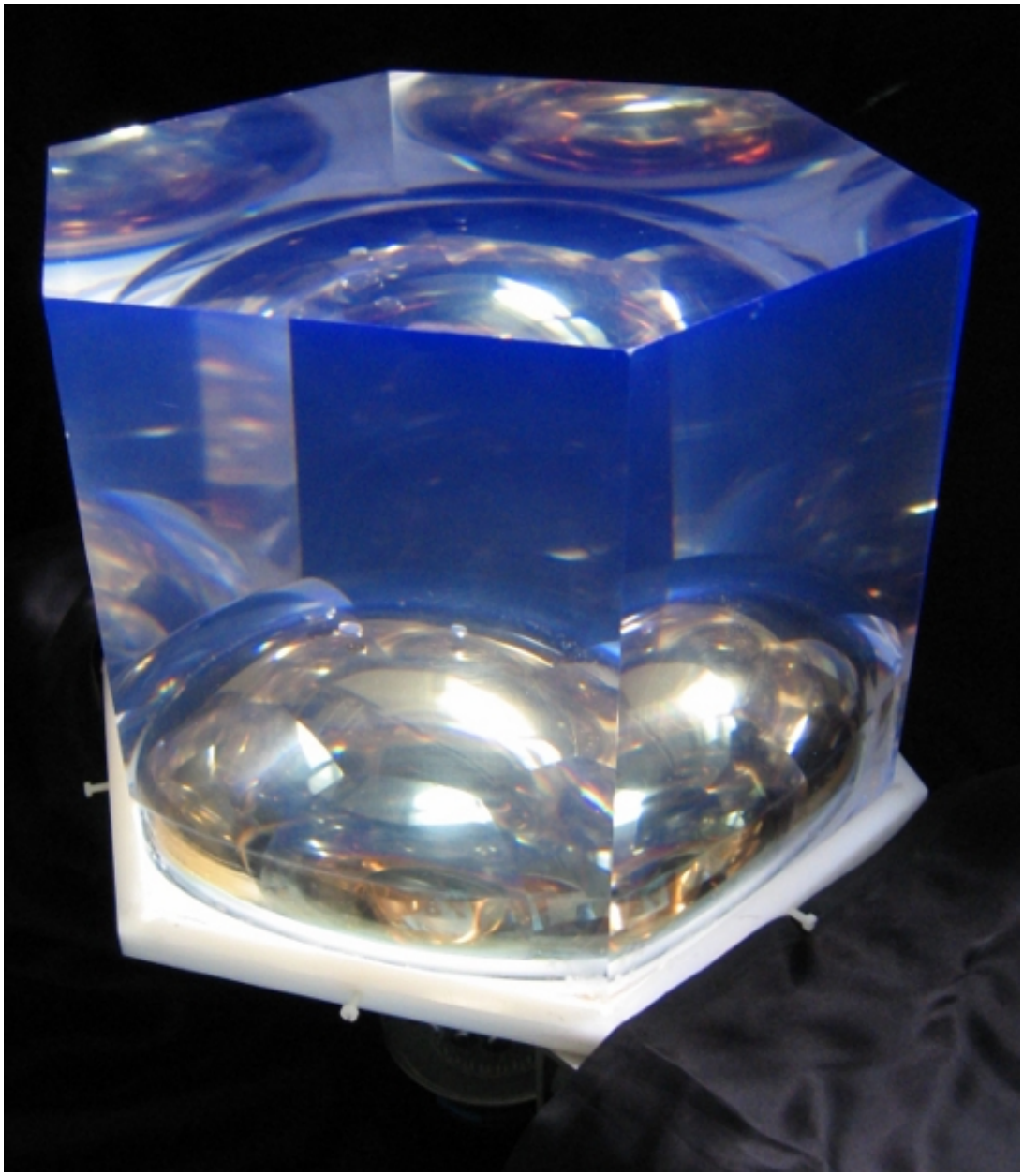

Figure 12.7: The EJ-200 scintillator coupled to the 8” Hamamatsu R5912-MOD.

An important observation from the Photonis PMT measurements is the improved performance over the Hamamatsu PMT. After-pulsing was observed in the 8" Photonis XP1886-124 and a previous study done at CENBG [120] displayed an effective QE similar to that of the XP1886-160. The XP1886-124 (with reduced QE) and the XP1886-100 both perform better than the Hamamatsu PMT. There are a few possible explanations for this behavior. The QE profile of the Hamamatsu PMT is shifted into the UV where there are no scintillator emissions, but the QE of the PMTs at the 400 nm point still suggests that the Hamamatsu should perform better (Fig. 12.8). The collec-

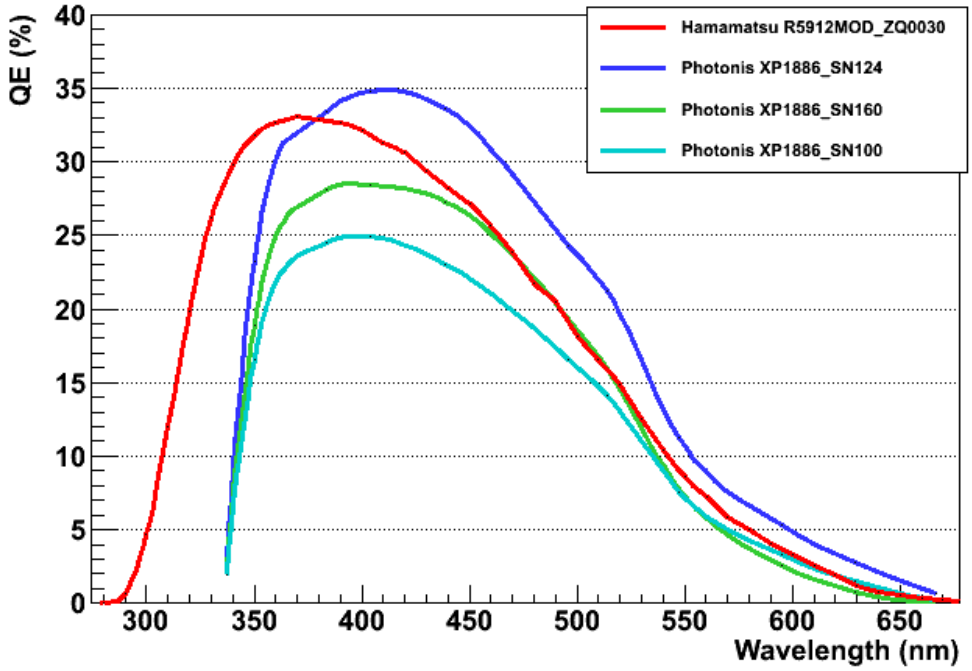

Figure 12.8: The QE profiles of the Hamamatsu and Photonis PMTs as a function of wavelength.

tion efficiency of the PMTs is not known and presumably the Photonis PMTs are more efficient. There has been a lot of discussion between us, Hamamatsu, and Photonis. The overall agreement is that although the QE spectra do play a role, the main reason for a better resolution from Photonis is due to their better collection efficiency and Hamamatsu will now be working on improving their collection efficiency. A previous study was done at CENBG [120] to optimize the voltage divider resistor values and the final divider was $\sim 0.5\%$ better than the standard. A combination of these effects explains why the Photonis PMTs perform better despite having a lower QE.

12.4 Summary and conclusions

Many options were considered for the SuperNEMO calorimeter (Tab. 12.1) including: Hamamatsu, ETL, and Photonis PMTs; mineral, liquid, PST and PVT scintillators; scintillator geometry; and different reflectors and optical couplings. Solid PVT scintillators coupled to large PMTs was chosen as the baseline design and this configuration was therefore the focus of this presented work.

The choice of the 8" Hamamatsu R5912-MOD corresponds to fewer PMTs and electronic channels and therefore lower cost than the 3" or 5" options, and uniformity and magnetic effects for the 8" are better than that of larger PMTs. The Eljen type EJ-200 scintillator is much cheaper than the Bicron BC-408 alternative and for mass production the scintillators will be cast with a concave end because this is cheaper and less time consuming than machining. The optical coupling will have to be the Stycast-1264 for structural integrability and the choice of reflective wrapping is yet to be determined.

The unprecedented target resolution for the baseline design of the SuperNEMO calorimeter has been achieved. It is unfortunate that Photonis has shut down their PMT production branch but the target resolution is still achieved with the Hamamatsu PMT. Additional work is underway to improve the Hamamatsu collection efficiency and radiopurity and the fine details of the mechanical design. The future release of the 8" UBA with 43% max QE, optimized voltage divider, and improved collection efficiency will provide even better energy resolutions in the range of 6.5 to 7.0% for this configuration.

Chapter 13

Conclusions

Neutrinoless double-beta decay is one of the most sensitive processes to determine the nature, absolute mass scale and mass hierarchy of the neutrino and will therefore have huge implications for particle physics, nuclear physics, astrophysics, and cosmology. The study of two neutrino double-beta decay gives us a better understanding of the nuclear models used to calculate the nuclear matrix elements, which are important to extract the new physics parameters from the neutrinoless double-beta decay search.

The NEMO-3 detector is located at the Laboratoire Souterrain de Modane (LSM) in the Fréjus road tunnel connecting France and Italy. The detector was commissioned in February 2003 and has acquired 6 years of data thus far. The NEMO-3 collaboration has produced some of the most competitive and sensitive $2\nu\beta\beta$ decay results to date for many of the isotopes housed inside the detector, including the $2\nu\beta\beta$ decay of $^{96}\mathrm{Zr}$, which is the focus of this analysis.

A comprehensive account of the NEMO-3 detector is given describing the main parts: calorimeter, tracking detector, source isotopes, radon purification facility, and passive shielding. A description and measurement of the external and internal backgrounds associated with the experiment are presented. An outline of the topological signatures of electrons, positrons, photons, and alphas distinguishes NEMO-3 from other current experiments and provides a powerful tool for background suppression and identification of different kinematic $2\nu\beta\beta$ and $0\nu\beta\beta$ decay mechanisms.

Using 9.4 g of $^{96}\mathrm{Zr}$ and 1221 days of data corresponding to 0.031 kg·y, the $2\nu\beta\beta$ decay half-life measurement to the ground state is

$$T_{1/2}^{2\nu} = [2.35 \pm 0.14(stat) \pm 0.16(syst)] \times 10^{19}\,\mathrm{yr}\,,$$

corresponding to the matrix element

$$M^{2\nu} = 0.049 \pm 0.002\,.$$

This is the world's most precise measurement by a factor of 4 and provides a vital constraint on future NME calculations which can then be used to extract new physics from $0\nu\beta\beta$ decay. The $0\nu\beta\beta$ decay was excluded at the 90% CL

$$T^{0\nu}_{1/2} > 9.2 \times 10^{21}\,\mathrm{yr}\,,$$

which corresponds to an effective Majorana neutrino mass

$$\langle m_{\beta\beta} \rangle < 7.2 - 19.4\,\mathrm{eV}\,,$$

and this result is the world's most strict limit for ^{96}Zr to date.

Due for commissioning in 2012, SuperNEMO is the next generation detector which improves upon the proven technology and success of NEMO-3 to achieve a half-life sensitivity of $\sim 10^{26}$ yr (90% CL) for ^{82}Se which corresponds to a neutrino mass of 50-100 meV giving access to the inverted hierarchy. An overview of the R&D activities is presented including the calorimeter, tracking detector, source enrichment and purification, and software development. The focus of this presented research is on achieving an energy resolution of 7% FWHM at 1 MeV for the baseline design calorimeter of SuperNEMO. The contending calorimeter components such as the scintillators and PMTs are discussed and the factors contributing to the energy resolution are outlined and investigated through experimentation. The energy resolution measurements of numerous calorimeter configurations have been carried out and tabulated. The advantages and downsides of each contending configuration are discussed.

Finally an energy resolution of 7% FWHM at 1 MeV has been obtained for the calorimeter baseline design of SuperNEMO and verified by an independent experimental technique. This result not only meets the requirement stipulated by the R&D proposal, but is unprecedented for this type of calorimeter design. This result reflects the advantages of PVT based scintillator and high QE PMTs.

The calorimeter choices pursued in this study (ELJEN-200 PVT plastic scintillators and 8" Hamamatsu R5912-MOD PMTs) have been selected by the SuperNEMO collaboration as a building block of the calorimeter baseline design. Remaining work to finalize details of the calorimeter mechanical design has been outlined.

Bibliography

[1] W. Pauli. Dear radioactive ladies and gentlemen. *Phys. Today*, 31N9:27, 1978.

[2] B. Pontecorvo. Mesonium and antimesonium. *Sov. Phys. JETP*, 6:429, 1957.

[3] Z. Maki, M. Nakagawa, and S. Sakata. Remarks on the unified model of elementary particles. *Prog. Theor. Phys.*, 28:870–880, 1962.

[4] B. Aharmim et al. An Independent Measurement of the Total Active 8B Solar Neutrino Flux Using an Array of 3He Proportional Counters at the Sudbury Neutrino Observatory. *Phys. Rev. Lett.*, 101:111301, 2008, nucl-ex/0806.0989.

[5] G. Prior. Results from the Sudbury Neutrino Observatory phase III. *Nucl. Phys. Proc. Suppl.*, 188:96–100, 2009.

[6] Y. Ashie et al. A Measurement of Atmospheric Neutrino Oscillation Parameters by Super-Kamiokande I. *Phys. Rev.*, D71:112005, 2005, hep-ex/0501064.

[7] K. Okumura. Recent status of Super-Kamiokande. *AIP Conf. Proc.*, 981:139–141, 2008.

[8] M. Apollonio et al. Search for neutrino oscillations on a long base-line at the CHOOZ nuclear power station. *Eur. Phys. J.*, C27:331–374, 2003, hep-ex/0301017.

[9] S. Abe et al. Precision Measurement of Neutrino Oscillation Parameters with KamLAND. *Phys. Rev. Lett.*, 100:221803, 2008, hep-ex/0801.4589.

[10] I. Shimizu. KamLAND results. *Nucl. Phys. Proc. Suppl.*, 188:84–89, 2009.

[11] M.H. Ahn et al. Measurement of Neutrino Oscillation by the K2K Experiment. *Phys. Rev.*, D74:072003, 2006, hep-ex/0606032.

[12] R. Terri. Results of the K2K oscillation analysis. *AIP Conf. Proc.*, 981:169–171, 2008.

[13] P. Adamson et al. Measurement of Neutrino Oscillations with the MINOS Detectors in the NuMI Beam. *Phys. Rev. Lett.*, 101:131802, 2008, hep-ex/0806.2237.

[14] M. Maltoni, T. Schwetz, M.A. Tortola, and J.W.F. Valle. Status of global fits to neutrino oscillations. *New J. Phys.*, 6:122, 2004, hep-ph/0405172.

[15] X. Guo et al. A precision measurement of the neutrino mixing angle theta(13) using reactor antineutrinos at Daya Bay. 2007, hep-ex/0701029.

[16] F. Ardellier et al. Double Chooz: A search for the neutrino mixing angle theta(13). 2006, hep-ex/0606025.

[17] Y. Itow et al. The JHF-Kamioka neutrino project. 2001, hep-ex/0106019.

[18] D.S. Ayres et al. NOvA proposal to build a 30-kiloton off-axis detector to study neutrino oscillations in the Fermilab NuMI beamline. 2004, hep-ex/0503053.

[19] C. Giunti and Ch.W. Kim. Fundamentals of Neutrino Physics and Astrophysics. Oxford, UK: Univ. Pr. (2007) 710 p.

[20] E. Majorana. Theory of the Symmetry of Electrons and Positrons. *Nuovo Cim.*, 14:171–184, 1937.

[21] U. Seljak et al. Cosmological parameter analysis including SDSS Ly-alpha forest and galaxy bias: Constraints on the primordial spectrum of fluctuations, neutrino mass, and dark energy. *Phys. Rev.*, D71:103515, 2005, astro-ph/0407372.

[22] A.M. Malinovsky, A.A. Voevodkin, V.N. Lukash, E. V. Mikheeva, and A. A. Vikhlinin. Cosmological constraints on the neutrino mass from CMB anisotropy and large-scale structure of the universe. *Astron. Lett.*, 34:445–450, 2008.

[23] Ch. Kraus et al. Final Results from phase II of the Mainz Neutrino Mass Search in Tritium β Decay. *Eur. Phys. J.*, C40:447–468, 2005, hep-ex/0412056.

[24] E.W. Otten and C. Weinheimer. Neutrino mass limit from tritium beta decay. *Rept. Prog. Phys.*, 71:086201, 2008, hep-ex/0909.2104.

[25] Yu.G. Zdesenko, F.A. Danevich, and V.I. Tretyak. Has neutrinoless double beta decay of Ge-76 been really observed? *Phys. Lett.*, B546:206–215, 2002.

[26] C.F.V. Weizsacker. Zur Theorie der Kernmassen. *Z. Phys.*, 96:431–458, 1935.

[27] M. Goeppert-Mayer. Double beta-disintegration. *Phys. Rev.*, 48:512–516, 1935.

[28] G. Racah. On pair production through charged particle collisions. *Nuovo Cim.*, 14:93–113, 1937.

[29] W.H. Furry. On transition probabilities in double beta-disintegration. *Phys. Rev.*, 56:1184–1193, 1939.

[30] C. Amsler et al. Review of particle physics. *Phys. Lett.*, B667:1, 2008.

[31] R.N. Mohapatra and P.B. Pal. Massive neutrinos in physics and astrophysics. Second edition. *World Sci. Lect. Notes Phys.*, 60:1–397, 1998.

[32] Z.G. Berezhiani, A.Yu. Smirnov, and J.W.F. Valle. Observable Majoron emission in neutrinoless double beta decay. *Phys. Lett.*, B291:99–105, 1992, hep-ph/9207209.

[33] R.N. Mohapatra, A. Perez-Lorenzana, and C.A. Pires. Neutrino mass, bulk Majoron and neutrinoless double beta decay. *Phys. Lett.*, B491:143–147, 2000, hep-ph/0008158.

[34] P. Bamert, C.P. Burgess, and R.N. Mohapatra. Multi-Majoron modes for neutrinoless double beta decay. *Nucl. Phys.*, B449:25–48, 1995, hep-ph/9412365.

[35] R.N. Mohapatra and E. Takasugi. Neutrinoless Double Beta Decay with Double Majoron Emission. *Phys. Lett.*, B211:192, 1988.

[36] N. Fatemi-Ghomi. Measurement of the double beta decay half-life of Nd-150 and search for neutrinoless decay modes with NEMO-3 detector. *PhD Thesis*, 2009, hep-ex/0905.0822. University of Manchester, UK.

[37] M. Hirsch, H.V. Klapdor-Kleingrothaus, and S.G. Kovalenko. Supersymmetry and neutrinoless double beta decay. *Phys. Rev.*, D53:1329–1348, 1996, hep-ph/9502385.

[38] S.T. Petcov, H. Sugiyama, and Y. Takanishi. Neutrinoless Double Beta Decay and H++/– to l'+/- l+/- Decays in the Higgs Triplet Model. *Phys. Rev.*, D80:015005, 2009, hep-ph/0904.0759.

[39] J. Menendez, A. Poves, E. Caurier, and F. Nowacki. Disassembling the Nuclear Matrix Elements of the Neutrinoless double beta Decay. *Nucl. Phys.*, A818:139–151, 2009, nucl-th/0801.3760.

[40] J. Menendez, A. Poves, E. Caurier, and F. Nowacki. Deformation and the Nuclear Matrix Elements of the Neutrinoless Double Beta Decay. 2008, nucl-th/0809.2183.

[41] M. Kortelainen and J. Suhonen. Nuclear matrix elements of neutrinoless double beta decay with improved short-range correlations. *Phys. Rev.*, C76:024315, 2007, nucl-th/0708.0115.

[42] V.A. Rodin, A. Faessler, F. Simkovic, and P. Vogel. Assessment of uncertainties in QRPA 0nu beta beta decay nuclear matrix elements. *Nucl. Phys.*, A766:107–131, 2006, nucl-th/0706.4304.

[43] J. Suhonen and O. Civitarese. Weak-interaction and nuclear-structure aspects of nuclear double beta decay. *Phys. Rept.*, 300:123–214, 1998.

[44] A. Faessler and F. Simkovic. Double beta decay. *J. Phys.*, G24:2139–2178, 1998, hep-ph/9901215.

[45] F.T. Avignone, S.R. Elliott, and J. Engel. Double Beta Decay, Majorana Neutrinos, and Neutrino Mass. *Rev. Mod. Phys.*, 80:481–516, 2008, nucl-ex/0708.1033.

[46] K. Chaturvedi, R. Chandra, P.K. Rath, P.K. Raina, and J.G. Hirsch. Nuclear deformation and neutrinoless double-beta decay of Zr-94, Zr-96, Mo-98, Mo-100, Ru-104, Pd-110, Te-128, Te-130, and Nd-150 nuclei within a mechanism involving neutrino mass. *Phys. Rev.*, C78:054302, 2008.

[47] R. Chandra, K. Chaturvedi, P.K. Rath, P.K. Raina, and J.G. Hirsch. Multipolar correlations and deformation effect on nuclear transition matrix elements of double-beta decay. 2009, nucl-th/0902.0658.

[48] V.I. Tretyak. New Results from the NEMO 3 Experiment. 2008, nucl-ex/0807.2157.

[49] A.S. Barabash. NEMO 3 double beta decay experiment: latest results. *J. Phys. Conf. Ser.*, 173:012008, 2009, nucl-ex/0807.2336.

[50] A.S. Barabash. Double beta decay experiments. *JINST*, 1:P07002, 2006, hep-ex/0602037.

[51] J. Argyriades et al. Measurement of the two neutrino double beta decay half-life of Zr-96 and search for associated neutrinoless processes with the NEMO-3 detector. 2009, nucl-ex/0906.2694.

[52] R. Arnold et al. First results of the search of neutrinoless double beta decay with the NEMO 3 detector. *Phys. Rev. Lett.*, 95:182302, 2005, hep-ex/0507083.

[53] J. Argyriades et al. Measurement of the Double Beta Decay Half-life of 150-Nd and Search for Neutrinoless Decay Modes with the NEMO-3 Detector. *Phys. Rev.*, C80:032501, 2009, hep-ex/0810.0248.

[54] S. Umehara et al. Neutrino-less Double Beta Decay of ^{48}Ca studied by CaF2(Eu) Scintillators. *Phys. Rev.*, C78:058501, 2008, nucl-ex/0810.4746.

[55] I. Ogawa et al. Search for neutrino-less double beta decay of Ca-48 by CaF-2 scintillator. *Nucl. Phys.*, A730:215–223, 2004.

[56] H.V. Klapdor-Kleingrothaus, I.V. Krivosheina, A. Dietz, and O. Chkvorets. Search for neutrinoless double beta decay with enriched 76Ge in Gran Sasso 1990-2003. *Phys. Lett.*, B586:198–212, 2004, hep-ph/0404088.

[57] H.V. Klapdor-Kleingrothaus et al. Latest Results from the Heidelberg-Moscow Double Beta Decay Experiment. *Eur. Phys. J.*, A12:147–154, 2001, hep-ph/0103062.

[58] C. E. Aalseth et al. The IGEX experiment revisited: a response to the critique of Klapdor-Kleingrothaus,Dietz, and Krivosheina. *Phys. Rev.*, D70:078302, 2004, nucl-ex/0404036.

[59] D. Gonzalez et al. Pulse shape discrimination in the IGEX experiment. *Nucl. Instrum. Meth.*, A515:634–643, 2003, hep-ex/0302018.

[60] N. Kudomi et al. Double beta decays of Mo-100 by ELEGANT V at Oto Cosmo Observatory. *Nucl. Phys. Proc. Suppl.*, 87:301–303, 2000.

[61] N. Kudomi et al. Double beta decays and ELEGANT V and VI at Oto Cosmo Observatory. *Nucl. Phys.*, A629:527c–530c, 1998.

[62] F. Bellini. Neutrinoless double beta decay search with CUORICINO and CUORE experiments. *Nucl. Phys. Proc. Suppl.*, 188:65–67, 2009.

[63] C. Arnaboldi et al. Results from a search for the 0vbb-decay of 130Te. *Phys. Rev.*, C78:035502, 2008, hep-ex/0802.3439.

[64] S. Umehara et al. CANDLES for double beta decay of Ca-48. *J. Phys. Conf. Ser.*, 39:356–358, 2006.

[65] Y. Hirano et al. Study of double beta decay of Ca-48 with CANDLES. *J. Phys. Conf. Ser.*, 120:052053, 2008.

[66] A.A. Smolnikov. Status of the GERDA experiment aimed to search for neutrinoless double beta decay of 76Ge. 2008, nucl-ex/0812.4194.

[67] J. Janicsko-Csathy. Status of the GERDA experiment. *Nucl. Phys. Proc. Suppl.*, 188:68–70, 2009.

[68] F.T. Avignone, III. The MAJORANA 76Ge neutrino less double-beta decay project: A brief update. *J. Phys. Conf. Ser.*, 120:052059, 2008, nucl-ex/0711.4808.

[69] C.E. Aalseth et al. The proposed Majorana Ge-76 double-beta decay experiment. *Nucl. Phys. Proc. Suppl.*, 138:217–220, 2005.

[70] R. Saakyan. Topological detection of double beta decay with NEMO3 and SuperNEMO. *J. Phys. Conf. Ser.*, 179:012006, 2009.

[71] R.B. Pahlka. The SuperNEMO Experiment. 2008, hep-ex/0810.3169.

[72] H. Ejiri. The MOON project and DBD matrix elements. *J. Phys. Conf. Ser.*, 173:012009, 2009.

[73] H. Ejiri et al. MOON for neutrino-less double beta decays. *Eur. Phys. J. ST*, 162:239–250, 2008.

[74] J.R. Wilson. The COBRA experiment. *J. Phys. Conf. Ser.*, 120:052048, 2008.

[75] K. Zuber. COBRA: Double beta decay searches using CdTe detectors. *Phys. Lett.*, B519:1–7, 2001, nucl-ex/0105018.

[76] F. Bellini. Neutrinoless double beta decay search with CUORICINO and CUORE experiments. *Nucl. Phys. Proc. Suppl.*, 188:65–67, 2009.

[77] R. Maruyama. Cryogenic Double Beta Decay Experiments: CUORE and CUORICINO. 2008, nucl-ex/0809.3840.

[78] R. Gornea. Double beta decay in liquid xenon. *J. Phys. Conf. Ser.*, 179:012004, 2009.

[79] N. Ackerman. Status of EXO-200. 2009, hep-ex/0909.1826.

[80] J.J. Gomez Cadenas, J. Martin-Albo, J. Munoz Vidal, and M. Sorel. The NEXT generation of neutrinoless double beta decay experiments. *J. Phys. Conf. Ser.*, 171:012068, 2009.

[81] J. Diaz et al. The NEXT experiment. *J. Phys. Conf. Ser.*, 179:012005, 2009.

[82] I. Barabanov et al. Characterization of a Nd-loaded organic liquid scintillator for neutrinoless double beta decay search of 150-Nd with a 10-ton scale detector. 2009, physics.ins-det/0909.2152.

[83] N. Ishihara et al. DCBA experiment for searching for neutrinoless double beta decay (II). *J. Phys. Conf. Ser.*, 120:052062, 2008.

[84] M.C. Chen. The SNO+ Experiment. 2008, hep-ex/0810.3694.

[85] K. Zuber. Nd double beta decay search with SNO+. *AIP Conf. Proc.*, 942:101–104, 2007.

[86] A. Staudt, K. Muto, and H.V. Klapdor-Kleingrothaus. Calculation of 2nu and 0nu double-beta decay rates. *Europhys. Lett.*, 13:31–36, 1990.

[87] S. Pirro et al. The final results of the Mi-Beta cryogenic experiment towards the CUORICINO experiment. *AIP Conf. Proc.*, 605:449–452, 2002.

[88] S. Pirro et al. Present status of MI-BETA cryogenic experiment and preliminary results for CUORICINO. *Nucl. Instrum. Meth.*, A444:71–76, 2000.

[89] Y. Takeuchi et al. Measurement of radon concentrations at Super-Kamiokande. *Phys. Lett.*, B452:418–424, 1999, hep-ex/9903006.

[90] R.B. Firestone and V.S. Shirley. Table of Isotopes, 8th Edition. 1999. John Wiley and Sons, 2 volumes, 3168 pages.

[91] O.A. Ponkratenko, V.I. Tretyak, and Yu.G. Zdesenko. The Event generator DECAY4 for simulation of double beta processes and decay of radioactive nuclei. *Phys. Atom. Nucl.*, 63:1282–1287, 2000, nucl-ex/0104018.

[92] R. Brun, F. Bruyant, M. Maire, A.C. McPherson, and P. Zanarini. GEANT-3. 1987. CERN-DD/EE/84-1.

[93] J. Argyriades et al. Measurement of the background in the NEMO 3 double beta decay experiment. *Nucl. Instrum. Meth.*, A606:449–465, 2009, nucl-ex/0903.2277.

[94] R. Arnold et al. Technical design and performance of the NEMO 3 detector. *Nucl. Instrum. Meth.*, A536:79–122, 2005, physics/0402115.

[95] X. Sarazin. Search for neutrinoless double beta decay with the NEMO-3 detector: First results. *Nucl. Phys. Proc. Suppl.*, 143:221–224, 2005, hep-ex/0412012.

[96] G.J. Feldman and R.D. Cousins. A Unified Approach to the Classical Statistical Analysis of Small Signals. *Phys. Rev.*, D57:3873–3889, 1998, physics/9711021.

[97] O. Helene. Upper Limit of Peak Area. *Nucl. Instr. Meth.*, 212:319, 1983.

[98] Th. Junk. Confidence level computation for combining searches with small statistics. *Nucl. Instrum. Meth.*, A434:435–443, 1999, hep-ex/9902006.

[99] A.L. Read. Presentation of search results: The CL(s) technique. *J. Phys.*, G28:2693–2704, 2002.

[100] P. Pagelkopf and J. Porstendorfer. Neutralisation rate and the fraction of the positive 218Po-clusters in air. *Atmospheric Environment*, 37:1057–1064(8), March 2003.

[101] C. Augier. *internal note*, 2003.

[102] S. King. Measurement of the double beta decay half-life of Mo-100 to the 0+1 excited state, and Ca-48 to the ground state in the NEMO 3 experiment. *PhD Thesis*, 2008. University College London, UK.

[103] R. Arnold et al. Double beta decay of Zr-96. *Nucl. Phys.*, A658:299–312, 1999.

[104] O. Helene. Determination of the upper limit of a peak area. *Nucl. Instrum. Meth.*, A300:132–136, 1991.

[105] A.S. Barabash et al. Investigation of the Beta Beta decay of Zr-96 to excited states in Mo-96. *J. Phys.*, G22:487–496, 1996.

[106] R. Arnold et al. Limits on different Majoron decay modes of Mo-100, Cd-116, Se-82 and Zr-96 for neutrinoless double beta decays in the NEMO-2 experiment. *Nucl. Phys.*, A678:341–352, 2000.

[107] R. Chandra, J. Singh, P.K. Rath, P.K. Raina, and J.G. Hirsch. Two neutrino double beta decay of A=94 through A=110 nuclei for 0+ to 0+ transition. *Eur. Phys. J.*, A23:223–234, 2005, nucl-th/0405074.

[108] O. Civitarese and J. Suhonen. Nuclear matrix elements for double beta decay in the QRPA approach: A critical review. *J. Phys. Conf. Ser.*, 173:012012, 2009.

[109] G. Pantis, F. Simkovic, J.D. Vergados, and A. Faessler. Neutrinoless Double Beta Decay within QRPA with Proton-Neutron Pairing. *Phys. Rev.*, C53:695–707, 1996, nucl-th/9612036.

[110] F. Simkovic et al. Anatomy of nuclear matrix elements for neutrinoless double-beta decay. *Phys. Rev.*, C77:045503, 2008, nucl-th/0710.2055.

[111] A.S. Barabash. Double beta decay: present status. 2008, hep-ex/0807.2948.

[112] A.S. Barabash. Is the weak interaction constant really constant? *Czech. J. Phys.*, 50:455–461, 2000.

[113] A.S. Barabash. Possible evidence of time variation of weak interaction constant from double beta decay experiments. *Astrophys. Space Sci.*, 283:607–612, 2003, nucl-ex/0210011.

[114] A. Kawashima, A. Masuda, and K. Takahashi. Geochemical estimation of the halflife for the double beta decay of Zr-96. *Phys. Rev.*, C47:2452–2456, 1993.

[115] M.E. Wieser and J.R. De Laeter. Evidence of the double beta decay of zirconium-96 measured in 1.8 x 10*9 year-old zircons. *Phys. Rev.*, C64:024308, 2001.

[116] R.V. Vasiliev. The BiPo low-background detector project. *Phys. Part. Nucl. Lett.*, 6:241–245, 2009.

[117] R.B. Palkha. *internal note*, 2008.

[118] F.T. Avignone, G.S. King, and Yu.G. Zdesenko. Next generation double-beta decay experiments: Metrics for their evaluation. *New J. Phys.*, 7:6, 2005.

[119] B. Anderson. *internal note*, 2009.

[120] E. Chauveau. *internal note*, 2008.

[121] A. Basharina-Freshville. *internal note*, 2008.

[122] Hamamatsu Corporation (www.hamamatsu.com). UBA and SBA Photomultiplier Tube Series. *TPMH1305E03*, 2008.

[123] T. Asch et al. Single photoelectron resolution for the calibration of photomultiplier systems. *Nuclear Science Symposium Conference Record, 2005 IEEE*, 2:887–890, 2005.

[124] I. Chirikov-Zorin et al. Method for precise analysis of the metal package photomultiplier single photoelectron spectra. *Nucl. Instrum. Meth.*, A456:310–324, 2001.

[125] R.B. Palkha. *internal note*, 2008.

[126] I.M. Chakravarti, R.G. Laha, and J. Roy. Handbook of Methods of Applied Statistics. Volume 1:392–394, 1967. John Wiley and Sons.

[127] M. Rose. *internal note*, 2007.